D 2019

U.PORTO
FEUP FACULDADE DE ENGENHARIA
UNIVERSIDADE DO PORTO

POLYDIMETHYLSILOXANE (PDMS) MICROPARTICLES SYNTHESIS FOR A NOVEL BLOOD ANALOGUE SUSPENSION

JOÃO MANUEL LEITE PIMENTA CARNEIRO

TESE DE DOUTORAMENTO APRESENTADA
À FACULDADE DE ENGENHARIA DA UNIVERSIDADE DO PORTO EM
ENGENHARIA QUÍMICA E BIOLÓGICA

U.PORTO
FEUP FACULDADE DE ENGENHARIA
UNIVERSIDADE DO PORTO

Polydimethylsiloxane (PDMS) microparticles synthesis for a novel blood analogue suspension

A thesis submitted in partial fulfilment of the requirements for the degree of Doctor in Chemical and Biological Engineering of the Faculty of Engineering of the University of Porto,
by

João Manuel Leite Pimenta Carneiro

João Bernardo Lares Moreira de Campos – Supervisor

João Mário Rodrigues Miranda – Co-supervisor

ceft
TRANSPORT PHENOMENA RESEARCH CENTER
Department of Chemical Engineering,
Faculty of Engineering, University of Porto, Portugal

October 2019

POPH QUALIFICAR E CRESCER
QREN QUADRO DE REFERÊNCIA ESTRATÉGICO NACIONAL
GOVERNO DA REPÚBLICA PORTUGUESA
UNIÃO EUROPEIA Fundo Social Europeu

This thesis was funded by FEDER funds through the Operational Programme for Competitiveness Factors COMPETE and National Funds through FCT (Fundação para a Ciência e a Tecnologia) under projects UID/EMS/00532/2019, POCI-01-0145-FEDER-016861-PTDC/QEQ-FTT/4287/2014 and grant PD/BD/114313/2016.

Transport Phenomena Research Center
University of Porto – Faculty of Engineering
Rua Dr.Roberto Frias s/n, 4200-465 Porto
up200302475@fe.up.pt

Agradecimentos

Queria agradecer em primeiro lugar ao meu Orientador Professor João Moreira de Campos pela oportunidade que me deu para a realização deste trabalho e por ter acreditado nas minhas capacidades, mesmo quando eu não acreditei. Para além de um excelente orientador, pessoa e acima de tudo amigo, foi um pilar importante no meu crescimento como investigador e como pessoa e esteve sempre disponível quando necessitei de ajuda tanto a nível de trabalho como a nível pessoal. Ao meu Co-orientador Professor João Mário Miranda um grande obrigado. A sua grande capacidade de *insight* fez-me pensar em ideias fora da caixa e tornou o trabalho muito mais interessante. Para além da parte laboral, sou grande fã do seu sentido de humor e gosto de ouvir a sua opinião acerca de diversos assuntos.

Um agradecimento muito especial à minha colega, amiga e recentemente mãe do grande Vasquinho, Erica Doutel. É uma lutadora de um enorme coração e sem ela não teria começado este doutoramento. Foi, é e será uma pessoa fundamental na minha vida, um grande beijinho. Também queria agradecer ao José Nogueira pela grande amizade, companheirismo e pragmatismo, um forte abraço.

Aos meus colegas e amigos de trabalho do CEFT, Ana, André, Marta, Soraia, Francisco, Samir, Joana e Tomás. Um Abraço especial ao Filipe Direito que neste momento se encontra para os lados do Brexit. Aos meus colegas e amigos do CEFT que proporcinaram grandes momentos de galhofa e também de *brainstorming*, essenciais para manter a minha sanidade mental ao longo deste trabalho. Aos meus antigos colegas do CEFT, em especial à Doutora Patrícia. Foi uma grande mentora e amiga e, em grande parte, responsável pela minha formação como investigador. Ao colega e amigo Ali Emami pela grande amizade e disponibilidade, grande Abraço.

Aos antigos supervisores Professora Mónica, Professora Laura Campo e Professor Fernando Pinho um muito obrigado. Um Beijinho especial à Professora Mónica. Foram muito importantes na minha formação como investigador. Ao Professor João Barreto, Professor João Barbosa e Professor Fernando Jorge um grande obrigado por me ouvirem e me aconselharem nos momentos mais críticos do meu percurso.

Aos meus amigos da comunidade de Magic. Apesar da recente amizade, aturaram-me nestes últimos dois anos. Também me ajudaram a crescer como pessoa e a abrir horizontes.

Aos meus amigos de infância que, apesar de grande parte estar emigrada, sempre mantivemos o contacto. Um agradecimento especial ao Miguel Martins. Ajudou-me na altura mais difícil da minha vida e sem ele não teria feito este percurso. Ao César, Nice e Gaspar pela sua amizade incondicional.

Em último lugar, mas não menos importante, queria agradecer à minha Família, em especial, à minha companheira Diana, aos meus Pais, à minha Irmã e às minhas lindas sobrinhas Aurora e Isaura. Foram a grande força motriz de todo o meu percurso estando sempre presentes. Amo-vos muito.

To my Family

Table of contents

Abstract

Cardiovascular diseases are one of the leading causes of death in developed countries. Local hemodynamic plays an important role in the better understanding of such diseases. Blood has a non–Newtonian viscoelastic shear–thinning behavior, which results, in large part, from the particulate matter, more specifically, from the presence of red blood cells (RBC). Due to ethical concerns and practical limitations, *in vitro* blood flows experiments are usually performed with blood analogue fluids. An ideal blood analogue must match the blood rheology in multiple scales, micro and macro, mimicking its non-continuum nature.

Polydimethylsiloxane (PDMS) polymeric particles are an interesting candidate to mimic the RBCs, as PDMS is a transparent inert elastomer. Along this thesis, two multiphase methods to produce PDMS microparticles are explored: one supported on a microfluidic flow focusing device and another through a membrane emulsification process.

The first method consists in the PDMS droplets production in a PDMS square section microchannel. The droplets generation was characterized and a flow regime map was sketched, delimiting the different flow regimes found: dripping, jetting, threading and viscous displacement. Afterwards, a numerical study validated by experimental data enabled the investigation of other flow conditions such as different viscosity ratios in free surfactant systems. The numerical code, based on a coupled level-set method and on a volume of fluid method, successfully predicts droplets size in surfactant free systems in almost all the conditions studied, but fails to predict in certain flow conditions when surfactant is used. With all the information gathered from the first two studies, the next step was the production of microparticles of PDMS. The droplets were generated in a flow focusing microfluidic PDMS channel in the jetting regime, and afterwards cross-linked in a thermal process to form microparticles with no shrinkage observed. The microparticles size distributions, constitution, morphology and optical properties were characterized. Although with microparticle quantities still insufficient to produce the necessary volumes to conduct a rheological characterization, the optical properties of the microparticles are shown to be ideal to perform visualization and velocimetry experiments.

The second method to produce PDMS microparticles was based in a multi-stage membrane emulsification process. This method allows the production of a large quantity, ~ 6 g, of RBCs size PDMS microparticles in under 3 hours. The microparticles concentration was adjusted to cover a wide hematocrit range. A blood analogue suspension consisting in a 21 % (w/w) PDMS water suspension has, at working lab temperatures (~20 ºC), excellent steady-state

shear rheology results, replicating the shear-thinning behavior of whole blood samples at physiological temperatures (~37 ºC). Moreover, the same suspension has relaxation times, measured in an extensional rheometer, of the same order of magnitude of the whole blood. Also, it presents good qualitative results, for different concentrations, in cell-free-layer tests. The novel blood analogue suspension developed in this thesis demonstrated promising results and will be tested in future macro and micro-scale *in vitro* hemodynamic studies.

Keywords: cardiovascular diseases; blood analogue; RBC; PDMS microparticles; flow-focusing droplet microfluidics; viscous fluids; regime map; numerical study; optical properties; membrane emulsification; *in vitro* hemodynamics.

.

Sumário

As doenças cardiovasculares são uma das principais causas de morte nos países desenvolvidos. A hemodinâmica desempenha um papel importante na compreensão destas doenças. O sangue possui um comportamento não-Newtoniano, reofluidificante e viscoelástico, o qual resulta, em grande parte, da sua matéria particulada, mais especificamente, da presença de glóbulos vermelhos (GV). Devido a preocupações éticas e limitações práticas, experiências *in vitro* de escoamentos sanguíneos são geralmente realizadas com fluidos analógos ao sangue. Um análogo ideal deve ter uma reologia semelhante à do sangue em várias escalas, micro e macro, mimetizando a sua natureza não contínua.

Micropartículas poliméricas de polidimetilsiloxano (PDMS) são potenciais candidatas para mimetizar os GVs, pois o PDMS é um elastómero inerte e transparente. Na execução deste trabalho foram explorados dois métodos, baseados em escoamentos multifásicos, para produzir micropartículas de PDMS: um através de um dispositivo microfluídico de escoamento convergente e outro através de um processo de emulsificação numa membrana.

O primeiro método consiste na produção de gotas de PDMS num microcanal de secção quadrada de PDMS. A geração de gotas foi caracterizada ao mesmo tempo que foi desenhado um mapa de regimes de escoamento: "*dripping"*, "*jetting"*, "*threading"* e "*viscous displacement"*. Posteriormente, um estudo numérico complementou os dados experimentais e possibilitou a investigação de outras condições, como diferentes razões de viscosidade na ausência de surfactante. O código numérico, baseado na combinação de dois métodos numéricos, "*level-set"* e "*volume of fluid"*, prevê com sucesso o tamanho das gotas na ausência de surfactante, mas falha, em certas condições de escoamento, quando se inclui o surfactante. Após a informação dos dois primeiros estudos, o passo seguinte foi a produção de micropartículas de PDMS. As gotas foram geradas no microcanal de PDMS em escomento convergente no regime de "*jetting"* e, posteriormente, curadas termicamente para formar micropartículas sem se observar qualquer retração de tamanho. As distribuições de tamanho das micropartículas, constituição, morfologia e propriedades ópticas foram caracterizadas. Embora com quantidades de micropartículas ainda insuficientes para a

realização de testes reológicos, este método permitiu ter partículas com propriedades ópticas ideais para realizar experiências de visualização e de velocimetria.

O segundo método para produzir micropartículas de PDMS foi baseado num processo de emulsificação através de uma membrana. Com este método é possível produzir uma grande quantidade, ~ 6 g, de micropartículas de PDMS em menos de 3 horas e com tamanho semelhante ao dos GVs. A concentração de micropartículas foi ajustada para abranger uma ampla gama de concentração de hematócritos. Uma suspensão análoga, consistindo numa suspensão aquosa com 21 % (w/w) de partículas de PDMS demonstrou, a temperaturas laboratoriais (~ 20 ºC), ter uma reologia de corte em estado estacionário semelhante à do sangue a temperaturas fisiológicas (~ 37 ºC). A mesma suspensão, quando sujeita a um escoamanto extensional, demonstrou tempos de relaxação, medidos num reómetro extensional, da mesma ordem de grandeza dos do sangue. Para além disso, apresenta bons resultados qualitativos, para diferentes concentrações, nos testes de camada livre de células. A suspensão análoga ao sangue desenvolvida nesta tese demonstrou resultados promissores e será testada em futuros estudos hemodinâmicos *in vitro* à macro e micro escalas.

Palavras-chave: doenças cardiovasculares; análogo do sangue; GV; microparticulas de PDMS; dispositivo microfluidico de escoamento convergente; fluidos viscosos; mapa de regimes; estudo numérico; propriedades óticas; emulsificação por membrana; hemodinâmica *in vitro*.

1

Chapter

Introduction

1

Introduction

1.1 Motivation

The cardiovascular system is exposed to a number of specific illnesses such as: coronary heart diseases, heart failure, arrhythmias, strokes, arterial and pulmonary hypertension, congenital heart diseases, cardiomyopathies and vascular heart diseases. Despite noticeable medical advances over the last few decades, cardiovascular diseases (CVD) remain a leading cause of death, being the number one in the European Union (EU) [1]. Local hemodynamic plays an important role in the better understanding of these lesions [2]. As long as blood circulates freely perfusing the tissues adequately, the body has a good chance to deal with many of the imposed disorders. However, once the blood flow stops or decreases, the tissue can be irreversibly injured. Blood flow is affected by its viscosity and more specifically by its sub-phases and particulate matter [3, 4]. Blood is a dense suspension composed of several elements, being the most important the red blood cells (RBCs), white blood cells and platelets dispersed in an aqueous matrix called plasma [4]. In large vessels, the blood can be treated as a homogeneous suspension, while in microvessels, diameters varying from ~ 6 to 300 μm [5, 6], such as arterioles, venules and especially in capillaries (diameter smaller than 8 μm), blood flow is strongly affected by geometric features, like contractions, expansions and bifurcations. These harmful effects can be enhanced by RBCs aggregation, which increases microvascular flow resistance and consequently reduce blood perfusion to the organs, leading to ischemia [6, 7]. Also, diseases that change the mechanical properties of the RBCs, i.e. diabetes and malaria, lead to abnormal microvascular hemodynamics [8, 9]. Several studies have been carried out concerning

the rheological behavior of whole blood [4, 10-15]. However, the manipulation of whole blood samples and the analysis of its flow dynamics *in vivo* are difficult due to the cost, safety and ethical issues involved, so *in vitro* studies are mandatory. Also, whole blood samples easily degrade in long term experiments [16]. Therefore, *in vitro* studies with blood analogue fluids are the most adequate alternative [16, 17]. In the literature, most of the proposed analogues are Newtonian fluids, water/glycerol and water/Dimethyl sulfoxide (DMSO) mixtures, or non-Newtonian polymeric aqueous solutions based on Xantham gum, polyacrylamide and hyaluronic acid [18, 19]. The main disadvantages of these analogue fluids are that they don't take into account the cluster formation and disaggregation of RBCs in local flow conditions and also RBCs ability to deform when submitted to tangential stresses. In addition, the non-continuum nature of blood leads to complex flows, especially at the microcirculatory scale, which are not replicated with these analogues [20]. For example, a particulate blood analogue could be of interest for preliminary *in vitro* hemodynamic studies in organ-on-a-chip systems[21], cell sorting [22], microbots [23] and also to better understand abnormal microvascular phenomena such as embolisms [24]. Also, an optically optimized particulate blood analogue, can be useful in *in vitro* experiments involving visualization and velocimetry techniques in irregular shape channels mimicking patient specific arteries [25].

Along the last three decades, microfluidics has emerged as a powerful platform for the generation of droplets and microparticles [26-42], which can be useful to obtain a suitable blood analogue suspension. In this study, the major motivation is to replicate the RBCs behaviour, in all the dimensions, through Polydimethylsiloxane (PDMS) microparticles produced in microfluidic devices.

1.2 Objectives

The main objective of the present work is the production and characterization of droplets and microparticles of Polydimethylsiloxane (PDMS) to be used in blood analogue suspensions. PDMS is a biocompatible, hydrophobic, transparent inert

elastomer commonly used in microfluidic devices and a very viscous fluid, in its liquid pre-polymer state, at least 600 times higher than water [42-45]. PDMS microparticles have been used in a wide range of applications from sensors to biomimetic fluids [42, 46-50]. In order to achieve the main objective, several intermediary goals are necessary:

- Characterization of the droplets formation of a high viscous fluid, PDMS, in a flow focusing microfluidic device;
- Prediction through a numerical code, previously validated with experimental data, of the best experimental conditions for future studies of highly viscous droplet formation in a flow focusing microfluidic device;
- Search of the ideal flow conditions to produce high quantities of RBCs size PDMS microparticles via a flow focusing microfluidic device;
- Production scale-up to obtain large quantities of particles from a highly viscous polymeric precursor;
- Production of readily PDMS blood analogue suspensions. The blood analogue rheological properties need to be characterized by steady-state shear and extensional experiments and preliminary hemodynamic studies should be performed.

The final blood analogue suspension should be able to mimic the rheological properties of blood in both macro and micro-scale hemodynamic studies.

1.3 Blood properties

Whole blood is a two-phase liquid suspension consisting in a liquid medium (plasma) and formed elements such as RBCs, white blood cells, and platelets. Thus, its rheology is mainly determined by the viscous properties of the plasma, by the fraction of RBCs (hematocrit, 40 – 50%), by the viscoelastic properties of the components and also by the interaction between the different components [4].

1.3.1 RBC cell morphology

The properties of an individual RBC change as it ages and the normal life-span of a RBC in the human blood is 100 – 120 days. The shape of a normal unshared erythrocyte is a biconcave discoid with a diameter of 6 – 8 μm, surface area of approximately 130 μm^2 and approximately 98 μm^3 of volume, Figure 1.1. This shape can change as a result of mechanical, chemical or thermal effects [4]. Significantly, a biconcave disk has a high surface area to volume ratio compared to a sphere. For example, the surface area of a sphere of volume 98 μm^3 is 103 μm^2 while the area of a biconcave RBC with an equivalent volume is 130 μm^2 [4]. This enables RBCs to deform more than a spherical shaped cell [4]. Deformation of RBCs can easily be seen in capillaries (4–8 μm inner diameter) [7, 51]. RBCs align in a single line and deform into axisymmetric parachute-like shapes or into asymmetric crepe-like shapes when travelling in the capillaries [7, 51], Figure 1.2.

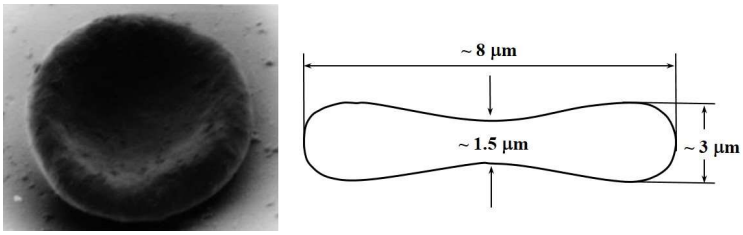

Figure 1.1. Scanning electron microscope image of a RBC (left) and schematic RBC representation with average geometric parameters (right). Adapted from Robertson et al.[4].

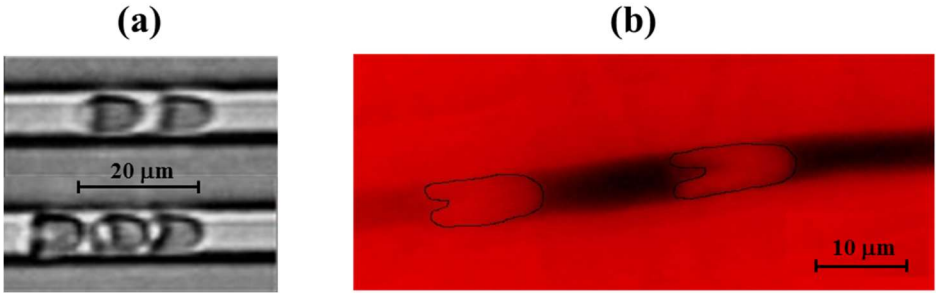

Figure 1.2. Deformation of RBCs in capillaries: a) microchannel showing the deformation of a RBC; b) mouse capillary (delimitation of RBCs for better view) with deformed RBCs. Adapted from Brust et al.[7].

1.3.2 Blood rheology

Blood is a non-Newtonian suspension exhibiting shear-thinning, thixotropic and viscoelastic characteristics. The RBCs capacity to aggregate/disaggregate and deform, depending on the local flow and on the hematocrit level, are the major contributing factors to the shear-thinning behavior [4, 7, 52-56]. Blood viscosity decreases at high shear stresses due to the deformation of RBCs, while it increases at low shear stresses because RBCs aggregate and form stacked coin structures, called *rouleaux* [12, 17]. This process is reversible and, as the shear stress increases, the larger *rouleaux* break up into smaller ones. At higher shear stress values, the suspension can be seen as a monodispersed RBCs suspension [4, 7, 52-56]. In a previous work [56], performed in the Transport Phenomena Research Center (CEFT), *in vivo* blood viscosity was measured. Blood viscosity, at 37 °C, for high shear rates (100-300 s^{-1}) is ~ 3.5 mPa s^{-1}, while it increases rapidly up to 30 mPa s^{-1} as the shear rate decreases to less than 2 s^{-1} [56], Figure 1.3.

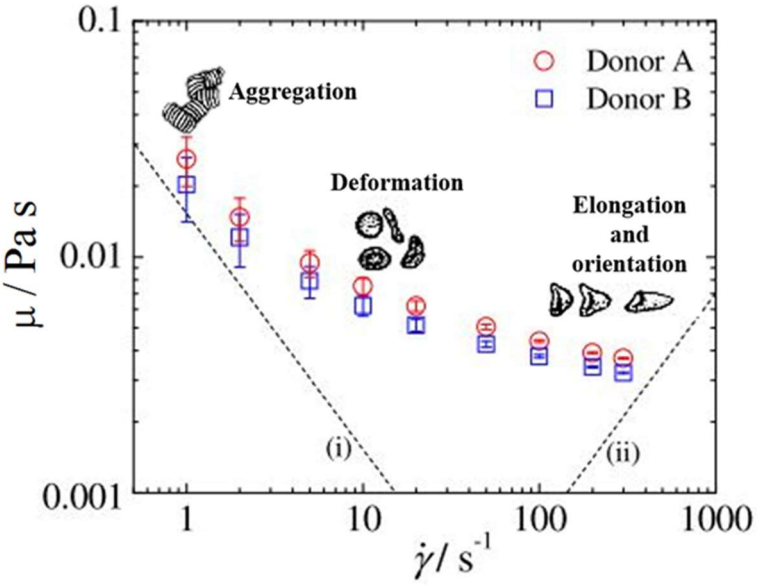

Figure 1.3. Steady-shear viscosity as a function of the shear rate measured at 37 °C, for two healthy donors, A and B, with a hematocrit of 41.6 % and 41.3 %, respectively. The dashed lines represent the minimum measurable shear viscosity based on 5× the minimum resolvable torque (i) and the onset of secondary flow due to Taylor instabilities (ii). Adapted from Sousa et al.[56].

Another key component of blood is plasma, whose infinite shear viscosity plateau, in healthy conditions, varies from 1.10 mPa s to ~ 1.35 mPa s at 37°C, while the viscosity of pure water is 1.0 mPa s at 20°C [4, 53, 54]. Recent study [55] reveals that plasma has a slight viscoelastic behavior, despite in most studies it is considered a Newtonian fluid [55]. Plasma proteins such as fibrinogen are thought to cause aggregation by facilitating binding between RBCs. High levels of fibrinogen in plasma increases RBCs aggregation and thus increases blood viscosity [4, 54, 55]. Experiments with RBCs in free-fibrinogen plasma show a decrease in the shear-thinning behavior and very low *rouleaux* formation [4, 7, 53, 54]. Another phenomena suggested to explain RBCs aggregation is a depletion effect, similar to what happens in colloidal polymer mixed solutions [54, 57]. Blood also exhibits a thixotropic behavior consisting in a viscosity decrease with time when subjected to a constant shear-rate. Blood thixotropy is associated with the aggregation/disaggregation of RBCs and with the intensity and time scales of the applied stresses [12, 17]. Also, when blood is subjected to an external deformation it can deform to a certain extent and, when the external forces ceases, the deformation is partially recovered due to its viscoelastic behavior [58].The viscoelasticity of blood is associated with its multiphase nature and with the morphological and elastic properties of the discrete phases, specifically the RBCs [17]. Although the elastic nature of blood is important, a recent study by Sousa et al. [59] measured the relaxation time of whole blood samples and concluded that the blood elasticity is weak.

1.3.2.1 Steady-state rheometry

In this thesis, steady-shear characterization of the blood analogue suspensions was carried out on a PHYSICA model MCR301 shear rheometer. The method of analysis is based on a Couette flow and allows the determination of the shear viscosity. There are other characteristics of the fluids that this equipment can obtain, but only the shear viscosity was explored. The protocol used to measure the shear viscosity of the blood analogues was the one implemented by Sousa et al. [56] for blood samples. The measurements were performed with a 50 mm diameter serrated plate–plate geometry, denoted as PP50/P2, using a gap of h_{gap} = 1 mm. The serrated plate has a structured roughness shape, with orthogonal protuberances of 1 mm height, which are useful to prevent slip effects in high concentrated suspensions. Also, this plate–plate geometry

delays the onset of inertial instabilities at the higher shear-rates [60]. The geometry is schematically represented in Figure 1.4. To reduce particle sedimentation and maintain the homogeneity of the sample, between each measurement and for shear rates ≤ 50 s^{-1}, a shear rate of 300 s^{-1} during 30 s was imposed [56].

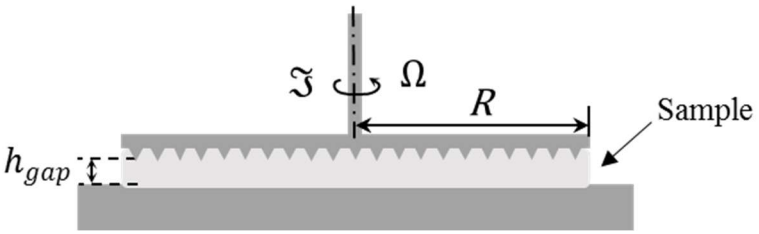

Figure 1.4. Schematic representation of the parallel plate geometry.

In a plate-plate arrangement the shear-rate, $\dot{\gamma}$,is given by:

$$\dot{\gamma} = \frac{\Omega R}{h_{gap}} \tag{1.1}$$

where Ω is the angular velocity and R the plate radius. The shear viscosity, $\mu(\dot{\gamma})$, is given by:

$$\mu(\dot{\gamma}) = \frac{1}{\dot{\gamma}} \frac{3\Im}{2\pi R^3} \left(1 + \frac{1}{3} \frac{\mathrm{d} \ln \Im}{\mathrm{d} \ln \dot{\gamma}}\right) \tag{1.2}$$

where $\Im$ is the torque.

At least three independent samples were measured in order to support the reproducibility of the results.

1.3.2.2 Extensional rheometry

Extensional flow enhances viscoelastic characteristics, due to a significant increase of the normal stresses [59]. The ideal flow to study extensional based properties is a purely uniaxial elongational flow [60]. The characteristic time scale of the normal

stresses growth in uniaxial elongational flows can be regarded as the relaxation time, λ.

For low-viscosity fluids, it is difficult to generate homogeneous elongational flows. The slow retraction method (SRM) developed by Campo and Clasen [61] was adopted, in this study, to measure the relaxation time of the blood analogue samples. The SRM is capable of measuring low relaxation times, as low as ~ 200 μs. In the SRM procedure, the sample is placed between two circular plates, which are separated by an initial distance h_i, Figure 1.5. At a given time, an axial step strain is imposed over a very long time (20 s and 50 s) until the final distance, h_f, is achieved, Figure 1.5. For this purpose, a capillary-breakup extensional rheometer, CaBER (Haake CaBER 1, Thermo Scientific), was used.

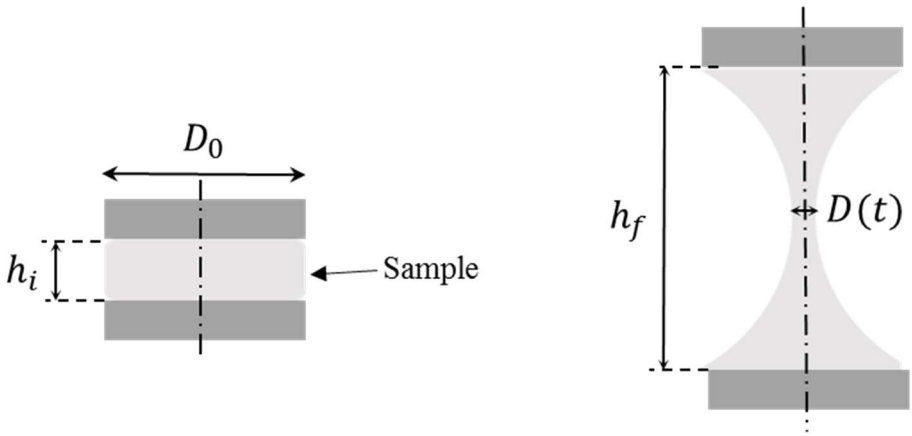

Figure 1.5. Schematic representation of an extensional flow: (left) sample at the initial instant and (right); sample being stretched in a uniaxial elongation flow.

Afterwards, the time evolution of the diameter of the filament $D(t)$, undergoing a capillary thinning process, is monitored by a high speed camera (FASTCAM Mini UX100). The relaxation time is calculated from the slope of the linear fit of the data of $\log[D(t)/D_0]$ *versus* time, t, (Eq. 1.2) in the region of elastic-capillary balance forces [55, 59, 62]:

$$\frac{D(t)}{D_0} = \mathrm{C}\, e^{\left(-\frac{t}{3\lambda}\right)} \tag{1.3}$$

where D_0 is the diameter of the filament at $t = 0$ and C is a constant, $\mathrm{C} = \lfloor G D_0/(4\,\sigma)\rfloor^{1/3}$, where G is the fluid elastic modulus.

At least three essays for each time evaluated, 20 s and 50 s, were carried out in order to support the reproducibility of the measurements.

1.3.3 Plasma Layer

Another important issue is the plasma layer formation in tubes with diameters less than about 300 μm [20, 63-66]. Mechanical interactions between RBCs and tube wall generally result in the formation of a plasma layer, cell-free layer (CFL), or a region of reduced hematocrits adjacent to the wall, increasing the concentration near the center of the tube [20, 63-66], Figure 1.7. This effect has significant consequences for the overall blood flow behavior in narrow tubes, including dynamic reduction of intravascular hematocrits (Fahraeus effect [63]), and reduction of the flow resistance below the level that would be expected based on the blood bulk viscosity (Fahraeus-Lindqvist effect[65]). The RBCs velocity is therefore higher than the average blood velocity [63-66].

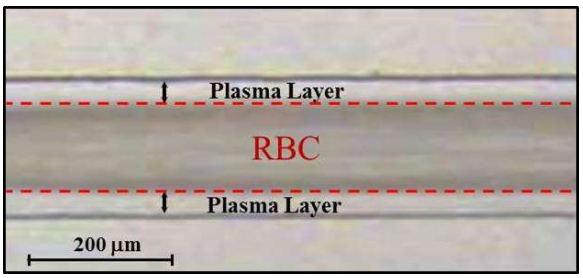

Figure 1.6. Plasma layer (near the channel wall) and RBCs core (center) in a planar microchannel. Adapted from [64].

1.4 Why PDMS microparticles?

PDMS is a silicone elastomer, chemically inert, thermally stable, permeable to gases and exhibits isotropic and homogeneous properties [45, 67]. Additionally, PDMS is transparent, nontoxic, biocompatible and has been frequently used in a wide range of medical equipments: catheters, drainage tubing, pacemakers, membrane oxygenators, and even for ear and nose implants [45, 68]. These properties, in combination with the low cost and suitability for mass-production, made PDMS a promising candidate material to produce microparticles to be employed in biomimetic suspensions such as blood. Also, PDMS microparticles have a relatively small refractive index, ~ 1.41, which matches the index of a large variety of fluids and also that of channels made in PDMS [69]. With this condition, optical techniques, such as Micro Particle Image Velocimetry (μPIV), can be performed in high density suspensions as well as in irregular circular shaped channels (see Chapter 4).

Chemically, PDMS is made of repeating silicon to oxygen bonds. The polymeric chain, Figure 1.7, is composed of silicon atoms linked to organic groups, usually methyl groups. This is the basis for the name "silicones" [68, 70]. The basic repeating unit became known as "siloxane" and the most common silicone is polydimethylsiloxane, abbreviated as PDMS [68].

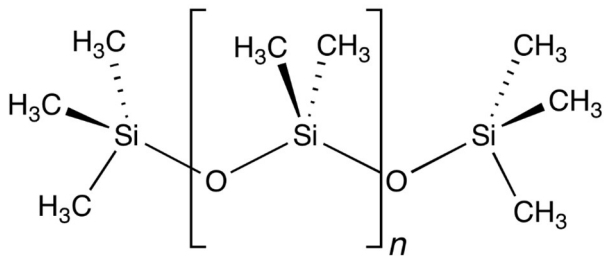

Figure 1.7. PDMS molecular structure.

The unique chemical structure of PDMS, with organic groups linked with an inorganic backbone gives to PDMS a combination of unique properties, making it possible to be use as fluid, emulsion, compound, resin, and elastomer. Depending on the size of the polymeric chain, non-cross-linked PDMS can be in the liquid state,

while, when cross-linked, the siloxane bonds result in a flexible polymer [71]. In this thesis, the PDMS precursor used was the Sylgard 184®. The PDMS precursor and a cross-linker, curing agent, are mixed at different ratios and afterwards the blend is thermally cross-linked. Other methods of polymer cross-linking exist and are well described elsewhere [72].

Methods to manufacture PDMS microparticles are found in the literature, as well as their wide range of applications: oxygen sensors [42], water treatment [73], gene delivery [74], rolling particle lithography [47], surface patterning [75], amphiphilic particles[76] and biomimetic fluids [46]. In Table 1.1 are summarized the works found about PDMS microparticles manufacture. The biggest disadvantage of using liquid PDMS as droplets material is its high viscosity. Note that the term "curing" referred along this thesis has the same meaning as cross-linking.

Table 1.1. Overview of PDMS microparticles manufacture, corresponding application and particle size found in the literature.

Method of preparation	Application	Size
Co-Flowing and photolithography	Amphiphilic particles [48]	~ 400-900 µm
Flow Focusing	Oxygen sensors [42]	~ 80 µm
	Particle lithography [47]	~ 50-220 µm
	Water treatment [73]	~ 620-740 µm
	Biomimetic fluids [46]	~ 3-20 µm
Mixing emulsification	Gene delivery [74]	~0.7-1 µm

The next two sections will be focused on the two main methods used in this work for the generation of PDMS droplets and microparticles - Sections 1.5 and 1.6.

1.5 Droplet-based microfluidics

1.5.1 Microfluidic devices

Microfluidics is a multidisciplinary topic with three decades of existence and it encloses a powerful platform for the generation of droplets and microparticles [26-37, 39-42, 77]. The

manipulation of small volumes of fluid at low Reynolds numbers and the ability to attain much faster reaction times, compared to macroscale systems, makes microfluidics an invaluable tool for a wide range of areas from engineering to biology [1-4]. Concerning micro-scale hemodynamics studies, microfluidic devices have been used as blood cells sorting and a platform to study blood analogues and healthy and pathological blood RBCs [8], to name a few.

Microfluidic devices can generate microscale droplets of one fluid within a second immiscible carrier fluid [3]. The ability to synthesize monodisperse droplets of controlled size and shape has numerous potential applications in areas such as: production of emulsions, drug delivery, catalysis, and medical imaging.

Droplet microfluidics includes active and passive methods. The main difference between these methods is on the external forces. Active droplet generators are usually accomplished by integrating additional forces into the microfluidic systems, such as: magnetic [78], pneumatic [79], electrical [80], thermal [81] and acoustic [82] forces. The active control offers more flexibility in manipulating droplets than passive droplet generation. However, the active methods suffer from difficulties in fabrication and miniaturization [83, 84]. This work will only be focused on passive methods.

In passive microfluidic devices, the hydrodynamic shear induced by the introduction of one immiscible fluid (dispersed fluid) into the bulk of another (continuous fluid) typically leads to the formation of droplets in one of two main flow regimes: dripping and jetting [48, 84-87]. When inertial forces are negligible, the main dimensionless parameters involved are:

- the flow rates ratio, $\varphi = Q_{\mathrm{d}}/Q_{\mathrm{c}}$;

- the viscosities ratio, $\chi = \mu_{\mathrm{d}}/\mu_{\mathrm{c}}$;

- and the capillary number of the dispersed phase (ratio between viscous and surface tension forces), $\mathrm{Ca_d} = \mu_{\mathrm{d}} U_{\mathrm{d}}/\sigma$.

where Q is the volumetric flow rate, μ the viscosity, U the inlet average velocity and σ the interfacial tension, The subscripts d and c refer to the dispersed and continuous phases, respectively.

Other dimensionless parameters such as Reynolds number (ratio between inertial and viscous forces,$\mathrm{Re} = \rho U h/\mu$ where h is the channel characteristic dimension), and

Weber number (ratio between inertial and surface tension forces, $We = \rho h U^2/\sigma$), are also important when the channel dimensions and / or U are sufficiently large for inertial forces to dominate viscous and surface tension forces. On this work $Re_d \ll 1$ and $We_d \ll 1$ and, therefore, inertia is not relevant.

The regimes and the dimensionless parameters involved in the droplets formation are well described in Chapters 2, 3 and 4.

Different configuration of microfluidic devices are used to generate droplets, being T – junction, flow focusing and co-flowing configurations the most common [26, 29, 34], Figure 1.8. In the T – junction, the dispersed phase is injected orthogonally to the continuous phase, Figure 1.8a. In the co-flowing configuration, the dispersed phase flows within and parallel to the continuous phase, Figure 1.8b. Both, T-junction and co-flowing geometries are capable of producing monodisperse droplets with size coefficients of variance (CV) lower than 3 % [84].

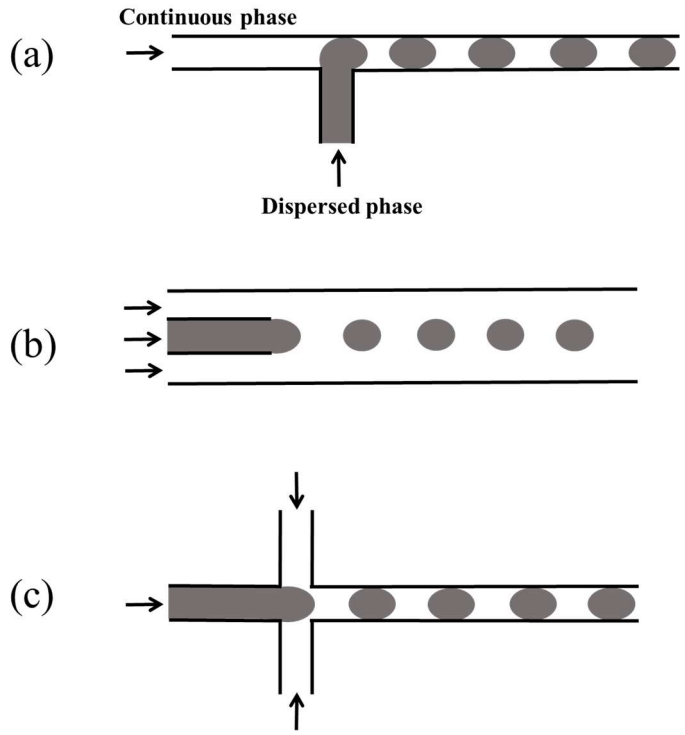

Figure 1.8. Schematic representation of different microfluidic devices: a) T-junction; b) co-flowing; and c) flow focusing. Arrows represent the flow direction.

To achieve both, small droplets and a low CV (< 5 %), microfluidic flow focusing devices are preferable [84]. In these devices, a dispersed phase (aqueous phase) is squeezed by two counter-flowing streams of a continuous phase [26, 29, 32, 35]. Both liquid phases, continuous and dispersed, are forced to flow through an outlet located downstream the three inlet channels, Figure 1.8c. The continuous phase forces the dispersed to flow in a narrow thread, breaking into droplets, Figure 1.8c. This configuration was chosen in this work to generate the PDMS microdroplets.

New techniques for increasing the generation rate of droplets production have recently been implemented by parallelizing microfluidic channels [88-90]. The parallelization is complex, expensive and only viscosities of the dispersed phase up to 30 mPa s^{-1} were tested [90]. Parallelization for highly viscous droplets formation requires a channel material able to withstand high pressures [90]. PDMS microchannels only withstand pressures up to ~ 70 Pa [91] being the average viscosity of the liquid PDMS pre-polymer ~ 640 mPa s^{-1} .For these reasons, an alternative method to scale-up the production of PDMS droplets is discussed in Section 1.6.

1.5.2 Microchannel fabrication

Microchannels developed for research are commonly fabricated in PDMS [26, 29, 34, 35, 43]. In this work, PDMS (Sylgard® 184) microchannels were fabricated using a soft lithography technique [44, 92] using SU-8 photoresist molds. This method is illustrated in Figure 1.9.

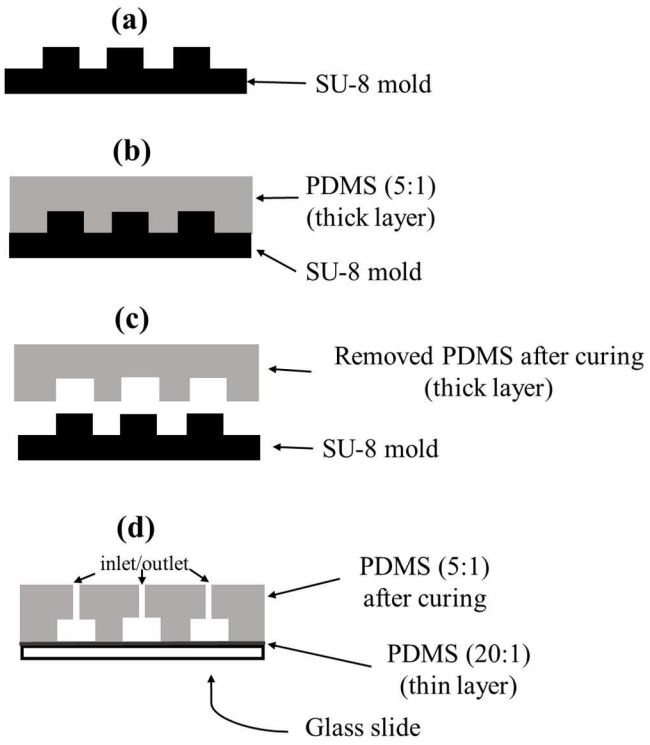

Figure 1.9. Overview of the PDMS microchannel fabrication procedure: a) Cross-section of a photoresist mold (SU-8) with a positive relief; b) The mixture of polymer oligomer with curing agent, prepared in a ratio of 5:1, is poured onto the SU-8 mold (thick layer) and placed in an oven to cure during 20 minutes; c) After curing, PDMS thick layer is removed from the SU-8 mold and access ports are created (inlets/outlets); d) The PDMS layer containing the channel structure is bonded to the glass slide covered with a thin layer of PDMS and placed in an oven to further seal the channel [60].

1.5.3 Wettability

When two immiscible fluids (liquid-liquid or gas-liquid) co-exist in a microfluidic system, the channels walls will have an affinity to be coated by one of the fluids rather than the other. This affinity is known as wettability. The wettability is defined by the contact angle of a liquid droplet at the three-phase boundary, i.e., where liquid, gas (or other liquid) and solid intersect, Figure 1.10. The angle, θ, between the solid and the tangent to the droplet surface at the intersection point is then the contact angle, Figure 1.10.

A contact angle greater than 90º reveals a hydrophobic solid material while a smaller than 90º a hydrophilic one, Figure 1.10 [93-96].

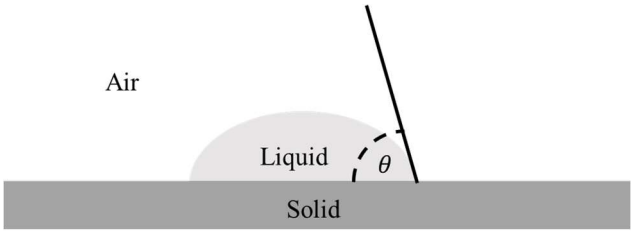

Figure 1.10. Schematic representation of the contact angle θ of a water liquid droplet in a solid surface. If θ is less than 90º the solid is hydrophilic.

The liquid PDMS pre-polymer will have affinity with the hydrophobic PDMS channels walls compromising the PDMS droplet formation. In order to change the hydrophobic nature of the PDMS channels, surface plasma oxidation treatment is required to replace the surface methyl groups, bounded to the silicon atom within the PDMS structure, by silanol groups (Si-OH), Figure 1.11 [43, 44, 94-98]. This technique relies on the use of an ionized gas to functionalize the microchannel walls surface. The key benefits of this technique are the short treatment time and the simple procedure, which make it one of the most efficient ways to modify a PDMS surface. An ongoing challenge with PDMS plasma oxidation is the hydrophobic recovery within hours (2-6 hours) caused by the migration of uncured PDMS oligomers from the bulk to the surface and the rearrangement of highly mobile polymer chains at room temperature to minimize the surface energy [97].

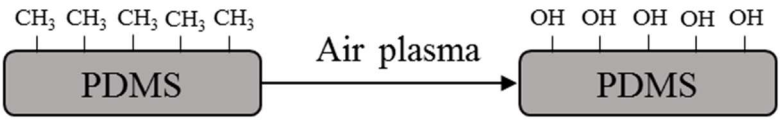

Figure 1.11. Schematic representation of the O_2 plasma treatment.

1.5.4 Surfactant

The term ‘surfactant’ derives from the contraction of ‘surface active agent’[99]. Surfactants are amphiphilic molecules frequently used to stabilize the droplet interface

in order to prevent droplets coalescence, a vital requirement in the droplet stabilization [26, 29, 34, 35, 42, 99]. Each surfactant has a hydrophilic head and a hydrophobic tail, Figure 1.12. The surfactants have different affinities for different immiscible phases. This characteristic drives the molecules to the newly formed droplet interface, reducing the interfacial tension.

By adding surfactant, the interfacial tension decreases until the critical micelle concentration (CMC) is reached [99-101], Figure 1.12. The CMC value is surfactant dependent. In dynamic conditions, mass transport limitations of the surfactant can occur. For example, with the stretching of a immiscible liquid thread, the adsorption rate of a surfactant can be lower than the rate of newly interface generation and consequently can appear zones, at the interface, with uneven surfactant adsorption [86, 99].

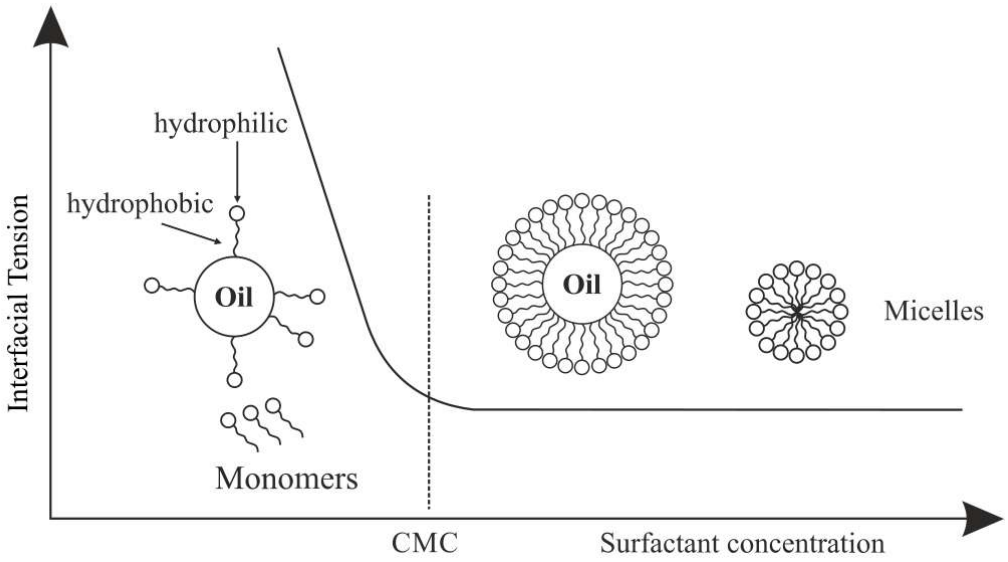

Figure 1.12. Effect of the surfactant concentration in the interfacial tension.

1.6 Membrane emulsification

In the early 1990s, membrane emulsification technique was proposed to produce fine emulsions at industrial scales [84]. Membrane emulsification can generate droplets at much higher throughput than microfluidics systems, but with the cost of

lower monodispersity (~ 20 %) [84, 102]. In membrane emulsification processes, the dispersed phase is forced through a porous membrane, after which droplets detach into the continuous phase, Figure 1.13. The membrane emulsification can be processed through two methods: direct membrane emulsification and premix membrane emulsification. In the direct membrane emulsification, a pure liquid (dispersed phase) is directly injected through a membrane into a second immiscible liquid (continuous phase), Figure 1.13a. In a premix emulsion, coarse droplets are homogenized by pressing the premixed emulsion through a membrane [84, 102, 103], Figure 1.13b. The advantage of premix is the capability of using higher dispersed phase fractions and achieve smaller droplets with higher throughputs [103]. However, in premix emulsification repeated passages through the membrane may be needed to better control the droplet size [102, 103]. Owing to the better control of the droplets size, the premix emulsification was the method adopted to produce PDMS microparticles in Chapter 5.

Different emulsification procedures are possible: rotation, cross-flow, stirring and vibration. [84, 103]. Membranes can be composed of different materials such as polymers, porous glass ceramic and metal [84, 102, 103]. The droplets size is affected by the membrane pore morphology, pore size distribution, porosity, spatial arrangement of the pores, surface wettability and charge, among other properties. In a similar manner to microfluidics, the membrane emulsification process is affected by the viscosity of the fluids, surfactant and dynamic parameters [103].

In Table 1.2 a comparison between flow focusing microfluidics and membrane emulsification processes is summarized.

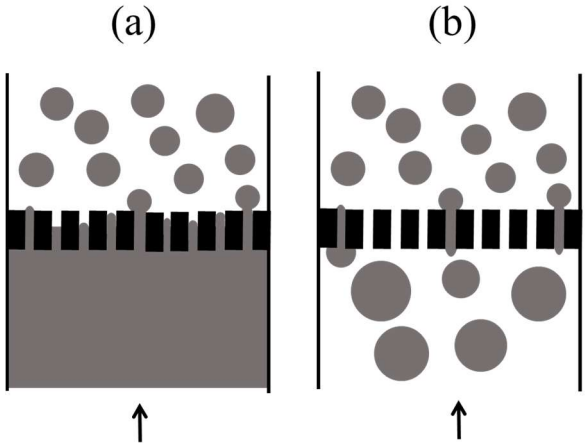

Figure 1.13. Schematic representation of the membrane emulsification process: a) direct and b) premix emulsification. Arrows represent the flow direction.

Table 1.2. Comparison between Flow Focusing Microfluidics and Membrane Emulsification processes.

Droplet Generation process	Minimum droplet size	Maximum Droplet Production rate	Monodispersivity
Flow Focusing Droplet Microfluidics	Several hundred nanometers [104]	~ tens of KHz [105]	CV < 5 % (dripping) [106] CV > 5% (jetting) [50]
Membrane Emulsification	~ 0.1 µm [102]	Tons of dispersed phase per hour [102]	CV ~ 20 % [107]

1.7 Computational Fluid Dynamics (CFD)

With the development of high performance computing and numerical procedures, the complex equations that govern the fluids flow can be accurately solved by Computational Fluid Dynamics (CFD) methods. CFD can convert the differential and other nonlinear equations representing the physical flow laws into algebraic equations to be solved by computers [108]. CFD can save time and resources and it is widely

used in the design process of flow systems, *e.g*, in chemical, automotive and aeronautical industries.

CFD offers important insights to understand the effects of the variables involved in droplets dynamic. In droplet microfluidics, several numerical methods have been proposed, each having its advantages and disadvantages[109].

The starting point of any numerical method is the description of the mathematical model, i.e., the definition of the differential equations that govern the flow (incompressible/compressible, inviscid/viscous, laminar/turbulent, 2D or 3D, etc) and the statement of the respective boundary conditions. For Newtonian and laminar flows, the momentum and continuity equations are written as:

$$\frac{\partial(\rho\vec{v})}{\partial t} + \nabla\cdot(\rho\vec{v}\vec{v}) = -\nabla\vec{p} + \nabla\cdot[\mu(\nabla\vec{v} + \nabla\vec{v}^{\mathrm{T}})] + \overrightarrow{f_\sigma} \tag{1.4}$$

$$\nabla\cdot\vec{v} = 0 \tag{1.5}$$

where p is the pressure, $\vec{v}$ the velocity vector, μ the dynamic viscosity of the fluid and $\overrightarrow{f_\sigma}$ represents the surface tension force.

Afterwards, it is necessary a spatial and sometimes a temporal discretization of the differential equations. The algebraic discretized equations are then solved. The solution is determined for all the points in the domain and, sometimes, as function of time [110, 111].

In terms of CFD software, there are several packages available, *i.e* OpenFOAM, Palabos, COMSOL, STAR-CCM+ and ANSYS Fluent. Among all the existing options, ANSYS Fluent was the software chosen to solve the numerical scenarios addressed in this thesis as it is user-friendly, has very robust volume of fluid methods and produces satisfactory results. The discretization approach implemented in Ansys Fluent is the finite volume method (FVM). In a FVM, the computational domain is divided in control volumes and conservation principles are applied to each control volume. This guarantees conservation, both, in each cell and globally in the domain.

For solving multiphase flows, ANSYS Fluent offers two methods for the flow simulation of incompressible immiscible fluids, with the capability of tracking topological changes of the interface: the volume of fluid method (VOF) and a coupled level-set (LS) and VOF methods (CLSVOF).

The (VOF) method, firstly proposed by Hirt and Nichols [112], is widely used to simulate multiphase flows. This method introduces an indicator function, to track the volume fractions of the different fluids in each control volume cell. In two-phase flows, the indicator function,α, is the volume fraction of one of the two phases. The function α has value one or zero, depending when the control volume is entirely filled with one of the phases or a value between one and zero if the interface crosses the control volume (Figure 1.14):

$$\boldsymbol{\alpha(\vec{x},t)} = \begin{cases} \mathbf{0} & \alpha = 0 \text{ continuous phase} \\ \mathbf{0 < \alpha < 1} & 0 < \alpha < 1 \text{ interface inside the control volume} \\ \mathbf{1} & \alpha = 1 \text{ dispersed phase} \end{cases} \tag{1.4}$$

where $\vec{x}$ is the position vector.

. The VOF advective equation is as follows:

$$\frac{\partial \alpha}{\partial t} + \nabla \cdot (\alpha \vec{v}) = 0 \tag{1.5}$$

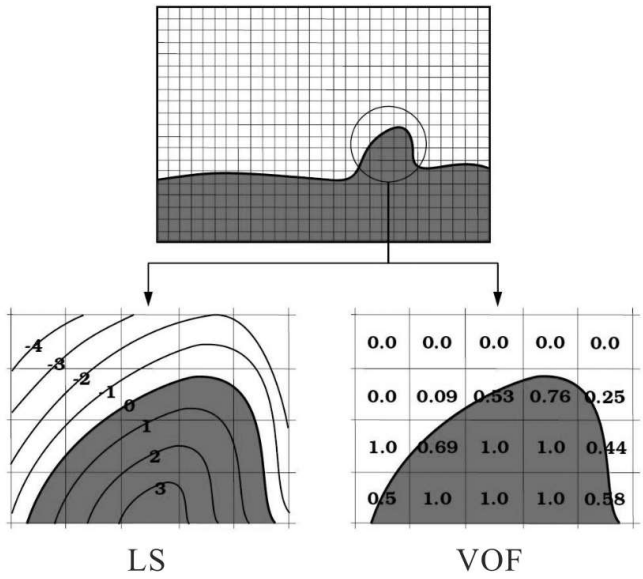

Figure 1.14. Illustration of the LS (left) and VOF (right) methods. Adapted from Berberović [113].

Sometimes, with VOF method, it is difficult to obtain the accurate curvature and smoothed physical properties at the interface. Although the interface is reconstructed every time step by a Piecewise Linear Interpolation Calculation scheme (PLIC) [114], it can happen sharp transitions of the volume fraction in some regions of the interface [115].

On the other hand, the discontinue nature of the VOF method can cause the presence of artificial spurious (or parasitic) currents [116] , which originate errors in the prediction of the interface curvature. These currents are originated by an imbalance between the discrete surface tension force, $\overrightarrow{f_\sigma}$, and the pressure-gradient , $\nabla\vec{p}$, Eq. (***1.4***) [116-121]. These errors proliferate dramatically into the velocity field at small capillary numbers, $\mathrm{Ca} < 0.01$, Figure 1.15 [122, 123]. For this reason, they are very likely to appear in the simulations of microfluidic systems operating at very low Ca. Spurious currents can be reduced by using a level-set function and/or a weighting function [121, 124]. A more detailed description of the surface tension force and a method to suppress spurious currents can be found in Chapter 3.

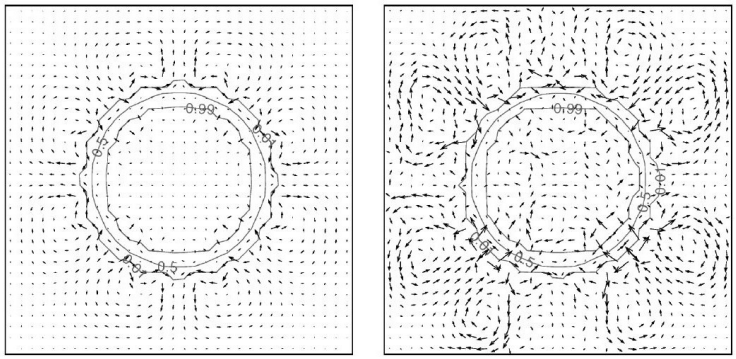

Figure 1.15. Vector map of the spurious currents in a stationary two-dimensional droplet. The contours represent the lines of constant volume fraction: $\mathrm{Ca} = 2.5 \times 10^{-4}$ (left) and $\mathrm{Ca} = 2.5 \times 10^{-5}$. Adapted from Harvie et al. Harvie, Davidson [116].

In the level-set (LS) method, first presented Osher and Sethian [125], a continuous smooth function is set throughout the computational domain as a signed distance from a point to the interface, ϕ; positive in one phase and negative in the other, with the value of zero at the interface, Eq. (1.7) and Figure 1.14.

The LS advective equation is as follows:

$$\frac{\partial \phi}{\partial t} + \vec{v} \cdot \nabla \phi = 0 \tag{1.6}$$

and the LS function, ϕ :

$$\phi(\vec{x}, t) = \begin{cases} +d & \text{if } \vec{x} \in \text{dispersed phase} \\ 0 & \text{if } \vec{x} \in \text{interface} \\ -d & \text{if } \vec{x} \in \text{continuous phase} \end{cases} \tag{1.7}$$

where d is the distance from a point to the interface.

In contrast to the volume fraction, this function is just an indicator with no physical meaning. Therefore, the level set function, does not need to satisfy the mass conservation law but requires re-initialization procedures in every time step to control the mass loss [113, 115, 121].

In this thesis, we chose a coupled LS and VOF method (CLSVOF), first introduced by Sussman and Puckett [115], in order to overcome the deficiencies of both, VOF and LS methods. The CLSVOF method is currently available in ANSYS FLUENT software (since Release 13.0, ANSYS Inc., USA).

The CLSVOF model is able to capture the interface curvature accurately due to the LS method and to satisfy the mass conservation equation due to the VOF method. A more detailed description of the CLSVOF model can be found in Chapter 3.

1.8 Thesis Outline

Following the present introductory chapter, the results are divided in four chapters, each one based on a paper published or under review in scientific journals:

- Chapter 2: Carneiro J, Doutel E, Campos JBLM, Miranda JM. '*PDMS droplet formation and characterization by hydrodynamic flow focusing technique in a PDMS square microchannel'*, 2016, published in Journal of Micromechanics and Microengineering.
- Chapter 3: Carneiro J, Campos JBLM, Miranda JM. '*High viscosity polymeric fluid droplet formation in a flow focusing microfluidic device – Experimental and numerical study'*, 2019, published in Chemical Engineering Science.
- Chapter 4: Carneiro J, Campos JBLM, Miranda JM. '*PDMS microparticles produced in PDMS microchannels under the jetting regime for optimal optical suspensions'*, 2019, published in Colloids and Surfaces A: Physicochemical and Engineering Aspects.
- Chapter 5: Carneiro J, Campos JBLM, Miranda JM. '*Microparticle blood analogue suspensions covering a wide hematocrit range'* under review in Soft Matter.

In Chapter 2, the generation of PDMS droplets by hydrodynamic flow focusing in a PDMS square section microchannel is reported. The challenges of generating polymeric droplets in a microchannel of the same material are described, as well as the flow characterization to generate them. Different flow regimes were found: dripping,

jetting, threading and viscous displacement. Also, droplet size, breakup distance and formation frequency were analysed and quantified for the jetting and dripping regimes. Only the dripping and jetting regimes were capable of producing droplets. This study was the first approach to establish the ideal flow conditions and boundaries to produce droplets of PDMS in a flow focusing microfluidic system.

Since high viscous droplets are very difficult to generate in microfluidic systems, a numerical study, complemented by an experimental one, was performed, Chapter 3, using the same multiphase system described in Chapter 2. CFD can save time and resources for future studies, previewing experimental results. Numerical and experimental data from three flow regimes (threading, dripping and jetting) were examined in order to validate the numerical code. The results were also compared to correlations from the literature.

The first two studies presented in this thesis, Chapters 2 and 3, were of outmost importance for the next studies presented in Chapter 4 and 5, since they were able to provide an important insight on the conditions to produce RBCs size PDMS microparticles.

In Chapter 4, it is described the production of PDMS sub-channel size microparticles in the same microfluidic system reported in Chapters 2 and 3. Droplets are produced in the jetting regime and, afterwards, thermally cured. The microparticles were chemically and optically characterized.

The throughput and microparticles size were still insufficient to produce the volumes necessary to conduct a rheological characterization and so the next obvious step was the scale–up by parallelization of the droplets formation. The microfluidic parallelization process was studied and presented several limitations, discussed in Chapter 1, section 1.5. Consequently, an alternative method to produce PDMS microdroplets with RBCs size is presented in Chapter 5. The method is based in a multistep membrane emulsification process. Membrane emulsification was capable of dealing with the high viscosity dispersed phase and enabled a high throughput droplets generation.

Finally, in Chapter 6, the contributions from this thesis are summarized and some suggestions for future work are disclosed.

A preliminary study regarding the production of PDMS microparticles was added to the appendix section: Carneiro J, Doutel E, Campos JBLM, Miranda JM. '*Visualization of PDMS Microparticles Formation for Biomimetic Fluids'*, 2015, published in Micro and Nanosystems.

Notation

Latin	Definition	Units
CV	Coefficient of variance	(%)
d	Distance from a point to the interface	(m)
$D(t)$	Diameter of the filament of the capillary thinning process at t	(m)
D_0	Diameter of the filament at $t = 0$	(m)
$\overrightarrow{f_\sigma}$	Surface tension force term	(N m^{-1})
G	Elastic modulus	(Pa)
h	Channel characteristic dimension	(m)
h_{gap}	Gap between plates	(m)
h_i	Initial distance between two circular plates	(m)
h_f	Final distance between two circular plates	(m)
p	Pressure	(Pa)
Q	Volumetric flow rate	(m^3 s^{-1})
Q_c	Volumetric flow rate of the continuous phase	(m^3 s^{-1})
Q_d	Volumetric flow rate of the dispersed phase	(m^3 s^{-1})
R	Plate radius	(m)
t	Time	(s)

U	Velocity	(m s^{-1})
U_c	Velocity of the continuous phase	(m s^{-1})
U_d	Velocity of the dispersed phase	(m s^{-1})
$\vec{v}$	Velocity vector	(m s^{-1})
$\vec{x}$	Vector position	(m)
$\vec{p}$	Pressure vector	(Pa s)

Greek	**Definition**	**Units**
α	Volume fraction	---
$\dot{\gamma}$	Shear rate	(s^{-1})
θ	Contact angle	(º)
λ	Relation time	(s)
μ	Dynamic viscosity	(Pa s)
μ_c	Dynamic viscosity of the continuous phase	(Pa s)
μ_d	Dynamic viscosity of the dispersed phase	(Pa s)
ρ	Fluid density	(kg m^{-3})
σ	Interfacial tension	(N m^{-1})
$\Im$	Torque	(N m)
φ	Volumetric flow rates ratio	---
ϕ	Signed distance from a point to the interface	---
χ	Viscosity ratio	---
Ω	Angular velocity	(rad s^{-1})

Dimensionless numbers	Definition
C	Relaxation time constant
Ca	Capillary number
Ca_c	Capillary number of the continuous phase
Ca_d	Capillary number of the dispersed phase
Re	Reynolds number
Re_d	Reynolds number of the dispersed phase
We	Weber number
We_d	Weber number of the dispersed phase

Acronyms	Definition
CEFT	Transport Phenomena Research Center
CFD	Computational Fluid Dynamics
CFL	Cell-free layer
CLSVOF	Coupled level-set and volume of fluid method
CMC	Critical micelle concentration
CVD	Cardiovascular diseases
DMSO	Dimethyl sulfoxide
FVM	Finite volume method
LS	Level-set method
PDMS	Polydimethylsiloxane
PDMS	Polydimethylsiloxane
PLIC	Piecewise Linear Interpolation Calculation

RBC	Red blood cell
SRM	Slow retraction method
SU-8	Designation of epoxi-bored photoresist
VOF	Volume of fluid method
μPIV	Micro Particle Image Velocimetry

References

1. Lozano, R., et al., *Global and regional mortality from 235 causes of death for 20 age groups in 1990 and 2010: a systematic analysis for the Global Burden of Disease Study 2010.* The Lancet, 2012. **380**(9859): p. 2095-2128.
2. E.D. Costa, J.C., M.S.N. Oliveira, J.B.L.M. Campos, J.M. Miranda, *Fabrication of mili-scale channels for hemodynamic studies*, in *ICEM15 - 15th International Conference on Experimental Mechanics*. 2012: Porto, Faculty of Engineering, University of Porto.
3. Dintenfa, L., *Blood rheology as diagnostic and predictive tool in cardiovascular-diseases - effects of ABO blood-groups.* Angiology, 1974. **25**(6): p. 365-372.
4. Robertson, A., A. Sequeira, and M. Kameneva, *Hemorheology*, in *Hemodynamical Flows*. 2008, Birkhäuser Basel. p. 63-120.
5. McHedlishvili, G. and N. Maeda, *Blood Flow Structure Related to Red Cell Flow: Determinant of Blood Fluidity in Narrow Microvessels.* The Japanese Journal of Physiology, 2001. **51**(1): p. 19-30.
6. Brust, M., *Rheological Properties of Red Blood Cells*. 2013, Franco-German University. p. 118.
7. Brust, M., et al., *The plasma protein fibrinogen stabilizes clusters of red blood cells in microcapillary flows.* Sci. Rep., 2014. **4**.
8. Pinho, D., et al., *In vitro particulate analogue fluids for experimental studies of rheological and hemorheological behavior of glucose-rich RBC suspensions.* Biomicrofluidics, 2017. **11**(5): p. 054105-054105.
9. Berger, S.A. and B.E. Carlson. *Sickle cell blood flow in the microcirculation*. in *The 26th Annual International Conference of the IEEE Engineering in Medicine and Biology Society*. 2004.
10. Benis, A.M. and J. Lacoste, *Study of erythrocyte aggregation by blood viscometry at low shear rates using a balance method.* Circulation Research, 1968. **22**(1): p. 29-41.
11. Chien, S., *Shear dependence of effective cell volume as a determinant of blood viscosity.* Science, 1970. **168**(3934): p. 977-979.
12. Thurston, G.B., *Rheological parameters for the viscosity viscoelasticity and thixotropy of blood.* Biorheology, 1979. **16**(3): p. 149-62.
13. Pirofsky, B., *The determination of blood viscosity in man by a method based on Poiseuille's law.* The Journal of clinical investigation, 1953. **32**(4): p. 292-298.
14. Picart, C., et al., *Human blood shear yield stress and its hematocrit dependence.* Journal of Rheology, 1998. **42**(1): p. 1-12.

15. Travagli, V., et al., *Comparison of blood viscosity using a torsional oscillation viscometer and a rheometer.* Clinical Hemorheology and Microcirculation, 2008. **38**(2): p. 65-74.

16. Baskurt, O.K., et al., *New guidelines for hemorheological laboratory techniques.* Clinical Hemorheology And Microcirculation, 2009. **42**(2): p. 75-97.

17. Sousa, P.C., et al., *A review of hemorheology: Measuring techniques and recent advances.* Korea-Australia Rheology Journal, 2016. **28**(1): p. 1-22.

18. Sousa, P.C., et al., *Flow of a Blood Analogue Solution Through Microfabricated Hyperbolic Contractions*, in *Computational Vision and Medical Image Processing*, J.M.R.S. Tavares and R.M.N. Jorge, Editors. 2011, Springer Netherlands. p. 265-279.

19. Campo-Deaño, L., et al., *Viscoelasticity of blood and viscoelastic blood analogues for use in polydymethylsiloxane in vitro models of the circulatory system.* Biomicrofluidics, 2013. **7**(3): p. -.

20. Lima, R., et al., *In vitro blood flow in a rectangular PDMS microchannel: experimental observations using a confocal micro-PIV system.* Biomedical Microdevices, 2008. **10**(2): p. 153-167.

21. Aziz, A.U.R., et al., *The Role of Microfluidics for Organ on Chip Simulations.* Bioengineering (Basel, Switzerland), 2017. **4**(2): p. 39.

22. Catarino, S.O., et al., *Blood Cells Separation and Sorting Techniques of Passive Microfluidic Devices: From Fabrication to Applications.* Micromachines, 2019. **10**(9): p. 593.

23. Martínez-Aranda, S., F.J. Galindo-Rosales, and L. Campo-Deaño, *Complex flow dynamics around 3D microbot prototypes.* Soft Matter, 2016. **12**(8): p. 2334-2347.

24. Bento, D., et al., *Microbubble moving in blood flow in microchannels: effect on the cell-free layer and cell local concentration.* Biomedical Microdevices, 2017. **19**(1): p. 6.

25. Doutel, E., et al., *Geometrical effects in the hemodynamics of stenotic and non-stenotic left coronary arteries—numerical and in vitro approaches.* International Journal for Numerical Methods in Biomedical Engineering, 2019. **35**(8): p. e3207.

26. Teh, S.-Y., et al., *Droplet microfluidics.* Lab on a Chip, 2008. **8**(2): p. 198-198.

27. Dendukuri, D., et al., *Continuous-flow lithography for high-throughput microparticle synthesis.* Nat Mater, 2006. **5**(5): p. 365-369.

28. Xu, S., et al., *Generation of Monodisperse Particles by Using Microfluidics: Control over Size, Shape, and Composition.* Angewandte Chemie International Edition, 2005. **44**(5): p. 724-728.

29. Baroud, C.N., et al., *Dynamics of microfluidic droplets.* Lab on a Chip, 2010. **10**(16): p. 2032-2032.

30. Peng Lee, C., Y. Hsin Chen, and Z. Hang Wei, *Fabrication of hexagonally packed cell culture substrates using droplet formation in a T-shaped microfluidic junction.* Biomicrofluidics, 2013. **7**(1).

31. Utada, A.S., et al., *Dripping to Jetting Transitions in Coflowing Liquid Streams.* Physical Review Letters, 2007. **99**(9): p. 094502-094502.

32. Anna, S.L., N. Bontoux, and H.A. Stone, *Formation of dispersions using "flow focusing" in microchannels.* Applied Physics Letters, 2003. **82**(3): p. 364-366.

33. Dufaud, O., E. Favre, and V. Sadtler, *Porous elastomeric beads from crosslinked emulsions.* Journal of Applied Polymer Science, 2002. **83**(5): p. 967-971.

34. Dendukuri, D. and P.S. Doyle, *The synthesis and assembly of polymeric microparticles using microfluidics.* Advanced Materials, 2009. **21**(41): p. 4071-4086.

35. Todd, P.L. and F.E. Jon, *A review of the theory, methods and recent applications of high-throughput single-cell droplet microfluidics.* Journal of Physics D: Applied Physics, 2013. **46**(11): p. 114005.

36. Garstecki, P., H.A. Stone, and G.M. Whitesides, *Mechanism for Flow-Rate Controlled Breakup in Confined Geometries: A Route to Monodisperse Emulsions.* Physical Review Letters, 2005. **94**(16): p. 164501.

37. Christian, H., *Large-scale droplet production in microfluidic devices—an industrial perspective.* Journal of Physics D: Applied Physics, 2013. **46**(11): p. 114008.

38. Garstecki, P., et al., *Formation of droplets and bubbles in a microfluidic T-junction-scaling and mechanism of break-up.* Lab on a Chip, 2006. **6**(3): p. 437-446.

39. Nie, Z., et al., *Emulsification in a microfluidic flow-focusing device: effect of the viscosities of the liquids.* Microfluidics and Nanofluidics, 2008. **5**(5): p. 585-594.

40. Tran, T.M., S. Cater, and A.R. Abate, *Coaxial flow focusing in poly(dimethylsiloxane) microfluidic devices.* Biomicrofluidics, 2014. **8**(1).

41. Takeuchi, S., et al., *An Axisymmetric Flow-Focusing Microfluidic Device.* Advanced Materials, 2005. **17**(8): p. 1067-1072.

42. Jiang, K., et al., *Microfluidic synthesis of monodisperse PDMS microbeads as discrete oxygen sensors.* Soft Matter, 2012. **8**(4): p. 923-926.

43. Mata, A., A. Fleischman, and S. Roy, *Characterization of Polydimethylsiloxane (PDMS) Properties for Biomedical Micro/Nanosystems.* Biomedical Microdevices, 2005. **7**(4): p. 281-293.

44. Friend, J. and L. Yeo, *Fabrication of microfluidic devices using polydimethylsiloxane.* Biomicrofluidics, 2010. **4**(2).

45. Mata, A., A.J. Fleischman, and S. Roy, *Characterization of polydimethylsiloxane (PDMS) properties for biomedical micro/nanosystems.* Biomedical microdevices, 2005. **7**(4): p. 281-293.

46. Muñoz-Sánchez, B.N., et al., *Generation of micro-sized PDMS particles by a flow focusing technique for biomicrofluidics applications.* Biomicrofluidics, 2016. **10**(1): p. 1-11.

47. Di Benedetto, F., et al., *Rolling particle lithography by soft polymer microparticles.* Soft Matter, 2013. **9**(7): p. 2206-2206.

48. Zhao, L.-B., et al., *A novel method for generation of amphiphilic PDMS particles by selective modification.* Microfluidics and Nanofluidics, 2011. **10**(2): p. 453-458.

49. Carneiro, J., et al., *PDMS droplet formation and characterization by hydrodynamic flow focusing technique in a PDMS square microchannel.* Journal of Micromechanics and Microengineering, 2016. **26**(10): p. 105013-105013.

50. Carneiro, J., J.B.L.M. Campos, and J.M. Miranda, *High viscosity polymeric fluid droplet formation in a flow focusing microfluidic device – Experimental and numerical study.* Chemical Engineering Science, 2019. **195**: p. 442-454.

51. Popel, A.S. and P.C. Johnson, *Microcirculation and hemorheology*, in *Annual Review of Fluid Mechanics*. 2005, Annual Reviews: Palo Alto. p. 43-69.

52. Fedosov, D.A., et al., *Predicting human blood viscosity in silico.* Proceedings of the National Academy of Sciences, 2011. **108**(29): p. 11772-11777.

53. Kim, Y., K. Kim, and Y. Park, *Measurement Techniques for Red Blood Cell Deformability: Recent Advances*. Blood Cell - An Overview of Studies in Hematology. 2012.

54. Wagner, C., P. Steffen, and S. Svetina, *Aggregation of red blood cells: From rouleaux to clot formation.* Comptes Rendus Physique, 2013. **14**(6): p. 459-469.

55. Brust, M., et al., *Rheology of Human Blood Plasma: Viscoelastic Versus Newtonian Behavior.* Physical Review Letters, 2013. **110**(7): p. 078305.

56. Sousa, P.C., et al., *Shear viscosity and nonlinear behavior of whole blood under large amplitude oscillatory shear.* Biorheology, 2013. **50**(5-6): p. 269-282.

57. Asakura, S. and F. Oosawa, *Interaction between particles suspended in solutions of macromolecules.* Journal of Polymer Science, 1958. **33**(126): p. 183-192.

58. Thurston, G.B., *Viscoelasticity of human blood.* Biophysical journal, 1972. **12**(9): p. 1205-1217.

59. Sousa, P.C., et al., *Rheological behavior of human blood in uniaxial extensional flow.* Journal of Rheology, 2018. **62**(2): p. 447-456.

60. Sousa, P.C.S.d., *Entry flow of viscoelastic fluids at macro- and micro-scale*, in *Engenharia Química e Biológica. Faculdade de Engenharia. Universidade do Porto*. 2010, Faculdade de Engenharia da Universidade do Porto. p. 303.

61. Campo-Deaño, L. and C. Clasen, *The slow retraction method (SRM) for the determination of ultra-short relaxation times in capillary breakup extensional rheometry experiments.* Journal of Non-Newtonian Fluid Mechanics, 2010. **165**(23): p. 1688-1699.

62. Entov, V.M. and E.J. Hinch, *Effect of a spectrum of relaxation times on the capillary thinning of a filament of elastic liquid.* Journal of Non-Newtonian Fluid Mechanics, 1997. **72**(1): p. 31-53.

63. Fåhraeus, R., *The suspension stability of the blood*. Vol. 9. 1929. 241-274.

64. Sollier, E., et al., *Fast and continuous plasma extraction from whole human blood based on expanding cell-free layer devices.* Biomedical Microdevices, 2010. **12**(3): p. 485-497.

65. Lindqvist, R.F.T., *The viscosity of the blood in narrow capillary tubes.* American Journal of Physiology, 1931. **96**: p. 562-568.

66. Pries, A.R., T.W. Secomb, and P. Gaehtgens, *Biophysical aspects of blood flow in the microvasculature.* Cardiovascular Research, 1996. **32**(4): p. 654-667.

67. Unger, M.A., et al., *Monolithic Microfabricated Valves and Pumps by Multilayer Soft Lithography.* Science, 2000. **288**(5463): p. 113.

68. Ratner, B.D., *Biomaterials science : an introduction to materials in medicine*. 2004, Amsterdam; Boston: Elsevier Academic Press.

69. McDonald, J.C. and G.M. Whitesides, *Poly(dimethylsiloxane) as a Material for Fabricating Microfluidic Devices.* Accounts of Chemical Research, 2002. **35**(7): p. 491-499.

70. Thomas, N.R., *Frederic Stanley Kipping—Pioneer in Silicon Chemistry: His Life & Legacy.* Silicon, 2010. **2**(4): p. 187-193.

71. Fincan, M., *Assessing Viscoelastic Properties of Polydimethylsiloxane (PDMS) Using Loading and Unloading of the Macroscopic Compression Test*. 2015.

72. Fried, J.R., *Polymer science technology*. 2013, Upper Saddle River, New Jersey: Prentice Hall.

73. Lian, Z., et al., *Microfluidic fabrication of porous polydimethylsiloxane microparticles for the treatment of toluene-contaminated water.* Microfluidics and Nanofluidics, 2018. **22**(12): p. 145.

74. Choi, Y.H., et al., *Production of PDMS microparticles by emulsification of two phases and their potential biological application.* International Journal of Polymeric Materials and Polymeric Biomaterials, 2018. **67**(11): p. 686-692.

75. Yin, J., et al., *Surface Wrinkling on Polydimethylsiloxane Microspheres via Wet Surface Chemical Oxidation.* Scientific Reports, 2014. **4**: p. 5710.

76. Zhao, L., et al., *A novel method for generation of amphiphilic PDMS particles by selective modification.* Microfluidics and Nanofluidics, 2011. **10**: p. 453-458.

77. Garstecki, P., et al., *Formation of droplets and bubbles in a microfluidic T-junction—scaling and mechanism of break-up.* Lab on a Chip, 2006. **6**(3): p. 437-437.

78. Tan, S.h. and N.-T. Nguyen, *Generation and manipulation of monodispersed ferrofluid emulsions: The effect of a uniform magnetic field in flow-focusing and T-junction configurations.* Physical review. E, Statistical, nonlinear, and soft matter physics, 2011. **84**: p. 036317.

79. Zeng, S., et al., *Microvalve-actuated precise control of individual droplets in microfluidic devices.* Lab on a Chip, 2009. **9**(10): p. 1340-1343.

80. Tan, S.H., et al., *The Microfluidic Jukebox.* Scientific Reports, 2014. **4**: p. 4787.

81. Tan, S.-H., et al., *Thermally controlled droplet formation in flow focusing geometry: formation regimes and effect of nanoparticle suspension.* Journal of Physics D: Applied Physics, 2008. **41**(16): p. 165501.

82. Ma, Z., et al., *Self-Aligned Interdigitated Transducers for Acoustofluidics.* Micromachines, 2016. **7**(12): p. 216.

83. Wang, J., et al., *Droplet Microfluidics for the Production of Microparticles and Nanoparticles.* Micromachines, 2017. **8**(1): p. 22.

84. Zhu, P. and L. Wang, *Passive and active droplet generation with microfluidics: a review.* Lab Chip, 2017. **17**(1): p. 34-75.

85. Nunes, J.K., et al., *Dripping and jetting in microfluidic multiphase flows applied to particle and fibre synthesis.* J. Phys. D Appl. Phys., 2013. **46**(11): p. 114002-114002.

86. Anna, S.L., *Droplets and Bubbles in Microfluidic Devices.* Annual Review of Fluid Mechanics, 2016. **48**(1): p. 285-309.

87. Fu, T., et al., *Droplet formation and breakup dynamics in microfluidic flow-focusing devices: From dripping to jetting.* Chemical Engineering Science, 2012. **84**: p. 207-217.

88. Conchouso, D., et al., *Three-dimensional parallelization of microfluidic droplet generators for a litre per hour volume production of single emulsions.* Lab on a Chip, 2014. **14**(16): p. 3011-3020.

89. Yadavali, S., D. Lee, and D. Issadore, *Robust Microfabrication of Highly Parallelized Three-Dimensional Microfluidics on Silicon.* bioRxiv, 2019: p. 625277.

90. Yadavali, S., et al., *Silicon and glass very large scale microfluidic droplet integration for terascale generation of polymer microparticles.* Nature Communications, 2018. **9**(1): p. 1222.

91. Kang, J.H., Y.C. Kim, and J.-K. Park, *Analysis of pressure-driven air bubble elimination in a microfluidic device.* Lab on a Chip, 2008. **8**(1): p. 176-178.

92. Xia, Y. and G.M. Whitesides, *Soft Lithography.* Annual Review of Materials Science, 1998. **28**(1): p. 153-184.

93. Abate, A.R., et al., *Patterning microfluidic device wettability using flow confinement.* Lab on a Chip, 2010. **10**(14): p. 1774-1776.

94. Bodas, D. and C. Khan-Malek, *Formation of more stable hydrophilic surfaces of PDMS by plasma and chemical treatments.* Microelectronic Engineering, 2006. **83**(4–9): p. 1277-1279.

95. Bodas, D. and C. Khan-Malek, *Hydrophilization and hydrophobic recovery of PDMS by oxygen plasma and chemical treatment—An SEM investigation.* Sensors and Actuators B: Chemical, 2007. **123**(1): p. 368-373.

96. Tan, S.H., et al., *Oxygen plasma treatment for reducing hydrophobicity of a sealed polydimethylsiloxane microchannel.* Biomicrofluidics, 2010. **4**(3).

97. Zhou, J., et al., *Surface modification for PDMS-based microfluidic devices.* ELECTROPHORESIS, 2012. **33**(1): p. 89-104.

98. Kaneda, S., et al., *Modification of the Glass Surface Property in PDMS-Glass Hybrid Microfluidic Devices.* Analytical Sciences, 2012. **28**(1): p. 39-39.

99. Baret, J.-C., *Surfactants in droplet-based microfluidics.* Lab on a Chip, 2012. **12**(3): p. 422-433.

100. Farn, R.J., *Chemistry and Technology of Surfactants*. 2008: Wiley.

101. Tostado, C.P., J. Xu, and G. Luo, *The effects of hydrophilic surfactant concentration and flow ratio on dynamic wetting in a T-junction microfluidic device.* Chemical Engineering Journal, 2011. **171**(3): p. 1340-1347.

102. Vladisavljević, G.T., I. Kobayashi, and M. Nakajima, *Production of uniform droplets using membrane, microchannel and microfluidic emulsification devices.* Microfluidics and Nanofluidics, 2012. **13**(1): p. 151-178.

103. Nazir, A., K. Schroën, and R. Boom, *Premix emulsification: A review.* Journal of Membrane Science, 2010. **362**(1): p. 1-11.

104. Gañán-Calvo, A., et al., *Focusing Capillary Jets Close to the Continuum Limit.* Nature Physics, 2007. **3**: p. 737-742.

105. Yobas, L., et al., *High-performance flow-focusing geometry for spontaneous generation of monodispersed droplets.* Lab on a Chip, 2006. **6**(8): p. 1073-1079.

106. Takeuchi, S., et al., *An Axisymmetric Flow-Focusing Microfluidic Device.* Advanced Materials, 2005. **17**: p. 1067-1072.

107. Dragosavac, M.M., et al., *Production of Porous Silica Microparticles by Membrane Emulsification.* Langmuir, 2012. **28**(1): p. 134-143.

108. Versteeg, H.K. and W. Malalasekera, *An Introduction to Computational Fluid Dynamics: The Finite Volume Approach*. 1995: Longman Scientific & Technical.

109. Wörner, M., *Numerical modeling of multiphase flows in microfluidics and micro process engineering: a review of methods and applications.* Microfluidics and Nanofluidics, 2012. **12**(6): p. 841-886.

110. H. Ferziger, J. and M. Peric, *Computational Methods for Fluid Dynamics / J.H. Ferziger, M. Peric*. Vol. 3. 2002.

111. Fletcher, C.A., *Computational techniques for fluid dynamics*. 1988: Springer-Verlag. 420.

112. Hirt, C.W. and B.D. Nichols, *Volume of fluid (VOF) method for the dynamics of free boundaries.* Journal of Computational Physics, 1981. **39**(1): p. 201-225.

113. Berberović, E., *Investigation of Free-surface Flow Associated with Drop Impact: Numerical Simulations and Theoretical Modeling.* 2010.

114. Youngs, D.L., *Time-dependent multi-material flow with large fluid distortion.* Numerical Methods for Fluid Dynamics, 1982.

115. Sussman, M. and E.G. Puckett, *A Coupled Level Set and Volume-of-Fluid Method for Computing 3D and Axisymmetric Incompressible Two-Phase Flows.* Journal of Computational Physics, 2000. **162**(2): p. 301-337.

116. Harvie, D.J.E., M.R. Davidson, and M. Rudman, *An analysis of parasitic current generation in Volume of Fluid simulations.* Applied Mathematical Modelling, 2006. **30**(10): p. 1056-1066.

117. Lafaurie, B., et al., *Modelling Merging and Fragmentation in Multiphase Flows with SURFER.* J. Comput. Phys., 1994. **113**(1): p. 134-147.

118. Abadie, T., et al., *Hydrodynamics of gas–liquid Taylor flow in rectangular microchannels.* Microfluidics and Nanofluidics, 2011. **12**.

119. Afkhami, S. and M. Bussmann, *Height functions for applying contact angles to 2D VOF simulations.* International Journal for Numerical Methods in Fluids, 2008. **57**: p. 453-472.

120. Francois, M.M., et al., *A balanced-force algorithm for continuous and sharp interfacial surface tension models within a volume tracking framework.* J. Comput. Phys., 2006. **213**(1): p. 141-173.

121. Hoang, D.A., et al., *Benchmark numerical simulations of segmented two-phase flows in microchannels using the Volume of Fluid method.* Computers & Fluids, 2013. **86**: p. 28-36.

122. Lafaurie, B., et al., *Modelling Merging and Fragmentation in Multiphase Flows with SURFER.* Journal of Computational Physics, 1994. **113**(1): p. 134-147.

123. Abadie, T., et al., *Hydrodynamics of gas-liquid Taylor flow in rectangular microchannels.* Microfluidics and Nanofluidics, 2012. **12**(1-4): p. 355-369.

124. Cummins, S.J., M.M. Francois, and D.B. Kothe, *Estimating curvature from volume fractions.* Comput. Struct., 2005. **83**(6-7): p. 425-434.

125. Osher, S. and J.A. Sethian, *Fronts propagating with curvature-dependent speed: Algorithms based on Hamilton-Jacobi formulations.* Journal of Computational Physics, 1988. **79**(1): p. 12-49.

2

Chapter

PDMS droplet formation and characterization by hydrodynamic flow focusing technique in a PDMS square microchannel*

*J Carneiro1, E Doutel , J B L M Campos and J M Miranda

PDMS droplet formation and characterization by hydrodynamic flow focusing technique in a PDMS square microchannel, **Journal of Micromechanics and Microengineering**, 2016, https://doi.org/10.1088/0960-1317/26/10/105013

2

PDMS droplet formation and characterization by hydrodynamic flow focusing technique in a PDMS square microchannel

Abstract

This study reports the generation of polydimetilsiloxane (PDMS) droplets by hydrodynamic flow focusing technique in a PDMS square microchannel. The droplets generation was characterized, and a flow regime map addressed on the capillary numbers of each phase was assembled. Different flow regimes were found - dripping, jetting, threading and viscous displacement - and the respective boundaries were sketched. Droplet size, breakup distance and formation frequency were analysed and quantified for the jetting and dripping regimes. The dripping regime showed better results for droplets formation, leading to a highest throughput of monodisperse droplets: formation frequency of ≈ 12 Hz and droplets almost uniform in size, 2.8 % the coefficient of variance. The qualitative analysis and quantitative measurement of the different variables and their correlation within a capillary dependent regime map proved to be an invaluable tool to study droplet formation by hydrodynamic flow focusing technique in a PDMS square microchannel.

2.1. Introduction

Microfluidics is a multidisciplinary technology with two decades of existence. Compared to macroscale systems, microfluidics is an invaluable tool for a wide range of areas from engineering to biology, mostly by the capacity of manipulation small volumes of fluid at low Reynolds numbers and by allowing much faster reaction times [1-4]. Among its applications, microfluidics is a leading platform for the generation of droplets and microparticles with tailored sizes and shapes [1-17]. Lab-on-a-chip systems, to generate microscale droplets of one fluid within a second immiscible carrier fluid, are a subclass of microfluidics [3]. Lab-on-a-chip systems offers a promising path to synthetize microparticles, enabling the production of highly uniform particles in the micrometer size range [1-6]. Microparticles, particularly polymeric, are important for a large variety of applications such as drug-delivery, cell mimicking and tissue engineering, among others [1, 10, 18, 19].

Different configurations of microfluidic devices, T– junctions and flow focusing configurations, are used to generate droplets [1, 4, 9]. Microfluidic Flow Focusing Devices (MFFD) have the advantage of parallel generation of droplets and the reutilization of one of the phases [1, 4, 7, 10]. In a MFFD, a carrier phase squeezes a dispersed phase through a common outlet and, by pressure and interfacial instabilities, the dispersed phase breaks down into microdroplets [1, 4, 7, 10].

Microfluidic research devices are generally fabricated in polydimethylsiloxane (PDMS) [1, 4, 9, 10, 20]. The most attractive features of using PDMS as a material to microchannels manufacture is the ability, by soft lithography, to create a large number of devices and the possibility to design complex channel geometries [21]. PDMS is a hydrophobic transparent inert elastomer with unique properties, such as optical clarity, adjustable mechanical properties, gas permeability, and biological compatibility making it a preferred material for many microfluidic based biomedical applications [20, 22, 23].For these reasons, PDMS is a worthy material not only for the MFFD, but also for the polymeric microparticles generation.

Although few, there are some studies concerning the production of PDMS microparticles by flow focusing techniques [17, 24]. However, until now, only one describes the generation of PDMS droplets in a microchannel of the same material

[24]. The generation of PDMS droplets in a PDMS MFFD is very challenging. The high affinity between the PDMS pre-polymer and the channel's wall, coupled with the adhesive nature of the PDMS pre-polymer and the tendency to cure into solid even at room temperature, impose many challenges to the generation of PDMS droplets [20, 23]. In order to avoid contact between the PDMS pre-polymer and the MFFD wall, a previous study used a complex MFFD geometry [24].

Several MFFD are comprised of a simple square section and, consequently, the dimensionless parameters to characterize the droplets generation are well known, i.e. capillary and Webber numbers [25]. Most studies characterize droplet size and droplets generation rate as a function of the continuous and dispersed flow rates [25-28]. Very few correlate these variables with the capillary numbers of both phases [28, 29].

The goals of the present work are the characterization of PDMS droplets formation in a PDMS MFFD and the finding of the best flow conditions to achieve the highest throughput of monodisperse PDMS droplets. The PDMS particles are very attractive, for example, to produce suspensions with ideal optical characteristics to be handled in experiments involving visualization techniques such as Micro Particle Image Velocimetry (μPIV). For the first time a simple square section PDMS MFFD is used to generate droplets of the same material. A flow regime map representing both capillary numbers is created and different flow regimes are observed and characterized through different variables observable during droplets formation. The characterization of the droplets generation by a regime map can provide valuable information about the best flow conditions to achieve a desirable goal and about how to scale-up or scale-down a simple PDMS microfluidic MFFD. This work provides detailed information not only about the regimes that can be found during droplets generation but also a detailed characterization of each map point.

2.2. Experimental

2.2.1. Microfluidic flow-focusing device

The MFFDs were fabricated by soft lithography [30, 31] by pouring a well-mixed solution of PDMS and curing agent (5:1) onto the SU-8 mold. A thin layer, ~ 30 μm,

of PDMS and curing agent (20:1) was spread by spincoating, in a glass slide. This ensures that all the MFFD walls material have the same wetting proprieties. Both, the PDMS mold and the coated glass slide were cured, in an oven, at 80 ºC for 20 minutes. Afterwards, the cured PDMS was peeled off from the SU-8 mold and sealed to the glass coated slide. To ensure a good sealing, the sealed channel was left to cure for approximately 12 hours at 80 ºC [30].

In the droplet formation experiment, the liquid pre-polymer cannot be in direct contact with the PDMS channel walls, since the pre-polymer PDMS has a high affinity with the hydrophobic PDMS of the channel walls, which is undesirable. With an air plasma surface-treatment, the PDMS surface can be modified from hydrophobic to hydrophilic to have more affinity with the aqueous continuous phase. Plasma treatment was carried out with air in a low pressure Plasma Reactor (Diener® electronic GMbH, model ZEPTO).

The MFFD, Figure 2.1, consists of three inlets channels, one for the dispersed phase, two for the continuous phase, and one outlet channel. All these channels intersect at right angles and have identical dimensions.

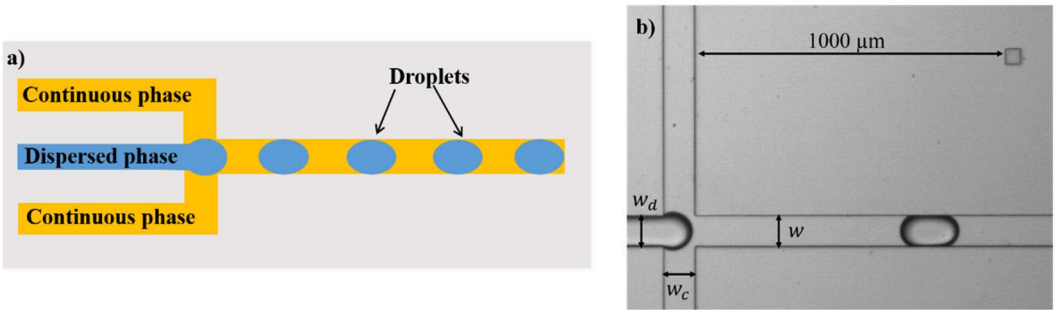

Figure 2.1. a) MFFD illustration and b) MFFD used in this study. w, w_d and w_c are, respectively, the width of the outlet, dispersed and continuous channels ($w = w_d = w_c =$ 100 µm). Marks of 1000 µm long are present along the outlet channel to enable an easy data characterization.

2.2.2. Fluids

The continuous phase was an aqueous solution with a surfactant, Sodium Dodecyl Sulfate (SDS) 2 % (w/w), and the dispersed phase was the liquid pre-polymer PDMS.

The PDMS used for both, channels and dispersed phase, was the Dow Corning Sylgard® 184 kit composed by a base polymer and a curing agent with viscosities, respectively, of 5 and 0.11 Pa s. A base to curing agent ratio of 6:4 was chosen for the PDMS pre-polymer dispersed phase since, in a previous study, droplets were successfully generated taking this proportion [17].

The viscosity of both phases was characterized using a rotational rheometer (Physica MCR301, Anton Paar) with a Peltier temperature control system. The measurements were performed at 20 ºC using a 50 mm diameter plate to plate geometry, PP50, with a gap of 0.1 mm. This gap and the characteristic dimension of the channel are of the same size. As the PDMS pre-polymer cures over time, to avoid drawbacks a 2-hour experimental window for the droplet generation was chosen and the PDMS pre-polymer rheology was characterized during an identical period of time (Figure 2.2).

The viscosities listed in Table 2.1 are the mean viscosities within 2 hours. The density of both phases was measured with a 10 mL pycnometer. The interfacial tension between phases was also measured at ~ 20 ºC in a DuNuoy ring tensiometer. The equilibrium contact angle between the dispersed phase and the channels walls is 42° and was measured according to a previous work by Tan *et al* [32]. The difference between the two wall-fluid interfacial tensions (wall-continuous phase interfacial tension and wall-dispersed phase interfacial tension) is ~ 0.009 N m^{-1}(calculated by the Young´s equation [33]).

Table 2.1. Physical properties of the phases.

Phases	**Viscosity (Pa s)**	**Density (kg m^{-3})**	**Interfacial tension (N m^{-1})**
Continuous	0.001	1001	0.012
Dispersed	0.640	1030	

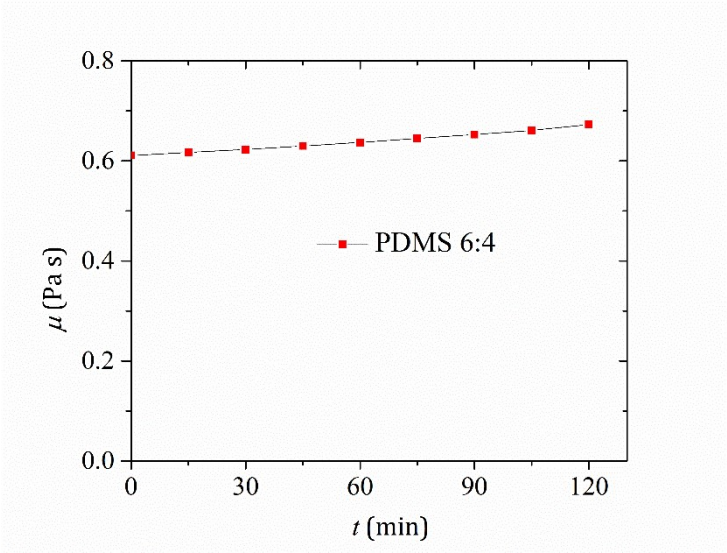

Figure 2.2. Steady-shear viscosity of the PDMS pre-polymer as a function of time at 20 ºC.

2.2.3. Flow visualization and characterization

Droplet formation images were captured at a maximum rate of 10000 frames per second via a high-speed camera (FASTCAM Mini UX100, Photron) mounted on an inverted epifluorescence microscope (DMI 5000M, Leica Microsystems GmbH). Using a dedicated syringe pump, the dispersed and continuous phases were injected into the microchannel. The post-processing of the images was performed using a MATLAB® custom code.

2.3. Results and Discussion

2.3.1. Flow Map

In this study, due to the small size of the device, inertial forces can be neglected and therefore only capillary and viscous forces are responsible for the different flow patterns. The regimes were characterized by the capillary numbers of both phases, defined as:

$$\mathrm{Ca} = \frac{U\mu}{\sigma} \tag{2.1}$$

where U and μ are, respectively, the fluid velocity and dynamic viscosity and σ the interfacial tension.

The flow regime map obtained is presented in Figure 2.3. The identification of the regimes was done according to Cubaud & Mason [25] work and is based only on the cappilary numbers of the phases. Since dripping and jetting regimes are those capable of generating droplets, the characterisation study was narrowed to capillary numbers ranges where these two regimes are reported in the flow regime map and in previous works [25, 26, 29, 34]. Table 2.2 gathers all the experimental conditions including the regime state representing the flow rates imposed, the flow rates ratio:

$$\varphi = \frac{Q_\mathrm{c}}{Q_\mathrm{d}} \tag{2.2}$$

where φ is the flow rates ratio and Q_c and Q_d are the flow rate of the continuous and dispersed phase respectively.

Low capillary numbers for the dripping region (bellow 10^{-2} for the dispersed phase, $\mathrm{Ca_d}$, and 10^{-3} for continuous phase, $\mathrm{Ca_c}$) were also studied to inspect if there is major differences from literature near the jetting regime.

The qualitative identification of the regimes, from Cubaud & Mason [25], is as follows:

- The dripping regime (■), where the thread of the continuous phase breaks and the cap formed stays within the focusing section;
- The jetting regime (■), where the thread breaks and the cap stays in the outlet channel;
- The threading regime (△) , where the thread is stable and doesn't break within a distance of $l < 20\,w$ from the focusing area;
- The viscous displacement regime (◇) characterized by the dispersed phase invading the continuous phase side channels.

Table 2.2. Experimental conditions of both fluids and the respective regimes observed.

φ	Q_d (m s^{-3})	Q_c (m s^{-3})	Ca_d	Ca_c	Regime (symbol)
10	1.67x10^{-12}	1.67x10^{-11}	8.89x10^{-3}	1.39x10^{-4}	■ Dripping
20	1.67x10^{-12}	3.33x10^{-11}	8.89x10^{-3}	2.79x10^{-4}	■ Dripping
30	1.67x10^{-12}	5.00x10^{-11}	8.89x10^{-3}	4.17x10^{-4}	■ Dripping
40	1.67x10^{-12}	6.67x10^{-11}	8.89x10^{-3}	5.56x10^{-4}	■ Dripping
50	1.67x10^{-12}	8.30x10^{-11}	8.89x10^{-3}	6.94x10^{-3}	■ Dripping
20	5.00x10^{-12}	1.00x10^{-10}	2.67x10^{-2}	8.33x10^{-4}	■ Dripping
40	5.00x10^{-12}	2.00x10^{-10}	2.67x10^{-2}	1.67x10^{-3}	■ Dripping
80	5.00x10^{-12}	4.00x10^{-10}	2.67x10^{-2}	3.33x10^{-3}	■ Dripping
166.67	5.00x10^{-12}	5.00x10^{-10}	2.67x10^{-2}	6.94x10^{-3}	■ Dripping
333.33	5.00x10^{-12}	1.67x10^{-9}	2.67x10^{-2}	1.39x10^{-2}	■ Dripping
10	1.00x10^{-11}	1.00x10^{-10}	5.33x10^{-2}	8.33x10^{-4}	■ Dripping
20	1.00x10^{-11}	2.00x10^{-10}	5.33x10^{-2}	1.67x10^{-3}	■ Dripping
30	1.00x10^{-11}	3.00x10^{-10}	5.33x10^{-2}	2.50x10^{-3}	■ Dripping
40	1.00x10^{-11}	4.00x10^{-10}	5.33x10^{-2}	3.33x10^{-3}	■ Dripping
50	1.00x10^{-11}	5.00x10^{-10}	5.33x10^{-2}	4.17x10^{-3}	■ Dripping
6	1.67x10^{-11}	1.00x10^{-10}	8.89x10^{-2}	8.33x10^{-4}	■ Dripping
12	1.67x10^{-11}	2.00x10^{-10}	8.89x10^{-2}	1.67x10^{-3}	■ Jetting
24	1.67x10^{-11}	4.00x10^{-10}	8.89x10^{-2}	3.33x10^{-3}	■ Jetting
50	1.67x10^{-11}	5.00x10^{-10}	8.89x10^{-2}	6.94x10^{-3}	■ Dripping
100	1.67x10^{-11}	1.67x10^{-9}	8.89x10^{-2}	1.39x10^{-2}	■ Dripping
4	2.50x10^{-11}	1.00x10^{-10}	1.33x10^{-1}	8.33x10^{-4}	■ Jetting
8	2.50x10^{-11}	2.00x10^{-10}	1.33x10^{-1}	1.67x10^{-3}	■ Jetting
16	2.50x10^{-11}	4.00x10^{-10}	1.33x10^{-1}	3.33x10^{-3}	■ Jetting
33.3	2.50x10^{-11}	5.00x10^{-10}	1.33x10^{-1}	6.94x10^{-3}	■ Jetting
66.67	2.50x10^{-11}	1.67x10^{-9}	1.33x10^{-1}	1.39x10^{-2}	■ Dripping
2.4	4.17x10^{-11}	1.00x10^{-10}	2.22x10^{-1}	8.33x10^{-4}	△Visc. Displament
4.8	4.17x10^{-11}	2.00x10^{-10}	2.22x10^{-1}	1.67x10^{-3}	■ Jetting
9.6	4.17x10^{-11}	4.00x10^{-10}	2.22x10^{-1}	3.33x10^{-3}	■ Jetting
20	4.17x10^{-11}	5.00x10^{-10}	2.22x10^{-1}	6.94x10^{-3}	■ Jetting
40	4.17x10^{-11}	1.67x10^{-9}	2.22x10^{-1}	1.39x10^{-2}	◇ Threading

In the literature another regime appears before the viscous displacement, the tubing regime, in which continuous phase occupies most of the cross section of the outlet

channel [25]. This regime was not observed, maybe due to the nature of the PDMS pre-polymer and the presence of the surfactant.

In Figure 2.3, at a critical $Ca_d \approx 10^{-1}$ (✸), a transition between the dripping and jetting regimes occurs. This critical value is widely observed in the literature and it depends slightly on Ca_c, [25, 26, 29, 34, 35]. The frontier between these two regimes is important since it signalizes the change between viscous and capillary effects governing the flow [25]. Above the dripping-jetting transition region, the viscous forces dominate and the viscous thread starts to increase in length as both capillary numbers increase and, eventually, the regime becomes purely viscous, (△) [25].

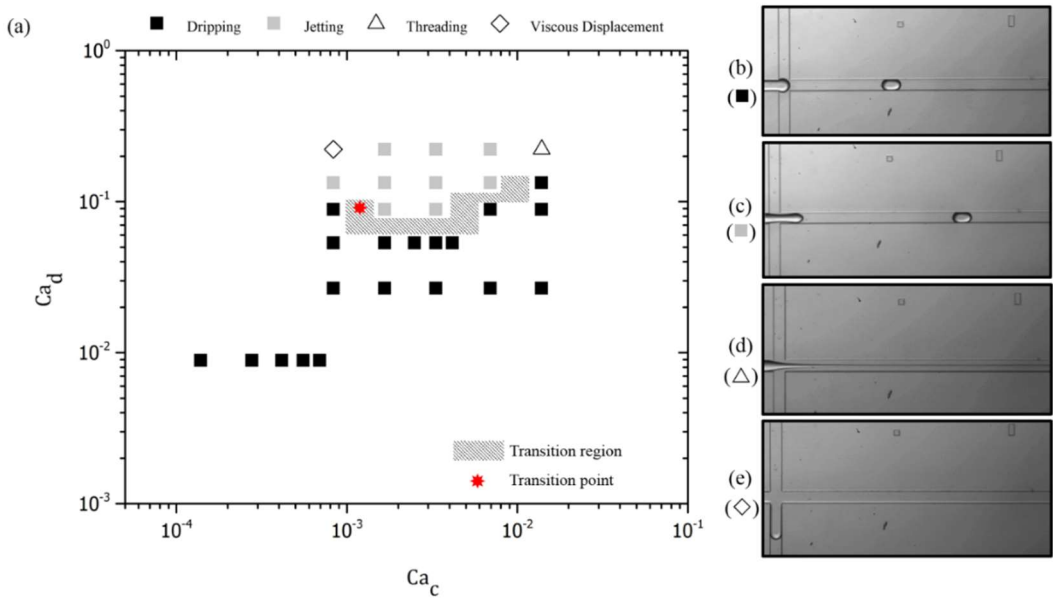

Figure 2.3. (a) Flow map regime of PDMS droplet formation dependent on the capillary numbers and (b) dripping (■), (c) jetting (■), (d) threading (△), (e) viscous displacement (◇).

Since one of the goals of this study (see Introduction) is to find the best flow conditions for monodispersed and high throughput droplet formation, a quantitative characterization of the flows signalized in the regime map is essential. It is worth noting that this quantitative analysis was only done for jetting and dripping regimes.

2.3.2. Frequency

An important parameter to measure the amount of droplets generated over time is the droplet generation frequency, f, given by:

$$f = \frac{nº droplets}{\Delta t} \ (Hz) \tag{2.3}$$

which measures the number of droplets generated over a time interval Δt of 1s. This variable is important to the goals of the present work and a regime with a high frequency value is the most desirable.

According to Figure 2.4 frequency increases until a critical Ca_c number and from there on decreases. The critical Ca_c number is different for each regime, $Ca_c \approx 2\times10^{-3}$ and 3×10^{-3} for the dripping and jetting regime respectively (dashed lines, Figure 2.4). This change is mainly explained by the overlapping of the viscous over the interfacial forces for increasing Ca_c numbers. For very low $Ca_d \approx 1 \times 10^{-2}$ numbers, the frequency is almost independent of Ca_c. As expected, for a given Ca_c number, the frequency increases as the Ca_d number increases.

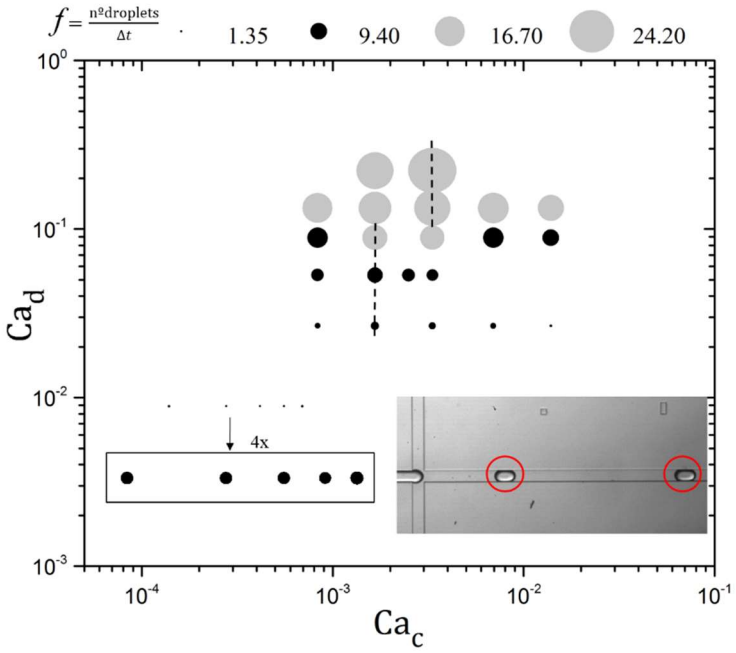

Figure 2.4. Frequency map for the flow regimes. The black and grey symbols correspond to the dripping and jetting regimes, respectively. Dash lines represent changes in the patterns.

2.3.3. Breakup distance

Breakup distance, l, is important to assure that droplets are generated near the focusing area, since instabilities can arise if the threads continue to grow [25]. The normalized breakup distance, L, was measured from the end of the focusing area until the location where the thread breaks up and is given by:

$$\mathrm{L} = \frac{l}{w} \tag{2.4}$$

where w is the characteristic dimension of the channel.

As observed in Figure 2.5, L increases until $Ca_c \approx 3 \times 10^{-3}$ and from there on starts decreasing for both dripping and jetting regime (vertical dashed lines, Figure 2.5). For very low Ca_d 10^{-2}, the normalized breakup distance maintains more or less constant as the Ca_c number increases. For a given Ca_c number, the breakup distance decreases from

the second to the third row of Ca_d number and then starts to increase during the transition from dripping to jetting regime (horizontal dashed lines, Figure 2.5).

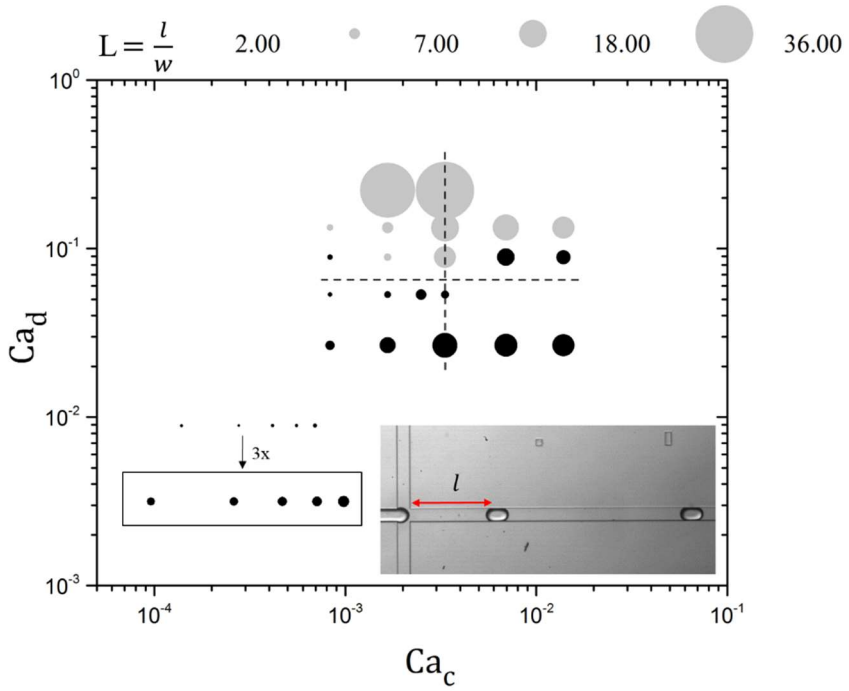

Figure 2.5. Normalized breakup distance according to the capillary numbers of the phases. The black and grey symbols correspond to the dripping and jetting regimes respectively and the dash lines represent changes in the changes in the patterns.

2.3.4. Droplet size

One of the most desirable features in droplet generation is the control of the droplet size. A high throughput monodisperse droplet generation for a large variety of applications [9-11, 29, 35] is an imperative. Normalized droplet size, L_d , is defined by:

$$L_d = \frac{\frac{\sum_{i=1}^{n} l_{di}}{n}}{w} \tag{2.5}$$

where l_{di} is the axial size of droplet i and n the number of measures done for each condition. To have an overall statistical description, it is also important to know the coefficient of variance (CV) of the normalized variable, defined by:

$$\mathrm{CV} = \frac{\sigma_{\mathrm{L_d}}}{\mathrm{L_d}}\, x\, 100 \tag{2.6}$$

where $\sigma_{\mathrm{L_d}}$ is the standard deviation of $\mathrm{L_d}$. As shown in Figure 2.6, normalized droplet size oscillates between 0.90 - 2.20. For both regimes, it is not clear a defined variation pattern with the capillary numbers.

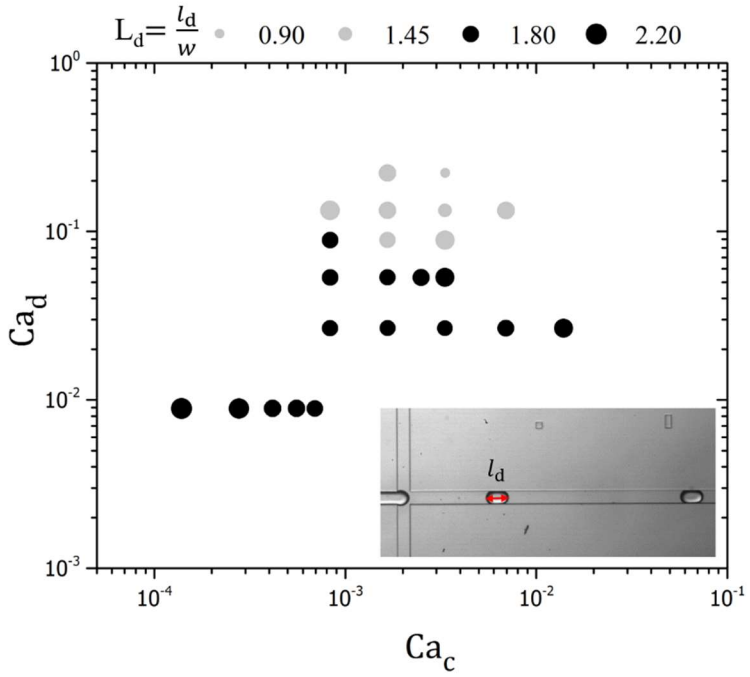

Figure 2.6. Normalized droplet size according to the capillary number of the phases. The black and grey symbols correspond to the dripping and jetting regimes respectively.

Since the droplet size is a mean value, it is important to analyze the coefficient of variance. According to Figure 2.7, the jetting regime presents a very high coefficient of variance, while in the dripping regime the coefficient of variance is around 3.0 % for all the cases measured.

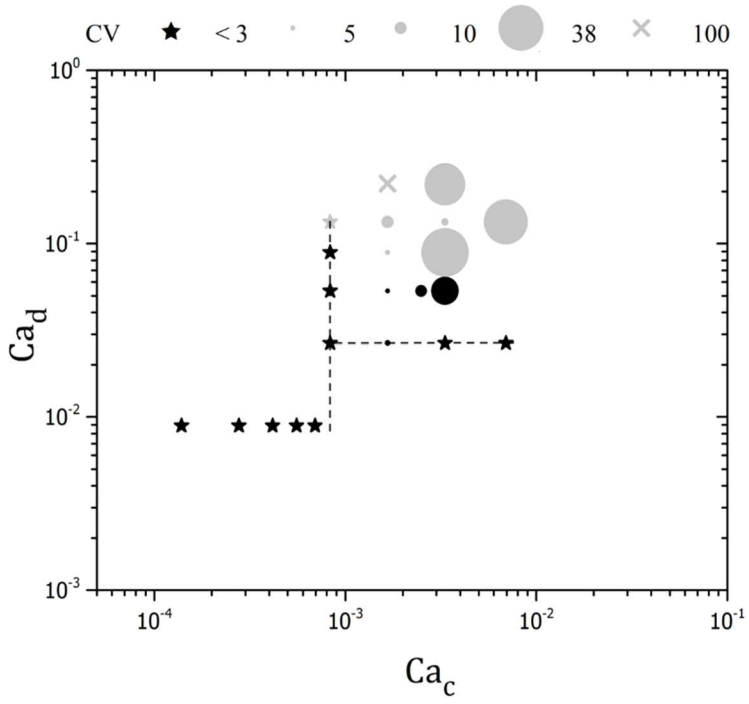

Figure 2.7. Coefficient of variance according to the capillary numbers of the phases. The black and grey symbols correspond to the dripping and jetting regimes respectively and the dash lines represent changes in the patterns.

The main goal of this study was to find out the best flow conditions to obtain high throughput monodisperse PDMS droplets in a PDMS MFFD. The experimental data obtained proved to be possible to attain the proposed goal with the experimental technique developed. By analyzing the different variables, the optimal conditions to obtain high throughput monodisperse PDMS droplets are in the dripping regime, near the critical Ca number, where the best compromise between a low size coefficient variance, 2.8 %, and a high formation frequency ≈ 12 Hz, is achieved. This frequency number is only valid for the operating scale of this work.

2.4. Conclusions

In this study, PDMS droplet generation in square section channels of the same material is presented and characterized. A flow map regime was constructed and different regimes were identified: jetting, dripping, threading and viscous

displacement regime. The jetting and dripping regimes were highlighted since they are the only ones capable of producing droplets. The characterization of the regimes allowed to point the best regions to create stable and monodisperse droplets enabling the control of the formation frequency and the breakup distance. A critical Ca number was found to limit the stable dripping regime from the unstable jetting regime, which is in good agreement with previous studies [25, 26, 29, 34]. This critical point not only delimits the two regimes but also restricts from which Ca numbers is possible to control the droplet generation. From the results, the dripping regime presented a lower size coefficient variance (around 2.8 %) compared to the jetting regime. The highest stable formation frequency (≈ 12 Hz) is achieved in the dripping regime located near the critical Ca number.

PDMS is a widely used polymer in microfluidic systems and this study proved to be a valuable tool to create PDMS droplets in a PDMS simple microfluidic flow focusing system.

Acknowledgments

This work was funded by FEDER funds through the Operational Program for Competitiveness Factors – COMPETE, ON.2 - O Novo Norte - North Portugal Regional Operational Program and National Funds through FCT - Foundation for Science and Technology under the projects: PEst-OE/EME/UI0532, FCT/3013/10/2/2016/S, PTDC/QEQ-FTT/4287/2014 and NORTE-07-0124-FEDER-000025- RL2_ Environment&Health.

Notation

Latin	Definition	Units
CV	Coefficient of variance	(%)
f	Droplet generation frequency	(Hz)
l	Breakup distance	(m)
L	Normalized breakup distance	---
l_{d}	Droplet length	(m)
$\mathrm{L_d}$	Normalized droplet length	---
Q	Volumetric flow rate	($m^3\ s^{-1}$)
Q_{c}	Volumetric flow rate of the continuous phase	($m^3\ s^{-1}$)
Q_{d}	Volumetric flow rate of the dispersed phase	($m^3\ s^{-1}$)
U	Velocity	($m\ s^{-1}$)
w	Outlet channel width	(m)
w_{c}	Continuous phase channel width	(m)
w_{d}	Dispersed phase channel width	(m)

Greek	Definition	Units
Δt	Time interval	(s)
μ	Dynamic viscosity	(Pa s)
σ	Interfacial tension	($N\ m^{-1}$)
$\sigma_{\mathrm{L_d}}$	Standard deviation of the normalized droplet length	---
φ	Volumetric flow rates ratio	---

Dimensionless numbers	Definition
Ca	Capillary number
Ca	Capillary number
Ca_c	Capillary number of the continuous phase
Ca_d	Capillary number of the dispersed phase

Acronyms	Definition
MFFD	Microfluidic flow focusing device
PDMS	Polydimethylsiloxane
SDS	Sodium dodecyl sulphate
SU-8	Designation of epoxi-bored photoresist
μPIV	Micro particle image velocimetry

References

1. Teh, S.-Y., et al., *Droplet microfluidics.* Lab on a Chip, 2008. **8**(2): p. 198-220.
2. Dendukuri, D., et al., *Continuous-flow lithography for high-throughput microparticle synthesis.* Nat Mater, 2006. **5**(5): p. 365-369.
3. Xu, S., et al., *Generation of monodisperse particles by using microfluidics: control over size, shape, and composition.* Angew Chem Int Ed Engl, 2005. **44**(5): p. 724-8.
4. Baroud, C.N., F. Gallaire, and R. Dangla, *Dynamics of microfluidic droplets.* Lab on a Chip, 2010. **10**(16): p. 2032-2045.
5. Peng Lee, C., Y. Hsin Chen, and Z. Hang Wei, *Fabrication of hexagonally packed cell culture substrates using droplet formation in a T-shaped microfluidic junction.* Biomicrofluidics, 2013. **7**(1): p. 14101.
6. Utada, A.S., et al., *Dripping to Jetting Transitions in Coflowing Liquid Streams.* Physical Review Letters, 2007. **99**(9): p. 094502.
7. Anna, S.L., N. Bontoux, and H.A. Stone, *Formation of dispersions using "flow focusing" in microchannels.* Applied Physics Letters, 2003. **82**(3): p. 364-366.
8. Dufaud, O., E. Favre, and V. Sadtler, *Porous elastomeric beads from crosslinked emulsions.* Journal of Applied Polymer Science, 2002. **83**(5): p. 967-971.
9. Dendukuri, D. and P.S. Doyle, *The Synthesis and Assembly of Polymeric Microparticles Using Microfluidics.* Advanced Materials, 2009. **21**(41): p. 4071-4086.
10. Todd, P.L. and F.E. Jon, *A review of the theory, methods and recent applications of high-throughput single-cell droplet microfluidics.* Journal of Physics D: Applied Physics, 2013. **46**(11): p. 114005.
11. Garstecki, P., H.A. Stone, and G.M. Whitesides, *Mechanism for Flow-Rate Controlled Breakup in Confined Geometries: A Route to Monodisperse Emulsions.* Physical Review Letters, 2005. **94**(16): p. 164501.
12. Christian, H., *Large-scale droplet production in microfluidic devices—an industrial perspective.* Journal of Physics D: Applied Physics, 2013. **46**(11): p. 114008.
13. Garstecki, P., et al., *Formation of droplets and bubbles in a microfluidic T-junction-scaling and mechanism of break-up.* Lab on a Chip, 2006. **6**(3): p. 437-446.
14. Nie, Z., et al., *Emulsification in a microfluidic flow-focusing device: effect of the viscosities of the liquids.* Microfluidics and Nanofluidics, 2008. **5**(5): p. 585-594.

15. Tran, T.M., S. Cater, and A.R. Abate, *Coaxial flow focusing in poly(dimethylsiloxane) microfluidic devices.* Biomicrofluidics, 2014. **8**(1): p. 016502.

16. Takeuchi, S., et al., *An Axisymmetric Flow-Focusing Microfluidic Device.* Advanced Materials, 2005. **17**(8): p. 1067-1072.

17. Jiang, K., et al., *Microfluidic synthesis of monodisperse PDMS microbeads as discrete oxygen sensors.* Soft Matter, 2012. **8**(4): p. 923-926.

18. Champion, J.A., Y.K. Katare, and S. Mitragotri, *Particle Shape: A New Design Parameter for Micro- and Nanoscale Drug Delivery Carriers.* Journal of controlled release : official journal of the Controlled Release Society, 2007. **121**(0): p. 3-9.

19. Xu, Q., et al., *Preparation of Monodisperse Biodegradable Polymer Microparticles Using a Microfluidic Flow-Focusing Device for Controlled Drug Delivery.* Small, 2009. **5**(13): p. 1575-1581.

20. Mata, A., A. Fleischman, and S. Roy, *Characterization of Polydimethylsiloxane (PDMS) Properties for Biomedical Micro/Nanosystems.* Biomedical Microdevices, 2005. **7**(4): p. 281-293.

21. Shah, R.K., et al., *Designer emulsions using microfluidics.* Materials Today, 2008. **11**(4): p. 18-27.

22. Friend, J. and L. Yeo, *Fabrication of microfluidic devices using polydimethylsiloxane.* Biomicrofluidics, 2010. **4**(2): p. 026502.

23. Friend, J. and L. Yeo, *Fabrication of microfluidic devices using polydimethylsiloxane.* Biomicrofluidics, 2010. **4**(2): p. -.

24. Di Benedetto, F., et al., *Rolling particle lithography by soft polymer microparticles.* Soft Matter, 2013. **9**(7): p. 2206-2211.

25. Cubaud, T. and T.G. Mason, *Capillary threads and viscous droplets in square microchannels.* Physics of Fluids, 2008. **20**(5): p. 053302.

26. Nunes, J.K., et al., *Dripping and jetting in microfluidic multiphase flows applied to particle and fiber synthesis.* Journal of physics D: Applied physics, 2013. **46**(11): p. 114002.

27. Ward, T., et al., *Microfluidic flow focusing: Drop size and scaling in pressure versus flow-rate-driven pumping.* ELECTROPHORESIS, 2005. **26**(19): p. 3716-3724.

28. Lee, W., L.M. Walker, and S.L. Anna, *Role of geometry and fluid properties in droplet and thread formation processes in planar flow focusing.* Physics of Fluids (1994-present), 2009. **21**(3): p. 032103.

29. Rosenfeld, L., et al., *Review and analysis of performance metrics of droplet microfluidics systems.* Microfluidics and Nanofluidics, 2014. **16**(5): p. 921-939.

30. Sousa, P.C.S., *Entry flow of viscoelastic fluids at macro- and micro-scale*. 2010, University of Porto

31. Xia, Y.N. and G.M. Whitesides, *Soft lithography.* Annual Review of Materials Science, 1998. **28**: p. 153-184.

32. Tan, S.H., et al., *Oxygen plasma treatment for reducing hydrophobicity of a sealed polydimethylsiloxane microchannel.* Biomicrofluidics, 2010. **4**(3): p. 032204.

33. Yuan, Y. and T.R. Lee, *Contact Angle and Wetting Properties*, in *Surface Science Techniques*, G. Bracco and B. Holst, Editors. 2013, Springer Berlin Heidelberg: Berlin, Heidelberg. p. 3-34.

34. Anna, S.L., *Droplets and Bubbles in Microfluidic Devices.* Annual Review of Fluid Mechanics, 2016. **48**(1): p. null.

35. Stone, H.A., *Dynamics of Drop Deformation and Breakup in Viscous Fluids.* Annual Review of Fluid Mechanics, 1994. **26**(1): p. 65-102.

3

Chapter

High viscosity polymeric fluid droplet formation in a flow focusing microfluidic device - experimental and numerical study*

*J.Carneiro, JBLM. Campos, JM. Miranda
High viscosity polymeric fluid droplet formation in a flow focusing microfluidic device - experimental and numerical study, **Chemical Engineering Science**, https://doi.org/10.1016/j.ces.2018.09.042.

3

High viscosity polymeric fluid droplet formation in a flow focusing microfluidic device - experimental and numerical study

Abstract

Experimental and numerical studies concerning the formation of droplets of a viscous fluid in a less viscous immiscible one (viscosity ratio of 533), containing surfactant, were conducted in a flow-focusing square microchannel. Numerical and experimental data from three flow regimes were analysed: threading, dripping and jetting. The results were analysed qualitatively and quantitatively and also compared to correlations from the literature. The droplet sizes and the thread lengths obtained experimentally deviate from the ones obtained for surfactant free systems reported in the literature. The roles of the surfactant mass transport limitations and of the interface rheology are analysed and discussed. The numerical code, based on a coupled level-set and volume of fluid method, successfully predicts droplets sizes in surfactant free systems in almost all the conditions studied. The limits of the numerical code to accurately predict the size of the droplets, particularly in the monodispersed dripping

regime, were established. If surfactant is present, the numerical code fails to predict the droplet size under certain flow conditions.

3.1 Introduction

Polymeric microparticles are important for a large variety of applications such as drug-delivery, cell mimicking and tissue engineering, among others [1-7]. Droplet-based microfluidics are able to generate highly uniform droplets in the micrometer and nanometer size ranges [4, 8-11].

Different configurations of microfluidic devices, T-junctions, co-flowing and flow focusing configurations, are used to generate [12-14]. Microfluidic Flow Focusing Devices (MFFD), when compared with other configurations, have the advantage of parallel generation of droplets at higher frequencies [1, 9, 10, 15, 16]. In a MFFD, a carrier phase (continuous phase) squeezes a dispersed phase through a common outlet and, promoted by fluid instabilities, the dispersed phase breaks down into droplets, Figure 3.1. Droplets formation in MFFD can happen in two regimes: jetting and dripping [9, 17].

The qualitative identification of these flow regimes, Figure 3.1, is as follows:

- The dripping regime, where the thread of the dispersed phase breaks, retracts, and the drop is formed near the focusing section - Figure 3.1a. Although most of the dripping regime produces monodispersed droplets, it can also produce polydispersed at high Capillary numbers [18];
- The jetting regime, defined through persistent thread generating small droplets - Figure 3.1b;
- When the thread is stable and doesn't break within a distance $l < 20\ h$ from the focusing section, the flow is under the threading regime - Figure 3.1c;
- When the flow rate of the more viscous dispersed phase is much higher than that of the continuous phase, the dispersed phase invades the side channels leading to viscous displacement - Figure 3.1d.

MFFD are generally fabricated in polydimethylsiloxane (PDMS) [18-20]. PDMS is a hydrophobic transparent inert elastomer suitable not only for the channels material but

also for the microdroplets. The generation of PDMS droplets in a PDMS MFFD is very challenging owing the affinity between droplets and PDMS channel walls [18, 21]. Since PDMS can be cured by simply applying heat, PDMS cured particles can be further used as sensors [22] for microlithography [21] or to produce biomimetic fluids [23].

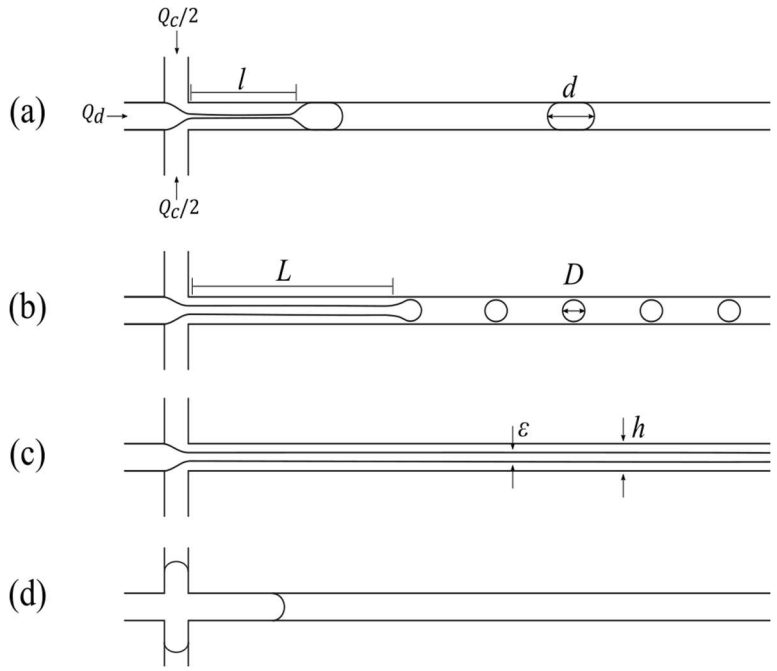

Figure 3.1. Schematic representation of the different flow regimes in a simple flow-focusing geometry: (a) dripping; (b) jetting ;(c) threading and (d) viscous displacement. Variables l and L are the thread length of the dripping and jetting regimes respectively, ε the thread diameter, d and D the droplet axial length and the droplet diameter, respectively.

In a square section MFFD, the normalized size of the droplets depends mainly on three dimensionless parameters: the flow rates ratio, $\varphi = Q_\mathrm{d}/Q_\mathrm{c}$, the viscosities ratio, $\chi = \mu_\mathrm{d}/\mu_\mathrm{c}$, and the capillary number of the dispersed phase, $\mathrm{Ca_d} = \mu_\mathrm{d} U_\mathrm{d}/\sigma$ (Q is the volumetric flow rate, μ the dynamic viscosity, U the average velocity at the inlet and σ the interfacial tension, while the subscripts d and c refer to the dispersed and continuous phases, respectively). Other dimensionless parameters such as Reynolds number, $\mathrm{Re} = \rho U h/\mu$ (ρ is the density of the fluid), and Weber number, $\mathrm{We} = \rho h U^2/\sigma$ are also important when the channel dimensions and/or U are sufficiently large for inertia to dominate viscous and surface tension forces. On our work $\mathrm{Re_d} \ll 1$ and $\mathrm{We_d} \ll 1$ and therefore inertia is not relevant.

Polymeric dispersed phase viscosity can be up to three orders of magnitude higher than the continuous phase viscosity [18, 24, 25]. Monodispersed particles are mostly generated in the dripping regime, in which the size of the droplets formed is weakly dependent on the flow rates ratio [26].

Several empirical correlations for predicting different variables such as the droplet size, thread and droplet diameters in flow-focusing configurations can be found in the literature [9, 17, 27-39]. The most relevant, for the development of this work, are the Cubaud and Mason [17] empirical correlations (Table 3.1), since they cover a wide range of high viscosity ratios, $\chi \in [22, 1500]$, and different flow regimes (threading, dripping and jetting).

Table 3.1. Cubaud and Mason[17] empirical correlations for different parameters and flow conditions for threading, dripping and jetting regimes, $24 \leq \chi \leq 1448$.

Regime	Normalized parameter	Scaling law(s)	Flow conditions
Threading	Thread diameter	$\varepsilon/h \approx \left(\frac{1}{2}\varphi\right)^{1/2}$	$\mathrm{Ca_d} \gg 10^{-1}$
Dripping	Droplet length	$d/h = 2.2 \times 10^{-4}\ (\alpha_c \mathrm{Ca_c})^{-1}\ (d > 2.5h)$	$\mathrm{Ca_d} < 10^{-1}$ $\mathrm{Ca_c} < 10^{-1}$
		$d/h = 0.5\ (\alpha_c \mathrm{Ca_c})^{-0.17}\ (d < 2.5h)$	
	Thread length	$l/h = \mathrm{C_t} \frac{\mu_d}{\sigma \mathrm{Ca_{cri}}} \frac{Q_d + Q_c}{2h^2}$	
Jetting	Droplet diameter	$D/h \approx 3.1 \left(\frac{1}{2}\varphi\right)^{1/2}$	$\mathrm{Ca_d} \sim \mathrm{Ca_{cri}} > 10^{-1}$
	Thread length	$L/h = \frac{\mathrm{C_j} \frac{\mu_d}{\sigma} \frac{8}{\pi h \mathrm{Ca_{cri}}} \left(\frac{Q_d Q_c}{2}\right)^{1/2}}{h}$	

Note: $\mathrm{C_t}$ and $\mathrm{C_j}$ are dimensionless constants close to unit, 2.1 and 1 respectively, $\mathrm{Ca_{cri}}$ is a critical capillary number that delimits the transition between dripping and jetting regimes and $\alpha_c = Q_c/(Q_c + Q_d)$ is the continuous phase flow ratio.

Since the establishment of empirical correlations involves large range of experimental conditions, numerical methods can be an invaluable tool to understand and predict the flow regimes and quantify the operation variables in droplet microfluidics. Most of the numerical studies about droplet formation in MFFD found in the literature are for $\chi \leq 100$ [40].

In this work, experiments in a MFFD are conducted with the two phases system water + SDS / PDMS (viscosity ratio of 533) in order to cover threading, dripping and jetting regimes. Experimental and numerical data are compared with Cubaud and Mason [17] empirical correlations. Special focus is on the dripping regime for high viscosity ratios, since it produces monodispersed particles in a wide range of operating conditions with a coefficient of variance of 3 % or less [18]. The role of the surfactant is analyzed by comparing results obtained with two different surfactant concentrations and with Cubaud and Mason [17] correlations, which were obtained in experiments without surfactant. A numerical code, based on a coupled level-set and volume of fluid (CLSVOF) method, is used to predict droplet size and thread length and the results are compared with the experimental results and with Cubaud and Mason [17] correlations.

3.2 Methods

3.2.1 Experimental techniques and procedure

The MFFD consists of three inlet channels — one for the dispersed phase, two for the continuous phase — and one outlet channel. All these channels intersect at right angles and have identical width and depth (Figure 3.1), 100 μm.

SU-8 molds of the MFFD were purchased to an external supplier. The MFFDs were fabricated by soft lithography [18] by a 5:1 PDMS and curing agent for the channel and a 20:1 base and curing thin layer, ~ 30 μm, of PDMS for the glass slide (Dow Corning Sylgard® 184 kit). This ensures that all the MFFD walls material have the same wetting proprieties. Both, PDMS mold and coated glass slide were cured, in an oven, at 80 ºC for 20 minutes. Afterwards, the cured PDMS was sealed to the glass coated slide and left to cure for approximately 12 hours at 80ºC [18]. Air plasma surface-treatment was applied to the PDMS surface in a low pressure Plasma Reactor (Diener® electronic GMbH, model ZEPTO) to render the surface hydrophilic.

Water with a surfactant, Sodium Dodecyl Sulfate (SDS) 2% w/w, was chosen for the continuous phase ($\mu_c = 0.0012$ Pa s and $\rho_c = 1001$ kg m^{-3}). Additionally, water with a surfactant SDS 8% w/w ($\mu_c = 0.0019$ Pa s and $\rho_c = 1014$ kg m^{-3}) was used for the continuous phase in experiments aiming to check for effects of mass transport

limitations of the surfactant. The dispersed phase was PDMS pre-polymer with a ratio of 6:4 base and curing agent respectively (Corning Sylgard® 184 kit). Although both, dispersed and continuous phases, are Newtonian fluids, the dispersed phase is a polymer that slowly cures at room temperature (~ 20-25 ºC). To avoid viscosity changes during the experiments, these were limited to a 2 hours period after the addition of the curing agent to the base. With all these conditions considered, the viscosity and density of the polymeric dispersed phase within the experimental period were $\mu_d = 0.640$ Pa s and $\rho_d = 1030$ kg m^{-3} respectively. The viscosity of both phases was characterized using a rotational rheometer (Physica MCR301, Anton Paar) with a Peltier temperature control system set at 20 ºC. The interfacial tension was measured at ~ 20 ºC in a DuNuoy ring tensiometer.

Droplet formation images were captured via a high-speed camera (FASTCAM Mini UX100, Photron), at a maximum rate of 10000 frames per second, mounted on an inverted epifluorescence microscope (DMI 5000M, Leica Microsystems GmbH). Using a dedicated syringe pump, the dispersed and continuous phases were injected into the microchannel, Figure 3.2. The post-processing of the images was performed using a MATLAB® custom code.

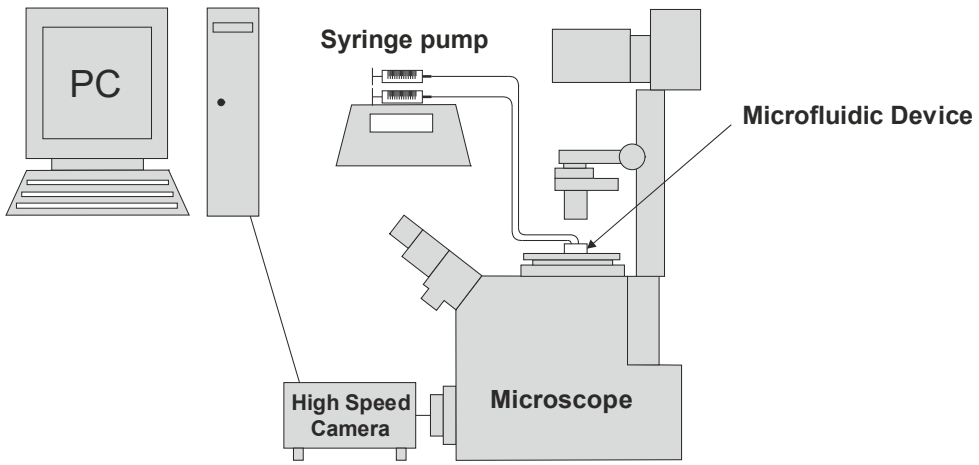

Figure 3.2. Experimental setup and microchannel flow focusing channel.

3.2.2 Numerical methods

Several numerical interface-capturing methods have been applied in recent studies of droplet formation in flow-focusing geometries: volume of fluid (VOF) method [41], level-set (LS) method [40], Lattice-Boltzmann method [42] and phase field method [39]. Other methods such as interface-tracking methods [43, 44] are also valuable in multiphase flow simulations; however they can be computationally demanding. These tracking methods are, in recent works, combined with neural networks statistical learning methods [17, 45, 46]. In a very simple description, in interface-tracking methods the mesh is an integral part of the interface and needs to be restructured as the flow progresses, whereas in interface-capturing methods the interface does not lay on the mesh elements but rather through them, being updated within the mesh elements [47]. The VOF method is the most widely applied interface-capturing method in modeling multiphase flows in microfluidic channels, due to its efficient tracking of the topological changes of the fluids interface. Although VOF is a robust method, for this work, we chose a coupled LS and VOF method (CLSVOF) [48]. The VOF method applies a discontinuous step function [49] and therefore it is sometimes difficult to obtain the accurate curvature and smooth physical properties at the interface. In contrast, the LS method applies a continuous smother function to track the interface, but has the disadvantage of lose mass during the numerical procedure [50]. In order to overcome both deficiencies, the CLSVOF method was chosen and is currently available in ANSYS FLUENT software (since Release 13.0, ANSYS Inc., USA).

Both liquid phases were considered Newtonian incompressible fluids and the Navier-Stokes equations are then given by:

$$\frac{\partial(\rho\vec{v})}{\partial t} + \nabla\cdot(\rho\vec{v}\vec{v}) = -\nabla p + \nabla\cdot[\mu(\nabla\vec{v} + \nabla\vec{v}^{T})] + \overrightarrow{f_{\sigma}} \tag{3.1}$$

$$\nabla\cdot\vec{v} = 0 \tag{3.2}$$

where p is the pressure, $\vec{v}$ the velocity vector , μ the dynamic viscosity of the fluid and $\overrightarrow{f_{\sigma}}$ represents the surface tension force term.

The CLSVOF comprises both advective VOF and LS equations (Eqs. (*3.3*) and (*3.6*) respectively). Mass conservation is guaranteed by the advective VOF equation and the interface sharpness by calculating the normal to the interface using the smoothed function ϕ (Eq. (*3.5*)). The size of the cut in the cell where the interface passes through is provided by VOF method, while the gradient of the level-set function determines the direction of the interface (LS method). The surface tension force is calculated by Eq.(*3.10*).

The advective equation in its conservative form can be written as:

$$\frac{\partial \alpha}{\partial t} + \nabla \cdot (\alpha \vec{v}) = 0 \tag{3.3}$$

where the volume fraction α at a given point, with a vector position $\vec{x}$, is defined as follows:

$$\alpha(\vec{x}, t) = \begin{cases} 0 & \alpha < 1 \ continuous \ phase \\ 0 < \alpha < 1 & \alpha = 0 \text{ interface} \\ 1 & \alpha > 1 \ dispersed \ phase \end{cases} \tag{3.4}$$

By its turn, the level-set function, ϕ, is the signed distance to the interface:

$$(\vec{x}, t) = \begin{cases} +d & if \ \vec{x} \ \epsilon \ dispersed \ phase \\ 0 & if \ \vec{x} \ \epsilon \ interface \\ -d & if \ \vec{x} \ \epsilon \ continuous \ phase \end{cases} \tag{3.5}$$

where d is the distance from a point to the interface. For each time step, the LS function is re-initialized, and the interface is determined by solving the LS advective equation:

$$\frac{\partial \phi}{\partial t} + \vec{v} \cdot \nabla \phi = 0 \tag{3.6}$$

The surface tension is calculated by the continuum surface force model (CSF) [51]:

$$\overrightarrow{f_\sigma} = \sigma \kappa \delta(\phi) \vec{n} \tag{3.7}$$

where $\delta(\phi)$ is a smooth Dirac function centered in the interface.

The unit normal vector $\vec{n}$ and the local mean interface curvature κ are defined as:

$$\vec{n} = \frac{\nabla\phi}{|\nabla\phi|}\Big|_{\phi=0} \tag{3.8}$$

$$\kappa = \nabla \cdot \frac{\nabla\phi}{|\nabla\phi|}\Big|_{\phi=0} \tag{3.9}$$

In some cases, applying the CSF model, Eq. (*3.7*), unphysical spurious currents can appear at the interface [52], particularly at $\mathrm{Ca} < 0.01$ [52, 53], Figure 3.3. To mitigate these effects, a weighting function was used on the surface tension term:

$$\overrightarrow{f_\sigma} = 2H_\phi \sigma\kappa\delta(\phi)\vec{n} \tag{3.10}$$

where H_ϕ :

$$H_\phi = \begin{cases} 0 & |\phi| > \epsilon \text{ (dispersed phase)} \\ 1 & |\phi| > \epsilon \text{ (continuous phase)} \\ \frac{1}{2}\left[1 + \frac{\phi}{\epsilon} + \frac{1}{\pi} sin\left(\frac{\pi\phi}{\epsilon}\right)\right] & |\phi| \leq \epsilon \end{cases} \tag{3.11}$$

where ϵ is the thickness of the interface.

In Figure 3.3, the spurious currents near the interface are shown, when VOF and CLSVOF methods are used. Contrarily, using the CLSVOF method with the H_ϕ scaling, at the droplet interface do not appear spurious currents and the interface has the most similar shape to the one obtained experimentally. The main disadvantage of using the CLSVOF with the weighting function, H_ϕ, is the need of a uniform mesh, otherwise when local refinement or grading is applied, the interface appears distorted in the refined regions. The need of a uniform mesh has computational costs. Local refinement is usually applied to improve the quality of the mesh in the film region, between the droplets and the wall. This film region is important to quantify mass transport rates in both circular and non-circular channels [54-56].

Boundary Conditions

The domain and mesh used are shown in Figure 3.4. The mesh was generated using Meshing from Ansys workbench software (ANSYS Inc.).

A uniform inlet velocity was set at the two inlets and a null relative pressure was set at the outlet. A no-slip boundary condition was used at the walls.

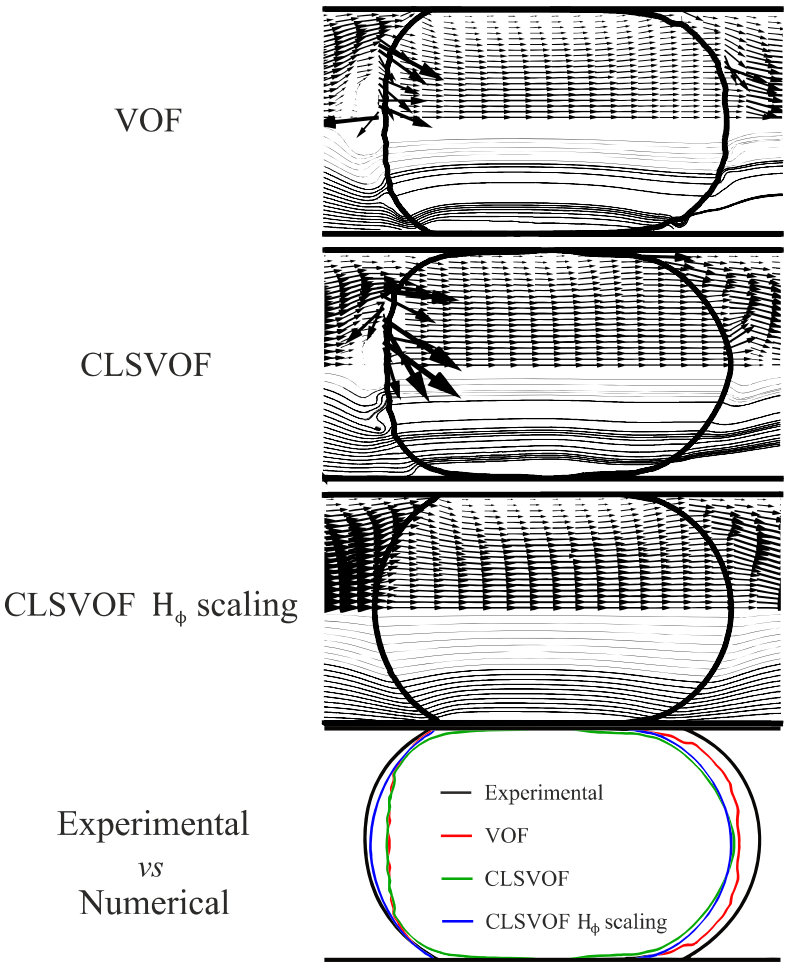

Figure 3.3. Experimental and numerical data comparison for $\chi = 533$, $Q_d = 0.6$ and $Q_c = 6$ (μL min^{-1}). Numerical data obtained through different methods: VOF, CLSVOF and CLSVOF H_ϕ scaling. Mesh resolution: $x/h = 0.02$. XY midplane is shown.

For the pressure interpolations "PRESTO!" scheme (PREssure STaggering Option) was used while PISO algorithm (Pressure-Implicit with Splitting Operators) was to

solve pressure-velocity coupling. The QUICK differencing scheme was employed to solve the momentum and level-set equations. The scalar gradients were computed by the Green-Gauss node-based method. The geometric reconstruction scheme (the Piecewise Linear Interpolation Calculation, PLIC) was used for the interface reconstruction.

The simulations were carried out on a cluster (16 cores and 32 GB RAM). The typical simulation time for the x=4 μm and x=4μm meshes (see section below) with 108,000 and 980,000 elements was about 4 days and 20 days respectively in order to generate at least two consecutive droplets. The time step was adjusted to a Courant number of 0.25 with a maximum time step of 1^{-5} s.

The physical properties of the fluids tested numerically are listed in Table 3.2. A fully non-wetting boundary condition (static contact angle of 180º) was chosen. Non-wetting conditions are preferred over dynamic contact angles, since the latter are very difficult to solve numerically [55]. To avoid dispersed phases with affinity to the channels wall, pairs of fluids, from Cubaud and Mason [17] work, with a high interfacial tension were chosen, G3 pairs (Table 3.2). For low interfacial fluid pairs, $\sigma \leq 2.2$ mN m^{-1}, Cubaud and Mason [17] observed a partially wetting of the wall by the dispersed phase, phenomena undesirable for steady generation of droplets [17, 57].

The inlet lengths are three times the characteristic dimension of the channels to ensure fully developed flows for all operating conditions.

Mesh Tests

For a given set of viscosity ratios, $24 \leq \chi \leq 1480$, different simulations were carried out by varying the mesh size elements (8, 4 and 2 μm). The chosen variable to analyze the mesh independency was the droplet size in the dripping regime d/h. It was observed that mesh independent solutions were obtained for mesh size of x=4 μm for $439 \leq \chi$ and a finer grid, x=2 μm, for $\chi \geq 439$, Table 3.3.

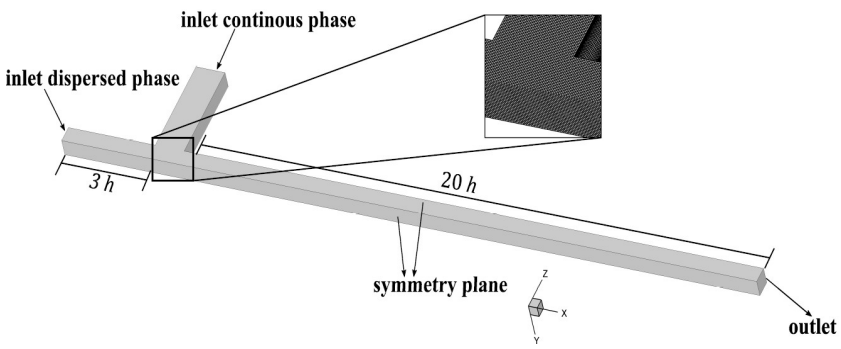

Figure 3.4. Geometry, boundaries and mesh representation (finer mesh, $x/h = 0.02$) of the MFFD numerical domain. The width in z direction is $0.5h$.

Table 3.2. Fluids and their respective relevant properties chosen from Cubaud and Mason [17] and our experimental fluid pairs.

Fluids pair(s)	Fluid properties					
	Dispersed phase	Viscosity (μ_d) [Pa·s]	Continuous phase	Viscosity (μ_c) [Pa·s]	Interfacial tension (σ) [mN·m^{-1}]	Viscosity ratio (χ)
G3C	Glycerol 100%	1.214	PDMS Oil 2	0.05	27	24
G3E	Glycerol 80%	0.077	PDMS Oil 3	0.00082	30.4	94
G3B	Glycerol 100%	1.214	PDMS Oil 1	0.00459	27	264
G3D	Glycerol 92%	0.36	PDMS Oil	0.00082	28.2	439
G3A	Glycerol 100%	1.214	PDMS Oil	0.00082	26.6	1480
Experimental 2% SDS	PDMS 6:4	0.640	Water 2% SDS	0.0012	12	533
Experimental 8% SDS	PDMS 6:4	0.640	Water 8% SDS	0.0019	12	337

Table 3.3. Numerical mesh grid independence test.

Fluids pair(s)	Ca_d	Ca_c	χ	Result(s) (d/h)				
				Scaling law *	Exp. 2% SDS	Numerical		
						Grid resolution (x/h)		
						0.08	0.04	0.02
G3C	2.25×10^{-2}	1.23×10^{-2}	24	1.07	1.16	0.96	0.99	1.02
G3E	2.11×10^{-2}	4.50×10^{-3}	94	1.26	-	1.07	1.06	1.10
G3E	2.25×10^{-2}	1.70×10^{-3}	264	1.49	-	1.30	1.22	1.23
G2D	2.13×10^{-2}	9.69×10^{-4}	439	1.64	-	1.34	1.33	1.34
G3A	2.28×10^{-2}	3.08×10^{-4}	1480	1.99	-	1.35	1.65	1.90
Exp.	5.33×10^{-2}	1.00×10^{-3}	533	1.64	1.71	1.48	1.48	1.57

* Cubaud and Mason (2008)

3.3 Results and Discussion

3.3.1 Regime Map

In multiphase microfluidic systems, it is common to build a map characterized by the Capillary number of each phase to identify the flow regimes and respective boundaries. Figure 3.5 shows such flow regime map, for $\chi = 533$, with data from experiments and also from simulations. In order to test the accuracy of the numerical code, the simulations were performed for conditions near the dripping-jetting transition. Since the flow regime map is a qualitative characterization of the multiphase microfluidic system, simulations were performed with $x/h = 0.04$ mesh. Although only one numerical result is in the jetting regime, it is near the critical capillary number, $\mathrm{Ca_{cri}} \approx 10^{-1}$ [17, 18], Figure 3.5. The main conclusion is that numerical method predicts well the flow conditions for the threading and dripping regimes.

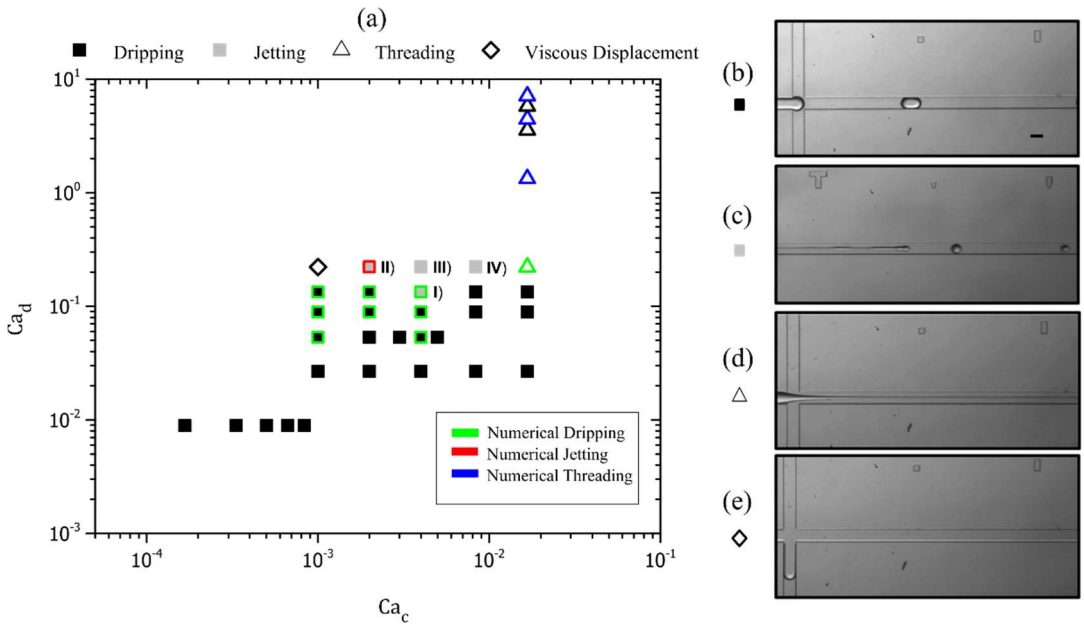

Figure 3.5. PDMS droplet formation ($\chi = 533$ and 2% SDS): (a) Flow map regime; (b) dripping (■); (c) jetting (■); (d) threading (△); (e) viscous displacement (◇). The numerical results are represented by the colored symbols. Scale bar: 100 μm.

3.3.2 Dripping Regime

Droplet formation

Droplet formation in the dripping regime begins with a cap of the dispersed phase moving slowly at the cross region (cap displacement –Figure 3.6 and Figure 3.7, phase I of the flow). As the dispersed phase blocks the flow of the continuous phase, the dispersed phase suffers a large acceleration (squeezing and pinching - Figure 3.6 and Figure 3.7, phase II of the flow). After the cap displacement, its velocity is nearby the mixture velocity, $U_{\mathrm{c+d}}$ ($U_{\mathrm{droplet}} \approx U_{\mathrm{c+d}} = U_{\mathrm{c}} + U_{\mathrm{d}}$, Figure 3.6 and Figure 3.7, phase III of the flow) and a thread starts to form, at the same time the continuous phase pushes the dispersed one. When the thread starts to be very thin, it breaks down (Figure 3.6– phase IV), owing to interfacial instabilities that spread both downstream and upstream the flow [6]. Droplets, smaller than the characteristic size of the channel $d < h$, tend to flow faster than the mixture velocity [17], $U_{\mathrm{c+d}}$ (Figure 3.7 – phase IV).

A specific condition regarding the generation of a sub-channel size droplet, Figure 3.6, was numerically studied and the results compared with Cubaud and Mason [17] experimental data, Figure 3.7. Although some temporal differences during the droplet formation are observed, approximately 15 ms (Figure 3.7), both temporal and spatial evolutions are satisfactorily comparable.

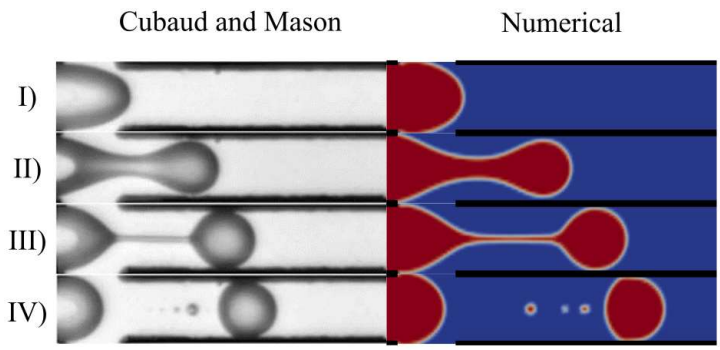

Figure 3.6. Comparison between Cubaud results and numerical data for the dripping regime ($\chi = 24$, $Q_{\mathrm{d}} = 0.3$ µL min^{-1}and $Q_{\mathrm{c}} = 4$ µL min^{-1}). Successive steps of the drop formation are represented: I) cap displacement; II) squeezing and pinching; III) tail stretching; and IV) complete breakup. Mesh resolution: x/h=0.04. XY midplane is shown. Scale bar: 100 µm.

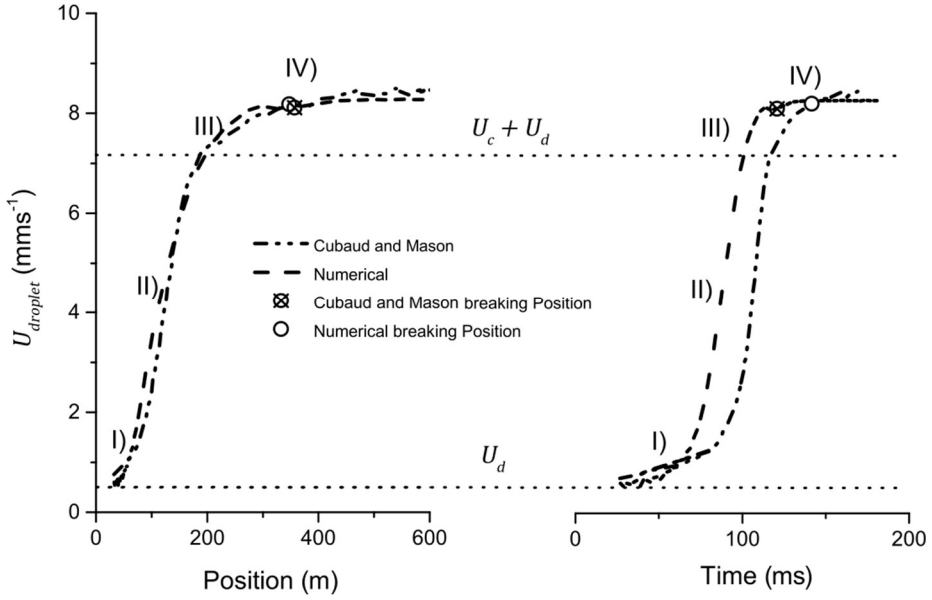

Figure 3.7. Dispersed phase velocity: a) spatial evolution; b) temporal evolution. Comparison between Cubaud and Mason (Cubaud and Mason, 2008) results and numerical data. Successive steps of the drop formation: I) cap displacement; II) squeezing and pinching; III) tail stretching; and IV) complete breakup. Dashed lines represent the dispersed phase velocity, U_{d}, and the mixture velocity, $U_{\mathrm{d}} + U_{\mathrm{c}}$. Fluid pair: $\chi = 24$, $Q_{\mathrm{d}} = 0.3$ and $Q_{\mathrm{c}} = 4$ μL min^{-1}.

Thread length

When the dispersed phase is squeezed by the continuous phase, a droplet starts to form and begins to move downstream but still connected to the carrier in the cross channel, Figure 3.1a. As the droplet moves, it pulls out a thread that eventually breaks due to the squeezing of the dispersed phase and to the appearing of instabilities both upstream and downstream the thread [6, 17]. Cubauld and Mason[17] quantified the thread length by the following correlation:

$$\frac{l}{h} = \mathrm{C_t}\frac{\mu_{\mathrm{d}}}{\sigma \mathrm{Ca_{cri}}}\frac{Q_{\mathrm{d}} + Q_{\mathrm{c}}}{2h^2} \tag{3.12}$$

where $\mathrm{C_t}$ is a numerical constant, $\mathrm{C_t} = 2.1$.

Threads from our experimental work are, on average, 38 % longer (2% SDS) and 117% (8% SDS) compared to Cubauld and Mason[17] correlation data, Figure 8a. Cubauld and Mason[17]did not use surfactant in the experiments.

Different viscosity ratios were simulated (Figure 3.8), $24 \leq \chi \leq 1480$. For $\chi \leq 94$, the numerical code is capable of predicting the thread length with an average deviation of 10 % and a maximum of 29 %, the later for the longest thread ($l \approx 6h$ for $\chi = 94$) For $\chi > 94$, the numerical code fails to accurately predict the thread length.

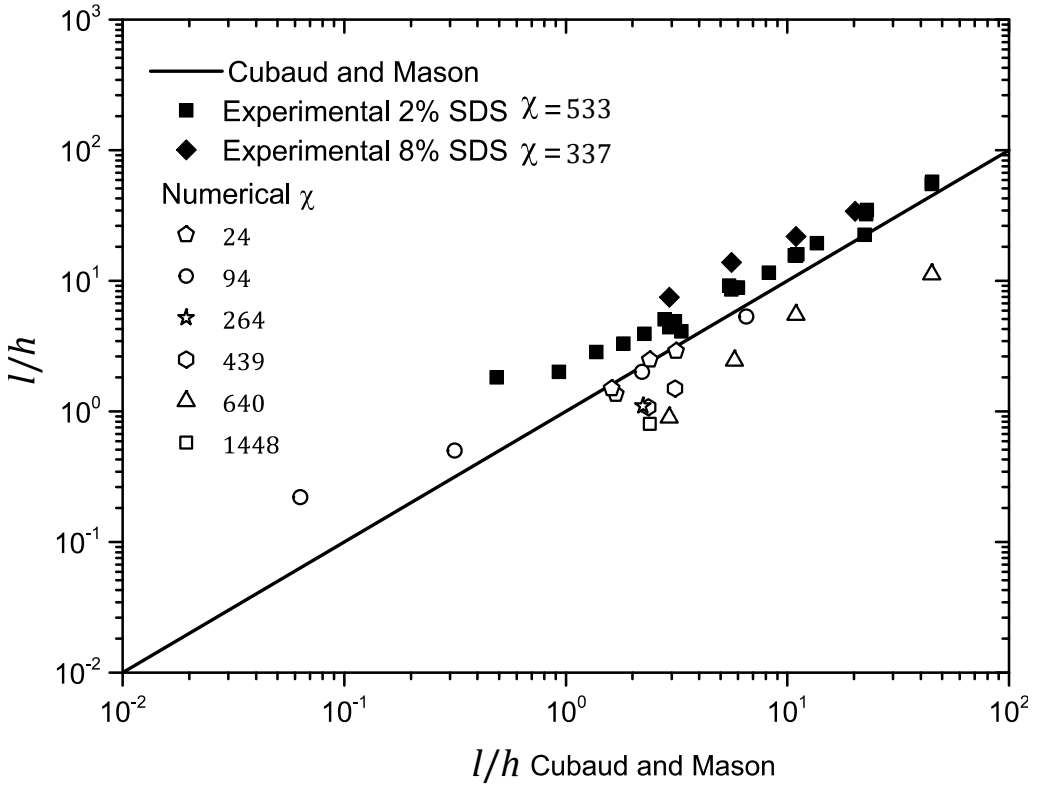

Figure 3.8. Dripping thread length: a) experimental data vs Cubauld and Mason [17] results for $\chi = 533$ and 337, 2% SDS and 8% SDS respectively; Numerical data versus Cubauld and Mason[17] results for $24 \leq \chi \leq 1480$.

Droplet length

Droplet length, *d*, is mainly determined during the squeezing and pinching stages Cubauld and Mason[17]. For $\chi \geq 24$, *d* strongly depends on the interfacial tension and

on the viscosity and flow rate of the continuous phase Cubauld and Mason[17] proposed two different fittings depending on the droplet length:

$$\frac{d}{h} \approx \begin{cases} 2.2 \times 10^{-4} \, (\alpha_c Ca_c)^{-1} & for \; d > 2.5h \\ 0.5 \, (\alpha_c Ca_c)^{-0.17} & for \; d < 2.5h \end{cases} \tag{3.13}$$

Numerical results, for the droplets length in the range $24 \leq \chi \leq 1480$, are in good agreement with Cubauld and Mason[17] correlations data, with deviations ranging from 1% to 25 %, Figure 3.9a. Although the numerical code fails to predict the thread length for $\chi > 94$, it predicts well the droplet length which, in most of the applications, is the important parameter.

For $\chi = 533$, experimental data follows well Cubauld and Mason[17] correlation for $d < 2.5h$ until a critical value of $\alpha_c Ca_c \approx 2 \times 10^{-3}$, Figure 3.9b. However, the droplet length starts to increase for $\alpha_c Ca_c > 2 \times 10^{-3}$ and then deviates from the Cubauld and Mason [17] correlation. The observed deviation is independent of the surfactant concentration and appears to be independent of Ca_d, Figure 3.9.b.

An interesting result is the shift of the droplet length occurring, for all Ca_d, at a critical thread length of $l \approx 20h$, Figure 3.10.

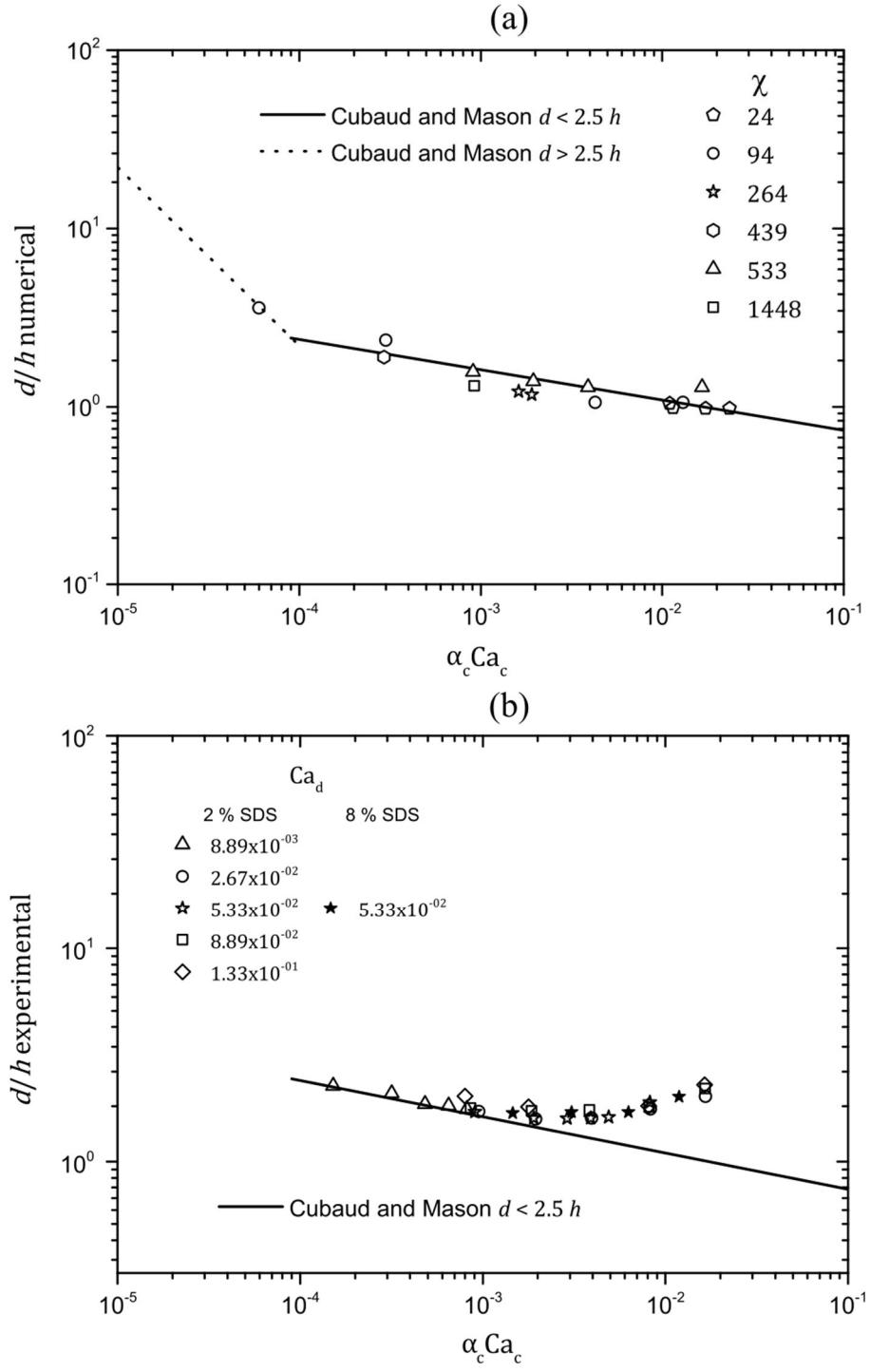

Figure 3.9. Droplet length in the dripping regime: a) Numerical data Cubauld and Mason[17] results for $94 \leq \chi \leq 1448$; b) Experimental data for different values of Ca_d, $\chi = 533$ and 337 for 2% SDS and 8% SDS respectively.

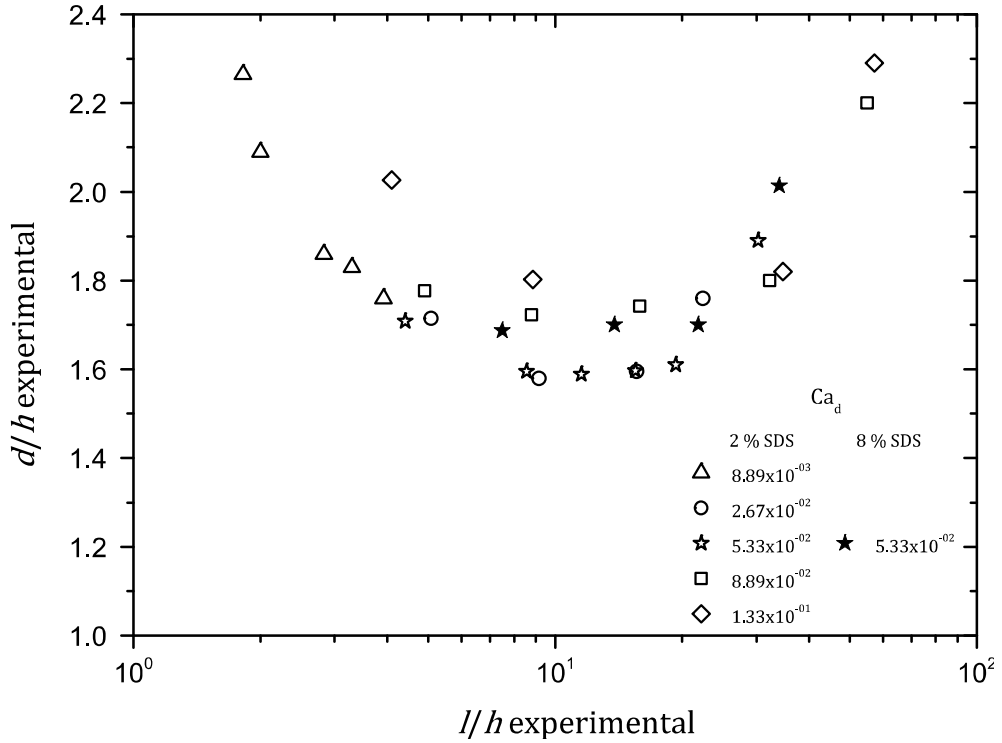

Figure 3.10. Dripping experimental droplet length versus thread length data for different values of Ca_d. Fluid pair: χ = 533 and 337 for 2 % SDS and 8 % SDS respectively.

The presence of asymmetrical flows are reported in the literature for high viscosity ratio in a flow-focusing geometry [30], nonetheless it is only reported at the squeezing/pinching stages near the cross region. The symmetrical/asymmetrical flows during drop breakup (a critical length, $l \approx 20h$) are clearly seen in Figure 3.11a and b, respectively. The asymmetrical case develops into a symmetrical elongated droplet (Figure 3.11c).

The numerical code predicts well the droplet length for all viscosity ratios when surfactant is not used. When surfactant is used, it affects droplet length for $\alpha_c Ca_c > 2 \times 10^{-3}$.

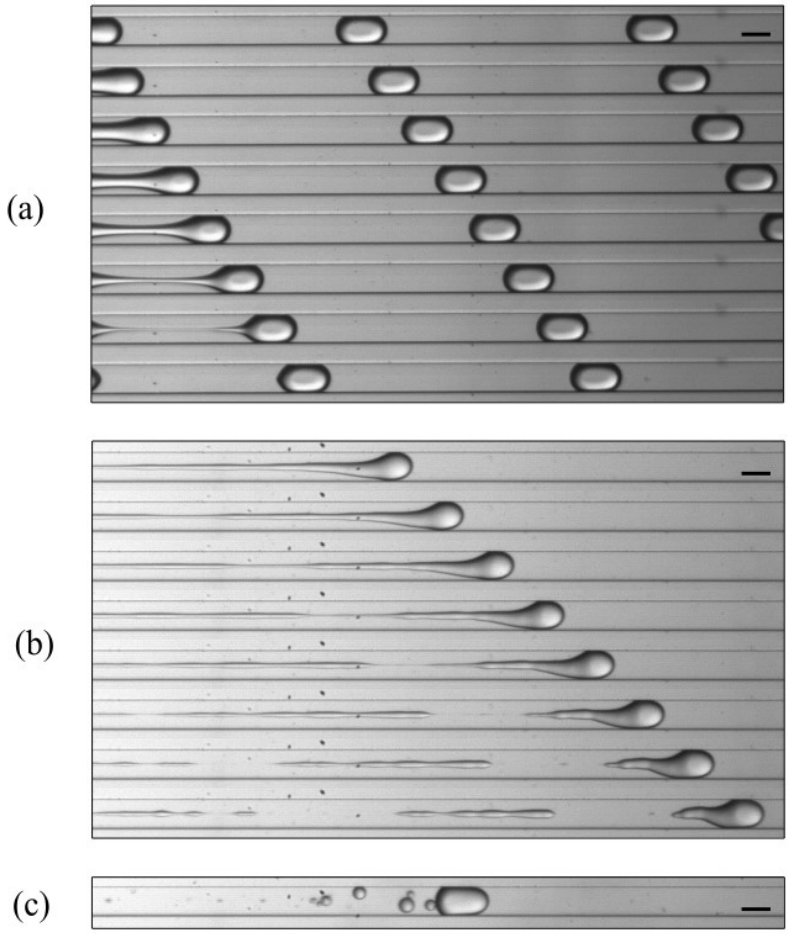

Figure 3.11. Symmetrical (a) and asymmetrical for $l > 20h$ (b) thread break. Fluid pair: $\chi = 533$, 2 % SDS: (a) Q_d= 1.5 and Q_c = 50 (µL min^{-1}); (b) Q_d= 0.3 and Q_c = 50 (µL min^{-1}); (c) stable droplet after formation for Q_d= 0.3 and Q_c = 50 (µL min^{-1}). Scale bar: 100 µm.

3.3.3 Jetting Regime

At $Ca_d > 10^{-1}$, Figure 3.5, the dispersed phase breaks farther from the junction and the thread does not recoil, developing a jet. Interfacial convective instabilities prompt the dispersed phase to form droplets at the end of the jet [9, 11, 17, 18, 58, 59], Figure 3.1b.

Experimental results

For a better understanding of the experimental jetting results, in Figure 3.12 all the studied jetting experimental points are represented by roman numerals, I-IV. In a previous study, with the same experimental fluid pair and channel geometry, it was observed that this regime produces polydispersed droplets. To have an overall statistical description of the polydispersity, it is important to analyse the coefficient of variance (CV) of the normalized droplet diameter (or length), defined by:

$$\mathrm{CV} = \frac{\sqrt{\frac{\sum_{i=1}^{n}(D/h_i - \overline{D/h})^2}{n-1}}}{D/h} \times 100 \tag{3.14}$$

where D/h_i is the dimensionless droplet size of droplet i , n represents the measures done for each condition and $\overline{D/h}$ the average dimensionless droplet size.

Figure 3.12 depicts the breakup and the droplets formed for all experimental points (CV of the normalized droplet diameter for each experiment is referred in the caption of the figure). The number of conditions studied for the jetting regime is smaller compared to those of the dripping regime since the jetting was mainly studied to delimit the dripping and build the regime map.

When the flow rate of the continuous phase is not sufficiently high (for a given flowrate of the dispersed phase), Figure 3.12 I-III, secondary droplets form and the CV of the normalized droplet diameter is large, $20\,\% \leq \mathrm{CV} \leq 105\,\%$. For the highest continuous flow rate, Figure 3.12-IV, the jet droplets are much more monodispersed, $\mathrm{CV} \approx 13\%$, nonetheless still above the value found in the dripping regime, $\mathrm{CV} \leq 3\%$ [18].

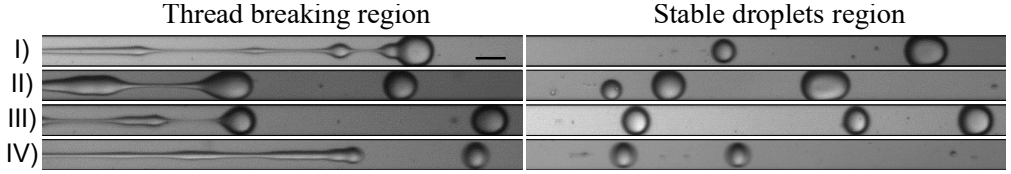

Figure 3.12. Experimental thread breaking and droplets formation: I) Q_{d}= 1.5 and Q_{c} = 24, CV ≈ 32 %; II) Q_{d}= 2.5 and Q_{c} = 12 , CV ≈ 105 %; III) Q_{d}= 2.5 and Q_{c} = 24, CV ≈ 20 %; IV) Q_{d}= 2.5 and Q_{c} = 50 , CV ≈ 13 % (both in μL min^{-1}). Fluid pair: χ = 533, 2 % SDS. Scale bar: 100 μm.

Both thread length and droplet diameter (or length) were compared to Cubaud and Mason [13] correlations.

For the droplet diameter Cubaud and Mason [13] correlation is as follows:

$$\frac{D}{h} \approx 3.1 \left(\frac{Q_\mathrm{d}}{2Q_\mathrm{c}}\right)^{1/2} \tag{3.15}$$

The experimental diameter of the droplets is larger than the one given by Cubaud and Mason [17] correlation Figure 3.13a. However, the diameter of the droplets is independent of the surfactant concentration

For the thread length Cubaud and Mason [17] found the fitting:

$$\frac{L}{h} = \frac{\mathrm{C_j} \frac{\mu_\mathrm{d}}{\sigma} \frac{8}{\pi h \mathrm{Ca_{cri}}} \left(\frac{Q_\mathrm{d} Q_\mathrm{c}}{2}\right)^{\frac{1}{2}}}{h} \tag{3.16}$$

where $\mathrm{C_j}$ is a numerical constant close to unit, $\mathrm{C_j} = 1$.

All experimental data exhibit larger thread length compared to Cubaud fitting, Figure 3.13b. The thread length increases with the surfactant concentration.

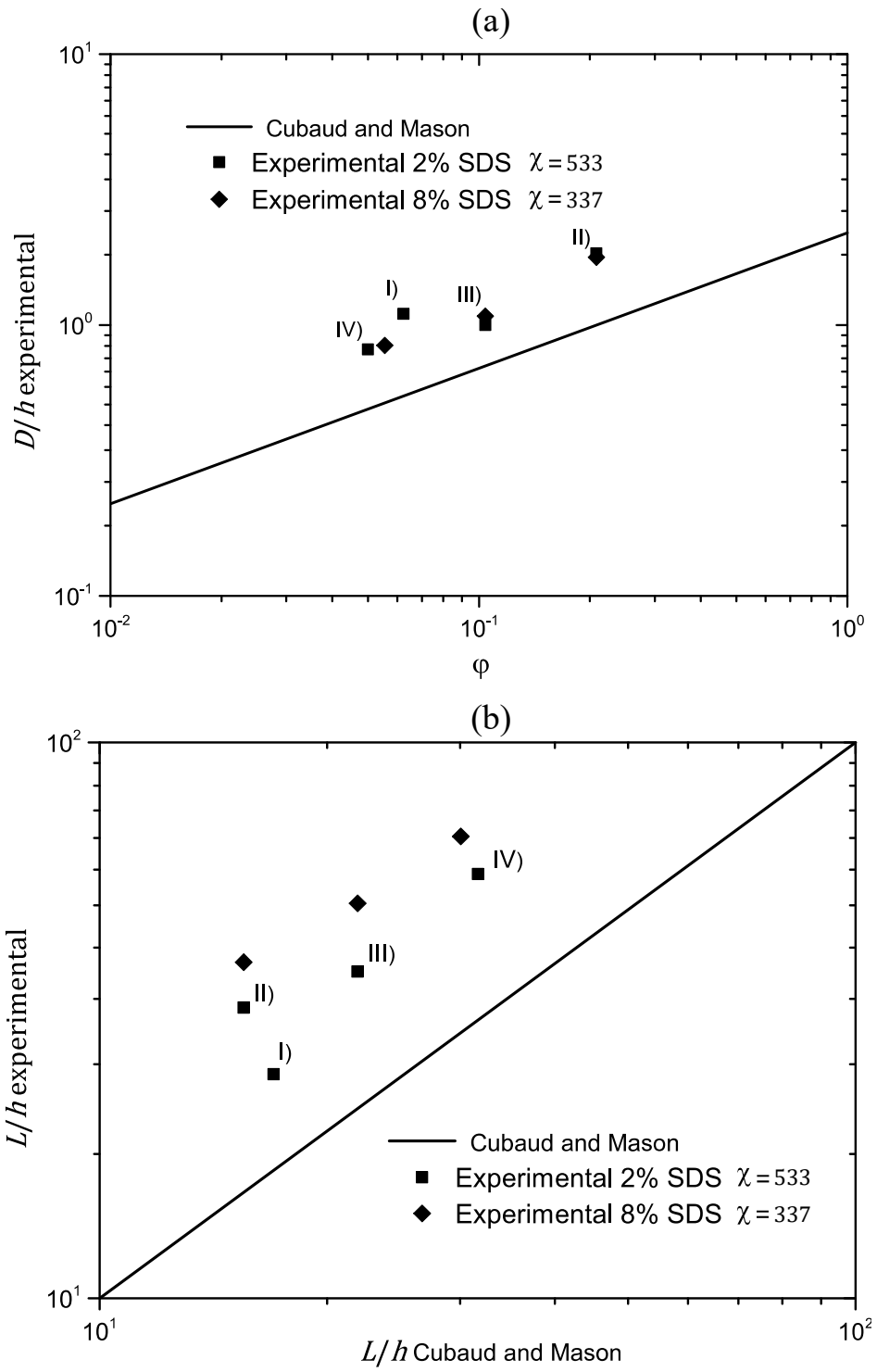

Figure 3.13. Comparison between jetting experimental results (χ = 533 and 337, 2 % SDS and 8 % SDS respectively) and Cubaud and Mason [17] data: a) droplet length/diameter; b) thread length. Roman numerals in the experimental points are from the flow regime map.

Numerical results

Jetting numerical simulations were only performed for $\chi = 24$ fluid pair. This viscosity ratio was selected because Cubaud and Mason [17] published images of the flow in the corresponding jetting regime. Contrarily to our experimental data, Cubaud and Mason [17] obtained monodispersed droplets.

According to Figure 3.14, the threads from the numerical results are longer than those from Cubaud and Mason [17] (a), some even longer than the numerical channel domain (b).

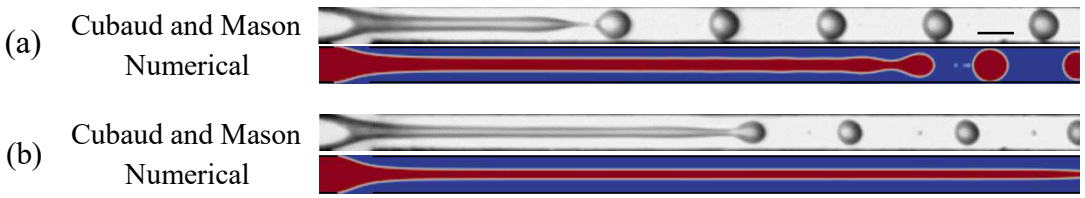

Figure 3.14. Cubaud and Mason [17] images *vs* numerical jetting droplet formation images for a $\chi = 24$: a) Q_d= 1 and Q_c = 4; b) Q_d= 1 and Q_c = 8 (µL min^{-1}). Mesh resolution: x/h=0.04. XY midplane is shown. Scale bar: 100 µm.

Although the thread length obtained numerically is higher than Cubaud and Mason [17] fitting, Figure 3.15b, the numerical droplet diameter is in good agreement with the fitting, Figure 3.15a. The numerical code is capable of predicting, for the conditions studied, the droplet diameter, but fails to predict the thread length.

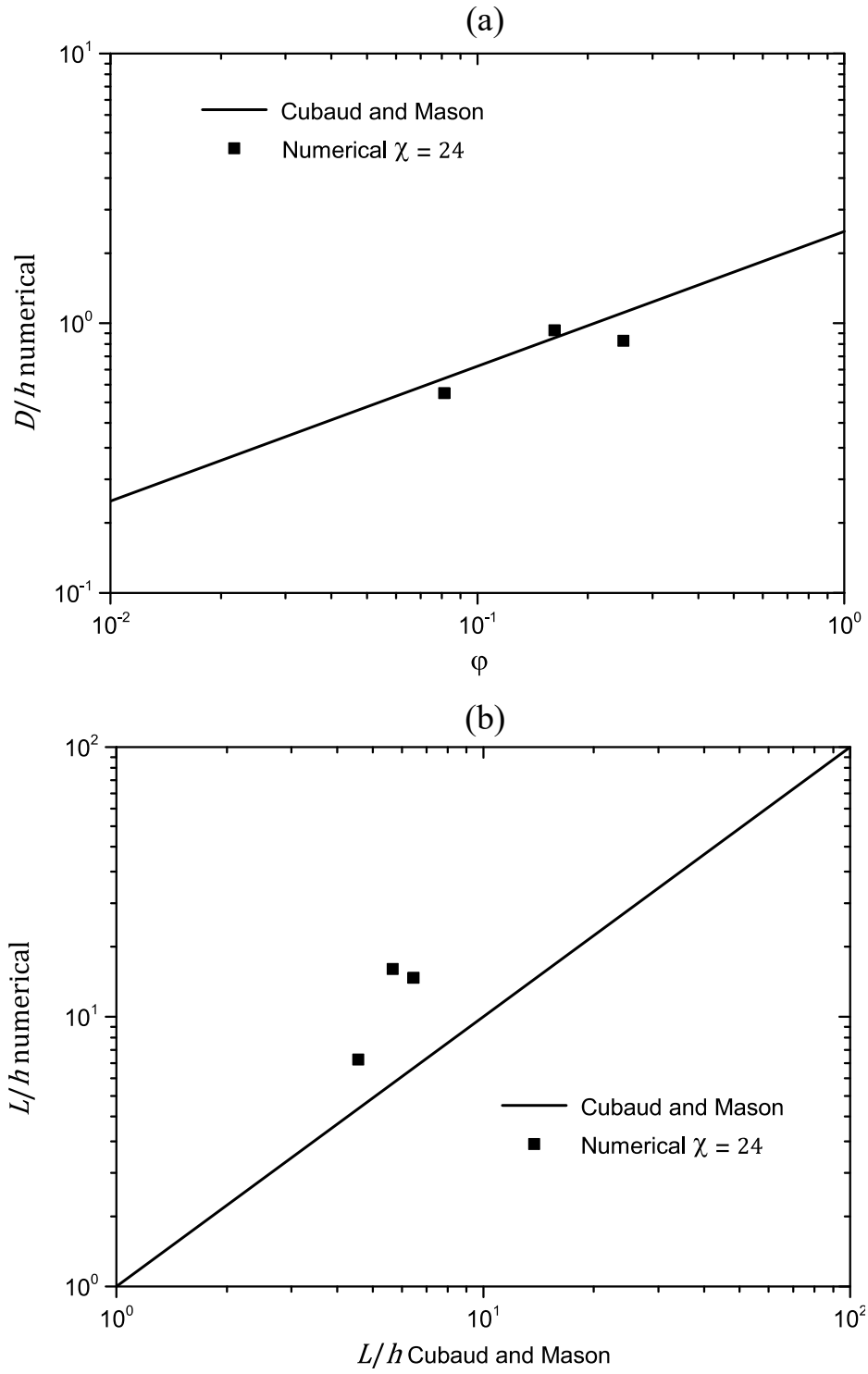

Figure 3.15. Numerical data versus Cubaud and Mason [17] results for $\chi = 24$: a) droplet diameter; b) thread length.

3.3.4 Threading Regime

The threading regime is characterized by the formation of a core stable viscous thread travelling confined by a less viscous fluid. This regime typically appears at $\mathrm{Ca_d} \gg 10^{-1}$ [17, 18] and is a good steady state benchmark for the numerical results, since forms a quasi-static thread and its thickness is constant in time.

Numerical results were compared with data obtained experimentally and also through Cubaud and Mason [17] correlation for the thread diameter:

$$\frac{\varepsilon}{h} \approx \left(\frac{Q_\mathrm{d}}{2Q_\mathrm{c}}\right)^{1/2} \tag{3.17}$$

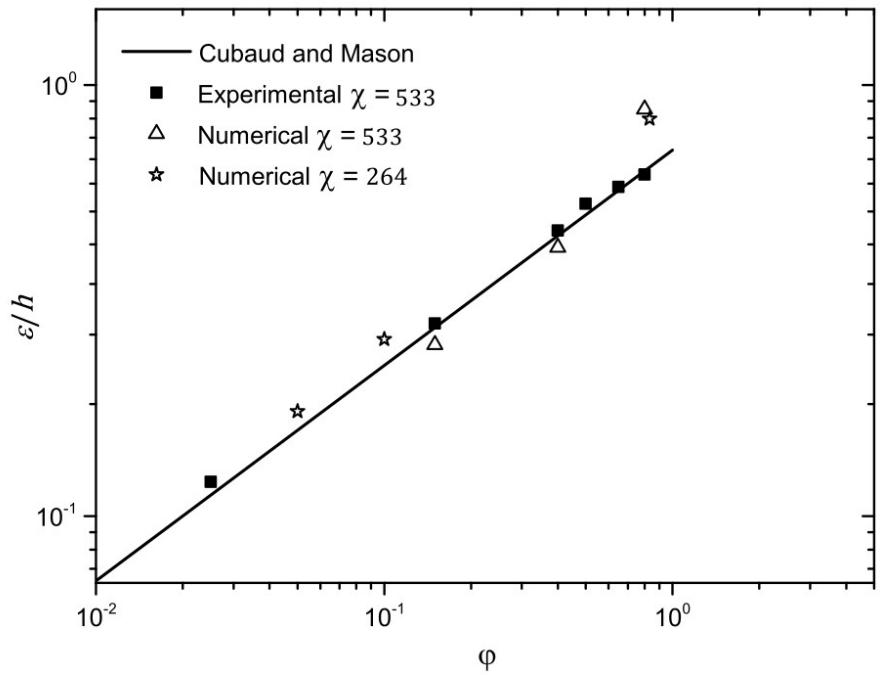

Figure 3.16. Thread normalized diameter, ε/h, for fluid viscosity ratios: $\chi = 533$ and $\chi = 264$. Experimental results were obtained for $\chi = 533$, 2 % SDS.

The viscosity ratios of the pair of fluids studied were high: χ = 264 and 533. According to Figure 3.16, numerical data are in a good agreement with both

experimental and fitting results, except for the highest flow rate ratio. Excluding these values, the average relative deviation is around 9 %.

In Figure 3.17, experimental and numerical images can be compared. The good agreement is visible, except, again, for the highest flow rate ratio where the dispersed phase in the numerical image occupies almost the entire channel, Figure 3.17c.

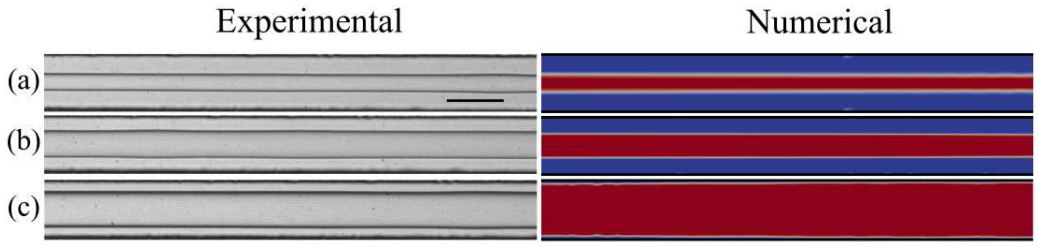

Figure 3.17. Experimental *vs* numerical images for the thread diameter (χ = 533, 2 % SDS): a) Q_d= 15 and Q_c = 100; b) Q_d= 40 and Q_c = 100 and; c) Q_d = 80 and Q_c = 100 (µL min^{-1}). Mesh resolution: x/h=0.04. XY midplane is shown. Scale bar: 100 µm.

3.4 Discussion

The experimental system under study is a two phase liquid-liquid system in which the continuous phase is water containing surfactant (SDS) and the dispersed phase is PDMS (Sylgard 284 kit 4:6). The surfactant SDS is soluble on the continuous phase but insoluble on the dispersed phase. Two surfactant concentrations were studied, 7 and 28 times the critical micelle concentration.

The experimental measurements in static conditions, Table 3.2, show that in this range the interfacial tension is independent of the surfactant concentration. In dynamic conditions, it has been documented that the surfactant in the interface may be subjected to transport along the interface, leading to concentration gradients and consequently to Marangoni forces, i.e. forces tangential to the interface [60, 61]. Mass transport limitations of the surfactant may also lead to interfacial tensions smaller than those measured in static conditions [62, 63]. The rheological properties of the interface, such as the shear and dilatational viscosity and elasticity, also depend on the surfactant concentration and are influenced by mass transport limitations [64, 65].

Cubaud and Mason [17] study, used for comparison, was conducted without any surfactant and so Marangoni forces and other effects of mass transport limitations were

not a factor. The numerical method followed in the present study does not capture mass transport limitations. In the experimental study developed, the effect of two surfactant concentrations was studied to infer the relevance of mass transport limitations. If the results obtained in the experimental study are independent of the surfactant concentration, it means that the interfacial tension and the rheological properties of the interface are not being affected by mass transport limitations.

Table 3.4. Comparison of the numerical and experimental results with data obtaind by Cubaud and Mason [17]

Regime	Topic	Numerical	Exceptions	Experimental	Exceptions
Threading	Thread diameter	Accurate prediction	Large flow rate ratio > 0.9	Coincident	Large flow rate ratio
Jetting	Droplet diameter	Accurate prediction	-	Higher values	-
	Thread length	Numerical thread is longer	-	Higher values	-
Dripping	Droplet length	Acceptable prediction	-	Accurate prediction for $\alpha_c Ca_c \leq 2 \times 10^{-3}$	$\alpha_c Ca_c > 2 \times 10^{-3}$
	Thread length	Numerical thread is slightly smaller	Higher viscosity ratios	Values slightly above	Lower lengths

Significant differences were observed between the experimental results and the data of Cubaud and Mason [17], Table 3.4. In the dripping regime, for $\alpha_c Ca_c > 2 \times 10^{-3}$, the droplet length is higher than expected from Cubaud and Mason [17] correlation, Figure 3.9b. To test if this length deviation also corresponds to a volume deviation, the diameters of the droplets were measured at the outlet under stagnant conditions. According to Figure 3.18, the length deviation is partly due to a change in the droplet shape, but even in static conditions the droplet length does not follow the decreasing trend observed by Cubaud and Mason [17]. In Figure 3.9b, it is also observed that the droplet length is independent of the surfactant concentration, suggesting that mass transport limitations have no significant effect on the interfacial tension during droplet formation. The effect of the surfactant on the rheology of the interface is probably the best explanation for the deviation observed and needs further investigation. Note, however, that the dynamics of the thread was found to be dependent of the

concentration, and as shown in Figure 3.10, the droplet length is correlated with the thread length.

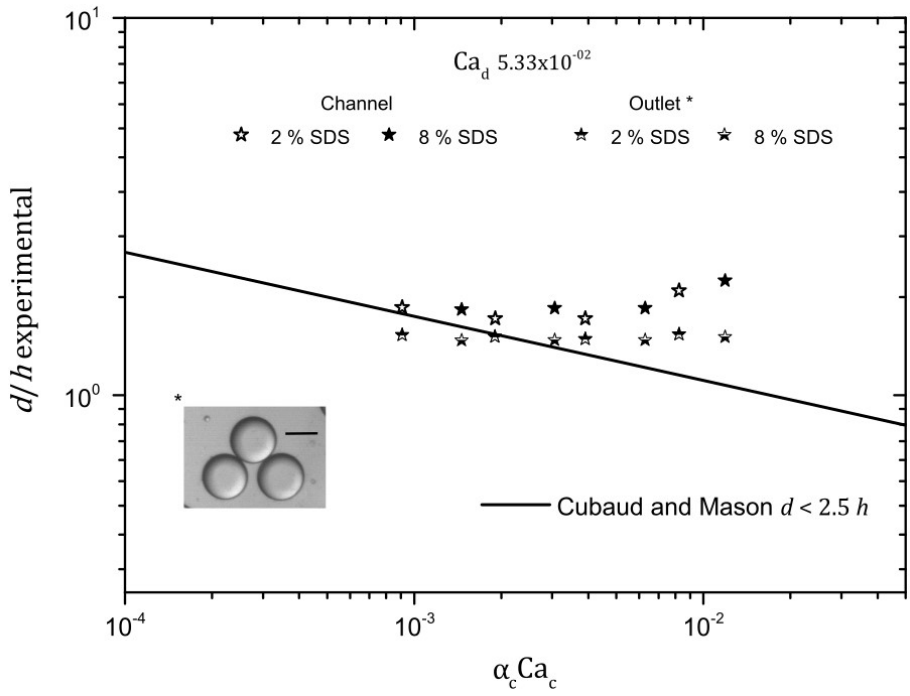

Figure 3.18. Experimental droplet length at the main channel and at the outlet in the dripping regime; $Ca_d = 5.33 \times 10^{-2}$, $\chi = 533$ and 337, SDS 2 % and 8 % respectively. Inset: droplet at the outlet. Scale bar: 100 µm.

For the dripping regime, the length of the thread is higher than that observed by Cubaud and Mason [17]. The thread formation is associated with the creation of interfacial area. To have constant concentration of the surfactant over the interface, the surfactant needs to be resupplied to the interface from the continuous phase at a rate proportional to the rate of surface creation. In our experiments, the thread length increases by increasing the surfactant concentration, Figure 3.8. The effective surface tension over the thread may be higher and Marangoni forces along the interface may form. The results suggest that this Marangoni forces are enhanced by the increase of the surfactant concentration. Marangoni forces act as an artificial elasticity that is superimposed to the interface elastic, which also depends on the surfactant concentration.

In the jetting regime, the droplet diameters are larger than those given by Cubaud and Mason [17] correlation. The droplet diameter is also independent of the surfactant concentration, implying that the process that leads to the droplet formation is not affected by mass transport limitations and most probably Marangoni forces are not involved. However, the length of the threads obtained experimentally are higher than those given by Cubaud and Mason [17] correlation and increases with the increase of the surfactant concentration. This result suggests that the surfactant contributes to the thread stabilization and that mass transport effects have a role in the stabilization process. Again, Marangoni forces and concentration dependent elasticity of the interface may have a role.

Images of Figure 3.11 show two unusual phenomena that require further explanation. For $l > 20h$, the droplet forms asymmetrically (Figure 3.11b) and an elongated droplet develops (Figure 3.11c). The observed behaviour could be attributed to the presence of an unbalanced surfactant adsorption at the thread interface. As the dispersed thread stretches, the adsorption rate of surfactant can be lower than the rate of newly interface generation and consequently appear zones, at the interface, with uneven SDS adsorption. Although SDS is present at 7-28 times above its critical micelle concentration, CMC (0.28 %), it may be insufficient to cover the interface for all flow conditions. At $\alpha_c Ca_c > 2 \times 10^{-3}$ and $l > 20h$, the unbalance distribution of SDS around the forming droplet can lead to asymmetric distribution of surfactant and consequently to asymmetric interfacial tension and asymmetric shape of the forming droplet. The elongated shape of the droplet could also be a problem of maldistribution of surfactant. The droplet interface is moving from the front to the back of the droplet, which may lead to a depletion of surfactant in the front of the droplet and an increase of the surfactant in the back. The importance of the surfactant effect is reported on droplet formation in previous works in different conditions [62, 63].

The numerical method can accurately predict the thread diameter in the threading regime, except for the case of flow rate ratio above 0.9. The numerical method can also predict accurately the droplet size in the dripping and jetting regimes. As for the thread length, in the dripping regime the numerical predictions are below the results obtained by Cubaud and Mason [17]. The deviation is higher for higher viscosity ratios. In the jetting regime, the thread lengths are higher than those obtained by Cubaud and Mason [17]. These results may be explained by the different thread widths

associated to each regime. In the dripping regime, the thread obtained numerically is thin and the mesh resolution is insufficient to solve it. In the jetting regime, the thread is wide and breaks due to instabilities along its length. The mesh resolution and the imposed symmetry both contribute to damp instabilities leading to longer threads. Nevertheless the numeric results predict well the thread diameter, ε, and the mode of maximum thread instability [66], $D/\varepsilon \approx 2.7$, of the jetting numerical results is in good agreement with the Cubaud and Mason [17] result of 2.9. To understand the limitations of the numerical method used in the present work, a comparison with the work developed in compound axisymmetric jets [67-69] is useful. In particular, Vu, Homma [67] used a front tracking method and have excellent agreement between numerical and experimental data for the jetting regime, although their work is validated in a 2D axisymmetric geometry with a comparatively larger main channel and the flow has significant inertial effects. In the present work, inertial effects are negligible and the width of the inlet is equal to the width of the main channel.

3.5 Conclusions

In this work we performed experimental and numerical studies concerning the formation of droplets of viscous fluids in a simple square section flow focusing geometry. By comparing the numerical, experimental and correlations from the literature data the following conclusions can be taken:

a) A regime map delimiting the boundaries of each regime was obtained for $\chi = 533$. The shifting conditions from dripping to jetting obtained in the experimental and numerical works are in good agreement and also concordant with the literature results for systems of lower viscosity ratio, $\mathrm{Ca_{cri}} \approx 10^{-1}$;

b) While the numerical method is able to predict the droplet size, either in the dripping as in the jetting regimes, it has limitations. In the jetting regime the size predictions are accurate for $\chi = 24$, but higher viscosity ratios need to be further studied to validate the droplet size predictions. The numerical method is unable to predict the thread length in the jetting and in the dripping regimes for $\chi > 94$. In the dripping regime, the limitations were attributed to the mesh resolution, while in the jetting regime are associated with numerical effects which damp instabilities.

c) Our experimental results for the droplets size and thread length fall off from Cubaud and Mason [17] correlations. In the case of the droplet length, the deviation is associated with a change in droplet shape. The droplet lengths obtained are not affected by surfactant mass transport limitations. Mass transport limitations play a role in the thread stability, both in the dripping and jetting regimes.

d) For the threading regime, the numerical and experimental results are in good agreement with Cubaud and Mason [17] correlations except when the flow rate ratio approaches unity.

Numerical studies can provide a better understanding on how the different experimental variables impact droplet formation. This study can provide a glance at the limitations of the numerical code in a flow focusing microfluidic system comprised of high viscosity ratio fluids. Further experimental studies need to be conducted to understand the influence of the surfactant on the droplet size in order to improve the numerical code accordingly. Also asymmetric phenomena were not considered in the numerical study and should be included in the future.

Acknowledgements

This work was funded by FEDER funds through COMPETE2020—Operational Programme for Competitiveness Factors (POCI) and National Funds (PIDDAC) through FCT (Fundação para a Ciência e a Tecnologia) under projects PEst-OE/EME/UI0532 and POCI-01-0145-FEDER-016861-PTDC/QEQ-FTT/4287/2014. J.Carneiro wants to thank Francisco Pimenta for the MATLAB® custom code.

Notation

Latin	Definition	Units
C_j	Jetting thread length constant	---
C_t	Dripping thread length constant	---
CV	Coefficient of variance	**(%)**
D	- Droplet axial length - Distance from a point to the interface	(m) (m)
D	Droplet diameter	(m)
$\overrightarrow{f_\sigma}$	Surface tension force term	(N m^{-1})
h	Channel characteristic dimension	(m)
H_ϕ	Heaviside weighting function	---
κ	Local mean interface curvature	---
l	Thread length of the dripping regime	(m)
L	Thread length of the jetting regime	(m)
$\vec{n}$	Unit normal vector	---
p	Pressure	(Pa)
Q	Volumetric flow rate	(m^3 s^{-1})
Q_c	Volumetric flow rate of the continuous phase	(m^3 s^{-1})
Q_d	Volumetric flow rate of the dispersed phase	(m^3 s^{-1})
t	Time	(s)
U	Velocity	(m s^{-1})
U_c	Velocity of the continuous phase	(m s^{-1})
U_d	Velocity of the dispersed phase	(m s^{-1})

$U_{\mathrm{c+d}}$	Mixture velocity	(m s^{-1})
U_{droplet}	Droplet velocity	(m s^{-1})
$\vec{v}$	Velocity vector	(m s^{-1})
x	Cell size	(m)
$\vec{x}$	Vector position	---

Greek	**Definition**	**Units**
α	- Continuous phase flow ratio	---
	- Volume fraction	---
$\delta()$	Dirac function	---
ε	Thread diameter	(m)
ϵ	Interface thickness	(m)
μ	Dynamic viscosity	(Pa s)
μ_{c}	Dynamic viscosity of the continuous phase	(Pa s)
μ_{d}	Dynamic viscosity of the dispersed phase	(Pa s)
ρ	Fluid density	(kg m^{-3})
σ	Interfacial tension	(N m^{-1})
φ	Volumetric flow rates ratio	(m^3 s^{-1})
ϕ	Signed distance from a point to the interface	---
χ	Viscosity ratio	---

Dimensionless numbers	Definition
Ca	Capillary number
Ca_c	Capillary number of the continuous phase
Ca_d	Capillary number of the dispersed phase
Ca_{cri}	Critical capillary number
Re	Reynolds number
Re_d	Reynolds number of the dispersed phase
We	Weber number
We_d	Weber number of the dispersed phase

Acronyms	Definition
CLSVOF	Coupled level-set and volume of fluid method
CSF	Continuum surface force model
LS	Level-set method
MFFD	Microfluidic Flow Focusing Device
PDMS	Polydimethylsiloxane
PISO	Pressure-Implicit with Splitting Operators
PLIC	Piecewise Linear Interpolation Calculation
PRESTO!	PREssure STaggering Option
QUICK	Quadratic Upstream Interpolation for Convective Kinematics
SDS	Sodium dodecyl sulphate
SU-8	Designation of epoxi-bored photoresist
VOF	Volume of fluid method

References

1. Lagus, T.P. and J.F. Edd, *A review of the theory, methods and recent applications of high-throughput single-cell droplet microfluidics.* Journal of Physics D: Applied Physics, 2013. **46**(11): p. 114005-114005.
2. Teh, S.-Y., et al., *Droplet microfluidics.* Lab on a Chip, 2008. **8**(2): p. 198-198.
3. Champion, J.A., Y.K. Katare, and S. Mitragotri, *Particle shape: A new design parameter for micro- and nanoscale drug delivery carriers.* Journal of Controlled Release, 2007. **121**(1-2): p. 3-9.
4. Xu, Q., et al., *Preparation of Monodisperse Biodegradable Polymer Microparticles Using a Microfluidic Flow-Focusing Device for Controlled Drug Delivery.* Small, 2009. **5**(13): p. 1575-1581.
5. Day, P., A. Manz, and Y. Zhang, *Microdroplet Technology*. 2012. 249-249.
6. Nunes, J.K., et al., *Dripping and jetting in microfluidic multiphase flows applied to particle and fibre synthesis.* Journal of Physics D: Applied Physics, 2013. **46**(11): p. 114002-114002.
7. Wan, J., *Microfluidic-based synthesis of hydrogel particles for cell microencapsulation and cell-based drug delivery.* Polymers, 2012. **4**(2): p. 1084-1108.
8. Anna, S.L. and H.C. Mayer, *Microscale tipstreaming in a microfluidic flow focusing device.* Physics of Fluids, 2006. **18**(12).
9. Anna, S.L., *Droplets and Bubbles in Microfluidic Devices.* Annual Review of Fluid Mechanics, 2016. **48**(1): p. 285-309.
10. Zhu, P. and L. Wang, *Passive and active droplet generation with microfluidics: a review.* Lab Chip, 2017. **17**(1): p. 34-75.
11. Utada, A.S., et al., *Dripping to Jetting Transitions in Coflowing Liquid Streams.* Physical Review Letters, 2007. **99**(9): p. 094502-094502.
12. Yang, L., et al., *Visualization and characterization of gas-liquid mass transfer around a Taylor bubble right after the formation stage in microreactors.* Chemical Engineering Science, 2016. **143**: p. 364-368.
13. Garstecki, P., et al., *Formation of droplets and bubbles in a microfluidic T-junction—scaling and mechanism of break-up.* Lab on a Chip, 2006. **6**(3): p. 437-437.
14. Anna, S.L., N. Bontoux, and H.A. Stone, *Formation of dispersions using "flow focusing" in microchannels.* Applied Physics Letters, 2003. **82**(3): p. 364-366.
15. Baroud, C.N., et al., *Dynamics of microfluidic droplets.* Lab on a Chip, 2010. **10**(16): p. 2032-2032.

16. Seemann, R., et al., *Droplet based microfluidics.* Reports on Progress in Physics, 2012. **75**(1): p. 016601-016601.

17. Cubaud, T. and T.G. Mason, *Capillary threads and viscous droplets in square microchannels.* Physics of Fluids, 2008. **20**(5): p. 1-11.

18. Carneiro, J., et al., *PDMS droplet formation and characterization by hydrodynamic flow focusing technique in a PDMS square microchannel.* Journal of Micromechanics and Microengineering, 2016. **26**(10): p. 105013-105013.

19. Dendukuri, D. and P.S. Doyle, *The synthesis and assembly of polymeric microparticles using microfluidics.* Advanced Materials, 2009. **21**(41): p. 4071-4086.

20. Mata, A., A.J. Fleischman, and S. Roy, *Characterization of polydimethylsiloxane (PDMS) properties for biomedical micro/nanosystems.* Biomedical microdevices, 2005. **7**(4): p. 281-293.

21. Di Benedetto, F., et al., *Rolling particle lithography by soft polymer microparticles.* Soft Matter, 2013. **9**(7): p. 2206-2206.

22. Jiang, K., et al., *Microfluidic synthesis of monodisperse PDMS microbeads as discrete oxygen sensors.* Soft Matter, 2012. **8**(4): p. 923-926.

23. Muñoz-Sánchez, B.N., et al., *Generation of micro-sized PDMS particles by a flow focusing technique for biomicrofluidics applications.* Biomicrofluidics, 2016. **10**(1): p. 1-11.

24. Carneiro, J., et al., *Visualization of PDMS Microparticles Formation for Biomimetic Fluids.* Micro and Nanosystems, 2015: p. 154-158.

25. Seo, M., et al., *Continuous microfluidic reactors for polymer particles.* Langmuir, 2005. **21**(25): p. 11614-11622.

26. Nie, Z., et al., *Emulsification in a microfluidic flow-focusing device: Effect of the viscosities of the liquids.* Microfluidics and Nanofluidics, 2008. **5**(5): p. 585-594.

27. Ward, T., et al., *Microfluidic flow focusing: Drop size and scaling in pressure versus flow-rate-driven pumping.* Electrophoresis, 2005. **26**(19): p. 3716-3724.

28. Christopher, G.F. and S.L. Anna, *Microfluidic methods for generating continuous droplet streams.* Journal of Physics D: Applied Physics, 2007. **40**(19): p. R319-R336.

29. Fu, T., et al., *Droplet formation and breakup dynamics in microfluidic flow-focusing devices: From dripping to jetting.* Chemical Engineering Science, 2012. **84**: p. 207-217.

30. Du, W., et al., *Breakup dynamics for high-viscosity droplet formation in a flow-focusing device: Symmetrical and asymmetrical ruptures.* AIChE Journal, 2016. **62**(1): p. 325-337.

31. Wu, P., et al., *Drag-induced breakup mechanism for droplet generation in dripping within flow focusing microfluidics.* Chinese Journal of Chemical Engineering, 2015. **23**(1): p. 7-14.

32. Bardin, D. and A.P. Lee, *Low-cost experimentation for the study of droplet microfluidics.* Lab Chip, 2014. **14**(20): p. 3978-3986.

33. van Loo, S.p., et al., *Droplet formation by squeezing in a microfluidic cross-junction.* Microfluidics and Nanofluidics, 2016. **20**(10): p. 1-12.

34. Abate, A.R., et al., *Impact of inlet channel geometry on microfluidic drop formation.* Physical Review E - Statistical, Nonlinear, and Soft Matter Physics, 2009. **80**(2): p. 1-5.

35. Bardin, D., et al., *High-speed, clinical-scale microfluidic generation of stable phase-change droplets for gas embolotherapy.* Lab on a chip, 2011(23): p. 3990-3998.

36. Jensen, M.J., H.A. Stone, and H. Bruus, *A numerical study of two-phase Stokes flow in an axisymmetric flow-focusing device.* Physics of Fluids, 2006. **18**(7): p. 1-11.

37. Lee, W., L.M. Walker, and S.L. Anna, *Role of geometry and fluid properties in droplet and thread formation processes in planar flow focusing.* Physics of Fluids, 2009. **21**(3).

38. Tan, Y.-C., V. Cristini, and A.P. Lee, *Monodispersed microfluidic droplet generation by shear focusing microfluidic device.* Sensors and Actuators B: Chemical, 2006. **114**(1): p. 350-356.

39. Liu, H. and Y. Zhang, *Droplet formation in microfluidic cross-junctions.* Physics of Fluids, 2011. **23**(8).

40. Li, Y., et al., *Control of the breakup process of viscous droplets by an external electric field inside a microfluidic device.* Soft Matter, 2015. **11**: p. 3884-3899.

41. Jia, H.W. and P. Zhang, *Investigation of the Taylor bubble under the effect of dissolution in microchannel.* Chemical Engineering Journal, 2016. **285**: p. 252-263.

42. Shi, Y., G.H. Tang, and H.H. Xia, *Lattice Boltzmann simulation of droplet formation in T-junction and flow focusing devices.* Computers and Fluids, 2014. **90**(September): p. 155-163.

43. Tryggvason, G., M. Ma, and J. Lu, *DNS–Assisted Modeling of Bubbly Flows in Vertical Channels.* Nuclear Science and Engineering, 2016. **184**(3): p. 312-320.

44. Bo, W., et al., *A Robust Front Tracking Method: Verification and Application to Simulation of the Primary Breakup of a Liquid Jet.* SIAM Journal on Scientific Computing, 2011. **33**(4): p. 1505-1524.

45. Ma, M., J. Lu, and G. Tryggvason, *Using statistical learning to close two-fluid multiphase flow equations for bubbly flows in vertical channels.* International Journal of Multiphase Flow, 2016. **85**: p. 336-347.

46. Ma, M., J. Lu, and G. Tryggvason, *Using statistical learning to close two-fluid multiphase flow equations for a simple bubbly system.* Physics of Fluids, 2015. **27**(9): p. 092101.

47. Cristini, V. and Y.-C. Tan, *Theory and numerical simulation of droplet dynamics in complex flows—a review.* Lab on a Chip, 2004. **4**(4): p. 257-264.

48. Sussman, M. and E.G. Puckett, *A Coupled Level Set and Volume-of-Fluid Method for Computing 3D and Axisymmetric Incompressible Two-Phase Flows.* Journal of Computational Physics, 2000. **162**(2): p. 301-337.

49. Hirt, C.W. and B.D. Nichols, *Volume of fluid (VOF) method for the dynamics of free boundaries.* Journal of Computational Physics, 1981. **39**(1): p. 201-225.

50. Sussman, M., P. Smereka, and S. Osher, *A Level Set Approach for Computing Solutions to Incompressible Two-Phase Flow.* Journal of Computational Physics, 1994. **114**(1): p. 146-159.

51. Brackbill, J.U., D.B. Kothe, and C. Zemach, *A continuum method for modeling surface tension.* Journal of Computational Physics, 1992. **100**(2): p. 335-354.

52. Lafaurie, B., et al., *Modelling Merging and Fragmentation in Multiphase Flows with SURFER.* Journal of Computational Physics, 1994. **113**(1): p. 134-147.

53. Abadie, T., et al., *Hydrodynamics of gas-liquid Taylor flow in rectangular microchannels.* Microfluidics and Nanofluidics, 2012. **12**(1-4): p. 355-369.

54. van Baten, J.M. and R. Krishna, *CFD simulations of mass transfer from Taylor bubbles rising in circular capillaries.* Chemical Engineering Science, 2004. **59**(12): p. 2535-2545.

55. Fletcher, D.F. and B.S. Haynes, *CFD simulation of Taylor flow: Should the liquid film be captured or not?* Chemical Engineering Science, 2016. **167**: p. 334-335.

56. Di Miceli Raimondi, N., et al., *Experiments of mass transfer with liquid-liquid slug flow in square microchannels.* Chemical Engineering Science, 2014. **105**: p. 169-178.

57. de Gennes, P.G., *Wetting: statics and dynamics.* Reviews of Modern Physics, 1985. **57**(3): p. 827-863.

58. Huerre, P., *Local and Global Instabilities in spacially developing flows.* Annual Review of Fluid Mechanics, 1990. **26**: p. 473-537.

59. Rayleigh, L., *On the Capillary Phenomena of Jets.* Proceedings of the Royal Society of London, 1879. **29**(196-199): p. 71-97.

60. Kamat, P.M., et al., *Role of Marangoni stress during breakup of surfactant-covered liquid threads: Reduced rates of thinning and microthread cascades.* Physical Review Fluids, 2018. **3**(4): p. 043602.

61. Hosokawa, S., et al., *Experimental evaluation of Marangoni stress and surfactant concentration at interface of contaminated single spherical drop using spatiotemporal filter velocimetry.* International Journal of Multiphase Flow, 2017. **97**: p. 157-167.

62. Glawdel, T. and C.L. Ren, *Droplet formation in microfluidic T-junction generators operating in the transitional regime. III. Dynamic surfactant effects.* Physical Review E - Statistical, Nonlinear, and Soft Matter Physics, 2012. **86**(2): p. 1-12.

63. Xu, J.H., et al., *The Dynamic Effects of Surfactants on Droplet Formation in Coaxial Microfluidic Devices.* Langmuir, 2012. **28**(25): p. 9250-9258.

64. Krägel, J. and S.R. Derkatch, *Interfacial shear rheology.* Current opinion in colloid & interface science, 2010. **15**(4): p. 246-255.

65. Martin, J.D., et al., *Interfacial rheology through microfluidics.* Advanced materials, 2011. **23**(3): p. 426-432.

66. Tomotika, S., *On the instability of a cylindrical thread of a viscous liquid surrounded by another viscous fluid.* Proceedings of the Royal Society of London. Series A - Mathematical and Physical Sciences, 1935. **150**(870): p. 322-337.

67. Vu, T.V., et al., *Computations of breakup modes in laminar compound liquid jets in a coflowing fluid.* International Journal of Multiphase Flow, 2013. **49**: p. 58-69.

68. Herrada, M.A., et al., *Analysis of the dripping–jetting transition in compound capillary jets.* Journal of Fluid Mechanics, 2010. **649**: p. 523-536.

69. Chen, Y., L. Wu, and C. Zhang, *Emulsion droplet formation in coflowing liquid streams.* Physical Review E, 2013. **87**(1): p. 013002.

4

Chapter

PDMS microparticles produced in PDMS microchannels under the jetting regime for optimal optical suspensions*

*J. Carneiro, JBLM. Campos, JM. Miranda
PDMS microparticles produced in PDMS microchannels under the jetting regime for optimal optical suspensions, **Colloids and Surfaces A: Physicochemical and Engineering Aspects**, https://doi.org/10.1016/j.colsurfa.2019.123737.

4

PDMS microparticles produced in PDMS microchannels under the jetting regime for optimal optical suspensions

Abstract

This study reports the generation and characterization of polydimethylsiloxane (PDMS) microparticles. Droplets are produced in the jetting regime by hydrodynamic flow focusing technique in a PDMS square-section microchannel and afterwards thermally cured. Both the droplets and microparticles size distributions are characterized and compared. During the curing process, there is no appreciable shrinking of the droplets/microparticles. Droplets are generated with a maximum frequency of 1.3 kHz and their diameter ranges from 27 to 59 μm depending on the flow rate ratio. After the cure, the microparticles are chemically and optically characterized. The results show that the droplet generation method and the curing process are able to produce PDMS microparticles with low size, low dispersity and optimal optical properties for visualization and velocimetry experiments.

4.1 Introduction

Polymeric microparticles have, nowadays, a wide range of applications, such as in tissue engineering, drug-delivery and cell mimicking, among others [1-7]. Several techniques and procedures have been developed to obtain microparticles: emulsification, direct agitation and grinding of the polymer, liquid spraying and microfluidics [8-10]. Techniques based on microfluidics are able to generate highly monodispersed particles in the micrometer and nanometer size ranges [4, 10-13].

Different microfluidic devices have been developed to produce microparticles and, between them, T-junctions and Flow Focusing configurations are the ones that show better performance [14-16]. Microfluidic Flow Focusing Devices (MFFD) have the advantage of parallel generation of small size particles at higher frequencies [1, 10, 12, 17, 18].

In a MFFD, a carrier phase (continuous phase) squeezes a dispersed phase through a common outlet and promotes, by fluid instabilities, the break of the dispersed phase into droplets, Figure 4.1 [19]. Subsequently, or in parallel, the droplets are cured to obtain particles.

The droplet formation in MFFD is done, preferably, in two flow regimes: jetting and dripping [10, 20]. To produce a large quantity of sub-channel size droplets, the jetting regime is the one that has the most advantages. The jetting regime is defined by a persistent thread which breaks far from the focusing section generating small droplets, Figure 4.1.

The size of the droplets formed depends on the fluids viscosity and density, surface tension, flow rates and geometry of the device. Performing dimensional analysis, the non-dimensional size of the droplets depends on the Capillary numbers of each phase and on the viscosity ratio [19, 20]. In alternative, followed in this work, one of the Capillary numbers can be replaced by the flow rate ratio.

The Capillary number, for a given phase *i*, measures the importance of viscous and capillary forces and is defined as:

$$\mathrm{Ca}_i = \frac{\mu_i v_i}{\sigma} \tag{4.1}$$

where μ_i is the viscosity of phase i, v_i the velocity of phase i and σ the interfacial tension.

The inversed flow rates ratio is defined as:

$$\varphi^* = \frac{Q_\mathrm{c}}{Q_\mathrm{d}} \tag{4.2}$$

where Q_d is the flow rate of the dispersed phase and Q_c of the continuous phase.

The viscosity ratio is defined as:

$$\chi = \frac{\mu_\mathrm{d}}{\mu_\mathrm{c}} \tag{4.3}$$

where μ_d is the viscosity of the dispersed phase and μ_c of the continuous phase.

PDMS is a transparent inert elastomer with unique properties, such as optical clarity, adjustable mechanical properties, gas permeability and biological compatibility. Furthermore, PDMS particles have others applications ranging from oxygen sensors to biomimetic fluids [19, 21-25].

PDMS droplet generation in PDMS microchannels is very challenging owing to the affinity between droplets and channel walls [19, 25]. The channels have to be chemically modified to avoid PDMS droplets from adhering to the channel walls and do not affect the particle production rate.

In most of the studies done, droplets in the range of 50-200 µm were generated in the dripping regime [19, 22, 23, 25]. To operate in this regime, the capillary number of the dispersed phase must be smaller than 0.1 [10, 19, 20, 25]. However, since PDMS viscosity is high (above 600 Pa s), to operate in the dripping regime, the flow rate of the dispersed phase must be low while the width of the microchannel cannot be too small. Therefore, the jetting regime becomes attractive to produce microparticles of

PDMS or any other polymer obtained from a high viscosity precursor. In the jetting regime, not only it is possible to obtain sub-channel sized particles, but it is also possible to operate at higher flow rate throughputs.

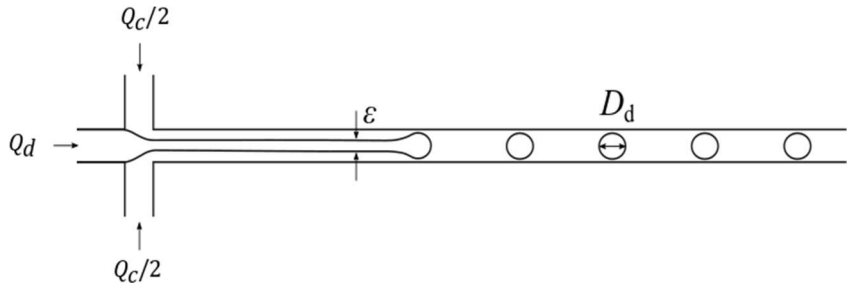

Figure 4.1. Schematic representation of the jetting regime in a simple flow-focusing geometry where ε is the thread diameter, D_d the droplet diameter, Q_d and Q_c are the flow rate of the dispersed and continuous phase, respectively.

Polydimethylsiloxane (PDMS) particles are very attractive to make suspensions to be handled in experiments involving visualization and velocimetry techniques. In visualization and velocimetry experiments of concentrated particulate suspension flows, the suspended particles must have a refractive index matching that of the solvent. Otherwise, the signal of the small (about 1μm) concentration fluorescent tracer particles seeded into the suspension to emit light at a given wavelength would be blocked and blurred hindering the experiments.

The objective of this work is to find the best flow conditions to produce in the jetting regime monodispersed sub-channel sized PDMS microdroplets (lower than 50 μm) with optical characteristics suitable to be applied in visualization and velocimetry experiments.

After the formation, the droplets in PDMS will be cured by heat to form microparticles and both the droplet and microparticle size distributions will be characterized and compared. Optical tests will be performed in order to analyse the refractive index of the microparticles and compared with that of the PDMS channels.

Although other works successfully produced PDMS microparticles with diameters bellow 10 μm, the microparticles were not produced in microchannels (limiting the parallelization potential) and shrinkage was observed [21, 26].

4.2 Experimental techniques and procedures

4.2.1 Microfluidic device fabrication

The Microfluidic Flow Focusing Device (MFFD), Figure 4.1, consists of three inlets channels, one for the dispersed phase and two for the continuous phase, and one outlet channel. All these channels intersect at right angles and have identical dimensions (100 μm in depth). The MFFDs were fabricated by soft lithography [25] using a 5:1 base PDMS to curing agent ratio for the channel, and a 20:1 base to curing agent ratio for the thin layer, ~ 30 μm, of PDMS spin-coated over a glass slide. The Dow Corning Sylgard® 184 kit was used [25]. This procedure ensures that all the MFFD walls material have the same wetting proprieties.

PDMS mold and coated glass slide were cured, in an oven, at 80 ºC for 20 minutes. Afterwards, the cured PDMS was sealed to the glass-coated slide and left to cure for approximately 12 hours at 80 ºC [25]. Before each experiment, air plasma surface-treatment was applied to the PDMS surface in a low pressure Plasma Reactor (Diener® electronic GMbH, model ZEPTO), for 3 min at 30 watts, to render the surface hydrophilic [25].

4.2.2 Microfluidic droplet generation and curing process

The continuous phase was an aqueous solution of glycerol (85 % w/w) with 0.4 % w/w of Sodium Dodecyl Sulfate (SDS), ($\mu_c = 0.0111$ Pa. s , $\rho_c = 1222$ kg m^{-3}). The dispersed phase was liquid PDMS pre-polymer with a 6:4 base to curing agent ratio (Corning Sylgard® 184 kit), ($\mu_d = 0.640$ Pa. s, $\rho_d = 1001$ kg m^{-3}). The viscosity of both phases was characterized using a rotational rheometer (Physica MCR301, Anton Paar) with a Peltier temperature control system set at 20 ºC. An interfacial tension between phases of $\sigma = 13.8$ mN m^{-1} was measured at ~ 20 ºC in a DuNuoy ring tensiometer.

Using a dedicated syringe pump, the dispersed and continuous phases were injected into the microchannel, Figure 4.2. Droplets were generated for 2 hours and collected

by a 5 mL pipette tip, Figure 4.2. The flow conditions set for the droplet generation are represented in Table 4.1. Afterwards, the droplets were transferred to a 5 mL pycnometer and were cured in the oven at 80 ºC for 40 min, Figure 4.2. The first attempt to cure particles was done with 20 mL goblets, but fusing of particles at the air / suspension interface was observed. For this reason, the pycnometer was chosen to cure the particles since the capillary minimizes the size of the air/liquid interface. Microparticles were then filtered, through an acetate cellulose filter - 0.2 µm pore - and washed with distilled water. Afterwards, they were stored in protected glass slides for future use.

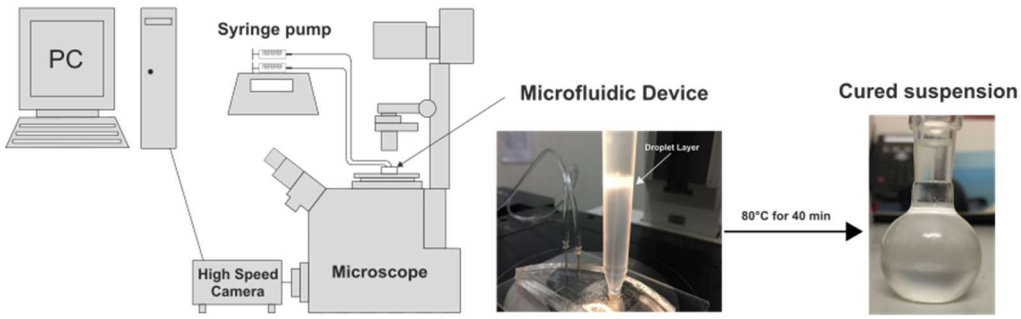

Figure 4.2. Experimental setup, microchannel flow focusing droplet generation and curing process.

Table 4.1. Flow conditions for the droplet generation.

φ^*	Q_d (µl min^{-1})	Q_c (µl min^{-1})	Ca_d	Ca_c
10	1	10	7.73×10^{-2}	1.34×10^{-1}
20	1	20	7.73×10^{-2}	2.68×10^{-1}
40	1	40	7.73×10^{-2}	5.36×10^{-1}
70	1	70	7.73×10^{-2}	9.38×10^{-1}
10	0.5	5	3.86×10^{-2}	6.70×10^{-2}
20	0.5	10	3.86×10^{-2}	1.34×10^{-1}
40	0.5	20	3.86×10^{-2}	2.68×10^{-1}
70	0.5	35	3.86×10^{-2}	4.69×10^{-1}

4.2.3 Droplets and microparticles size characterization

Droplet formation images were captured via a high-speed camera (FASTCAM Mini UX100, Photron), at a maximum rate of 20 000 frames per second and exposure time of 0.05 ms, mounted on an inverted epifluorescence microscope (DMI 5000M, Leica Microsystems GmbH), Figure 4.2. For optimal lighting conditions, a 10x objective (1 µm/pixel) was used to measure the newly generated droplets at the channel's outlet. The post-processing of the images and droplets diameter measurement was performed using a Droplet Morphometry and Velocimetry (DMV) software [27] with an average error of ~ 3 % for the droplet diameter. After the curing process, the microparticles were placed in glass slides and images were captured with a 20x (0.5 µm/pixel) and 40x objectives (0.25 µm/pixel) and the diameters were measured again using the software of the high-speed camera, Photron FASTCAM Viewer, with an average error of ~ 4 %. Microparticles with diameters bellow 2 µm were not taken into account due to the high measurement error, ~ 13 % for a 40x objective (0.25 µm/pixel).

4.2.4 Chemical characterizations of the microparticles

The PDMS microparticles and microchannel surface were sputtered with gold (Au) and was chemically analyzed by Scanning Electron Microscope (SEM), equipped with energy-dispersive X-ray spectroscopy.

4.2.5 Optical characterizations of the microparticles

The optical test consisted on the match of the refracting index of the PDMS microparticles with that of a 52 % Dimethyl sulfoxide (DMSO) aqueous solution (w/w) poured into the microparticles sample. The refractive indexes of both, PDMS and DMSO aqueous solution, were previously measured and are coincident, 1.4125. As a negative control test, water was also added to another sample.

4.3 Results and Discussion

The results and discussion are divided into four main sections:

- Characterization of the liquid droplet formation in the microfluidic device (section 4.3.1);
- Characterization and comparison between the liquid droplets and cured solid particles populations (section 4.3.2);
- Characterization of the chemical properties of the microparticles (section 4.3.3);
- Characterization of the optical properties of the microparticles (section 4.3.4).

4.3.1 Droplet size characterization

Droplets are generated in a Microfluidic Flow Focusing Device (MFFD) in the jetting regime; Figure 4.3 illustrates an example of the dynamics of the droplets formation.

In the jetting regime, the thread of the dispersed phase extends into the outlet channel until it breaks down giving rise to spherical droplets. The breaking mechanism that leads to the formation of the droplets, as well as the size of the microdroplets formed, is governed, in large extent, by the flow rate of the continuous phase, Q_{c} [13].

In order to study the flow rate ratio effect on the droplet diameter, the average dimensionless droplets diameter, $\frac{\overline{D}_d}{h}$ (h is the channel characteristic dimension), is plotted versus the flow rates ratio, $\varphi^* = Q_{\mathrm{c}}/Q_{\mathrm{d}}$, in Figure 4.4 for a viscosity ratio between phases of 6. Two different dispersed phase flow rates were studied, $Q_{\mathrm{d}} = 0.5 \text{ and } 1\ \mu\mathrm{L/min}$, to support the conclusions. According to the plot two main conclusions can be extracted:

1 – for each flow rate ratio, $\frac{\overline{D}_d}{h}$ is independent of the flow rate of the dispersed phase, as expected;

2- for a given flow rate of the dispersed phase, $\frac{\overline{D}_d}{h}$ decreases with increasing values of the continuous flow rate.

Another variable that has an effect on $\frac{\overline{D}_d}{h}$ is the viscosity ratio, χ . Cubaud and Mason [20] studied the droplet formation in high viscosity ratio systems, $24 \leq \chi \leq 1480$, while Fu *et al.* [28] in low viscosity systems, $1 \leq \chi \leq 12$. The droplet sizes in the present study for $\chi = 6$, as can be seen in Figure 4.4, are located near those of Fu *et al.* [28] and are smaller than those obtained for $\chi = 533$ and $\chi = 337$ by Carneiro et al. [19] with a water/PDMS system.

Another important parameter, in the jetting regime, is the so called mode of maximum instability [29], which is given by the ratio between the primary droplet diameter and the jet diameter, $\overline{D}_d/\varepsilon$. According to the works of Fu *et al.*Fu, Wu [28], Tomotika [29] and Cubaud and Mason [20] this ratio only depends on the viscosity ratio. In this work, $D_d/\varepsilon \approx 2.42$ for $\chi = 6$, which coincides with that of Fu *et al.* Fu, Wu [28], for the same viscosity ratio.

During the formation of each primary droplet, a much smaller satellite droplet is generated, Figure 4.3. These satellite droplets were excluded from droplet and particle characterization. Although satellite droplets account for 50 % of the droplet population, their volume only represents a maximum of ~ 2 % of the total volume of droplets. Their average diameter, $\overline{D}_{ds}$, ranges from 13 μm to 6 μm for the lowest and highest continuous flow rates respectively, following the same trend as $\overline{D}_d$, Figure 4.4(inset).

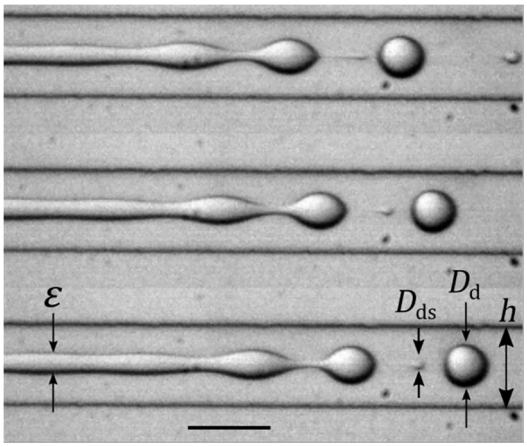

Figure 4.3. Droplet formation in the jetting regime. Flow condition: flow condition Q_d = 1 and Q_c = 10 µL min^{-1}. Time interval between frames: 0.05 ms. Scale bar: 100 µm.

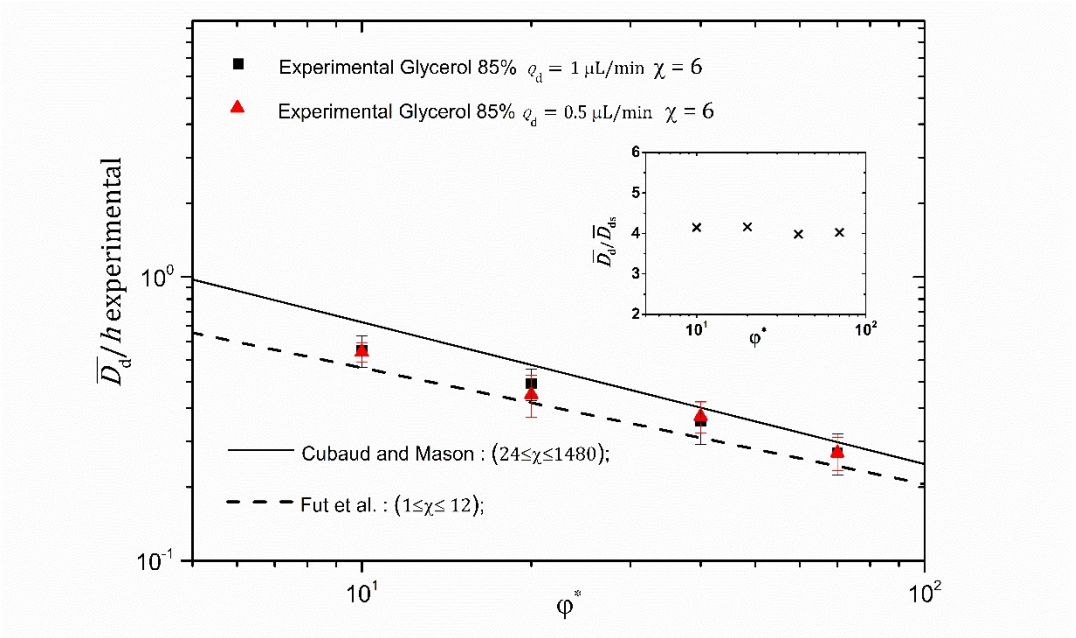

Figure 4.4. Experimental average dimensionless droplet diameter, $\frac{\overline{D}_d}{h}$, vs the ratio between the continuous and dispersed phase flow rate, $\varphi^* = Q_c/Q_d$, for two different dispersed flow rates, Q_d = 0.5 and Q_d = 1 µL min^{-1}. Cubaud and Manson (2008) , $24 \leq \chi \leq 1480$, and Fu et al (2012) , $1 \leq \chi \leq 12$, correlations for the droplet diameter in the jetting regime are also represented. The error bars represent the standard deviation. Inset: Ratio between droplet and satellite droplet diameters, $\overline{D}_d/\overline{D}_{ds}$, vs the ratio between the continuous and dispersed phase flow rate, φ^*.

Another significant output of the present study is the droplet generation frequency, f_{exp}, given by:

$$f_{exp} = \frac{nº droplets}{\Delta t} \ (Hz) \tag{4.4}$$

In Figure 4.5, f_{exp} is plotted in function of the flow rate ratio, φ*, for two flow rates of the dispersed phase, Q_d = 0.5 and Q_d = 1 µL min^{-1}. As φ* increases f_{exp} increases in a linear way for both Q_d; the highest Q_d (1 µL min^{-1}) produces more droplets. A maximum of 1300 Hz was obtained for 1 µL min^{-1}.

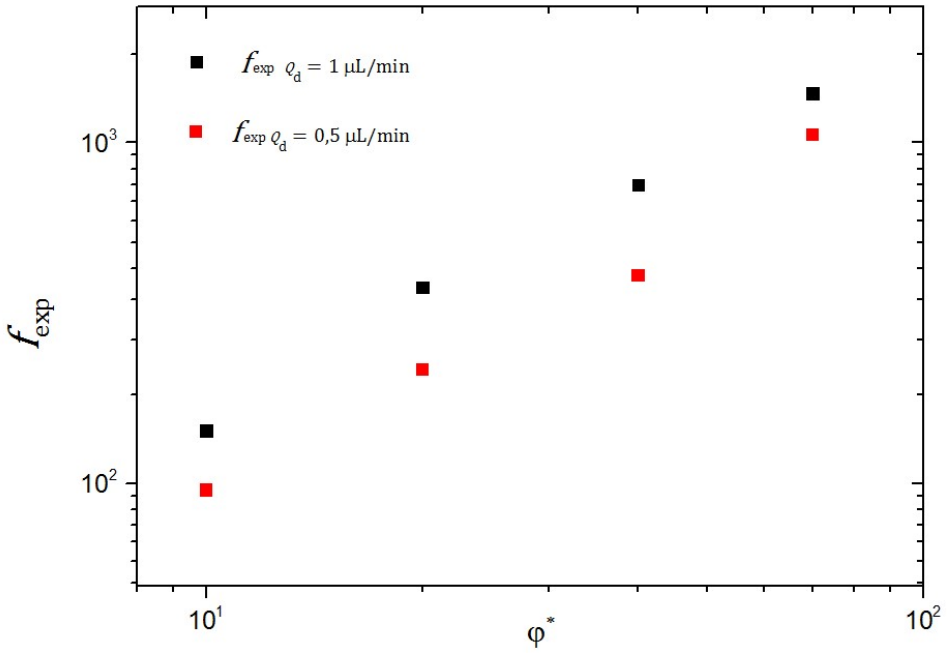

Figure 4.5. Experimental droplet generation frequency, f_{exp} , vs the ratio between the continuous and dispersed phase flow rate, $\varphi^* = Q_c/Q_d$, for for two different dispersed flow rates, Q_d= 0.5 and Q_d = 1 µL min^{-1}.

In Figure 4.6 the droplet diameter distribution is represented for Q_d = 1 µL min^{-1} for all Q_c. The average diameter of the droplets, $\overline{D}_d$, and the coefficient of variance (CV) are also represented: $\overline{D}_d$ ranges from ~27 µm to ~ 59 µm from the highest to the lowest Q_c, while CV ranges from ~ 12 % to ~ 16 %, which can be considered a relatively low value. For a better characterization, Normal and Log-Normal

distributions are also represented in Figure 4.6. With the exception of the distribution for the lowest Q_c, Figure 4.6a, all the others are well represented by a Log-Normal curve. For the lowest Q_c, a large percentage of the population is within a very short size range, ~ 60 % between 52.5 and 55.5 µm, and by consequence, its CV is the lowest with ~ 12 %.

The jetting regime is a flow regime inherently unstable and leads necessarily to polydispersed particles. The coefficients of variance obtained in the present work are relatively small when compared to those obtained previously [19] for a higher viscosity ratio ($\chi = 533$) suggesting that decreasing the viscosity ratio reduces the particle size polydispersity.

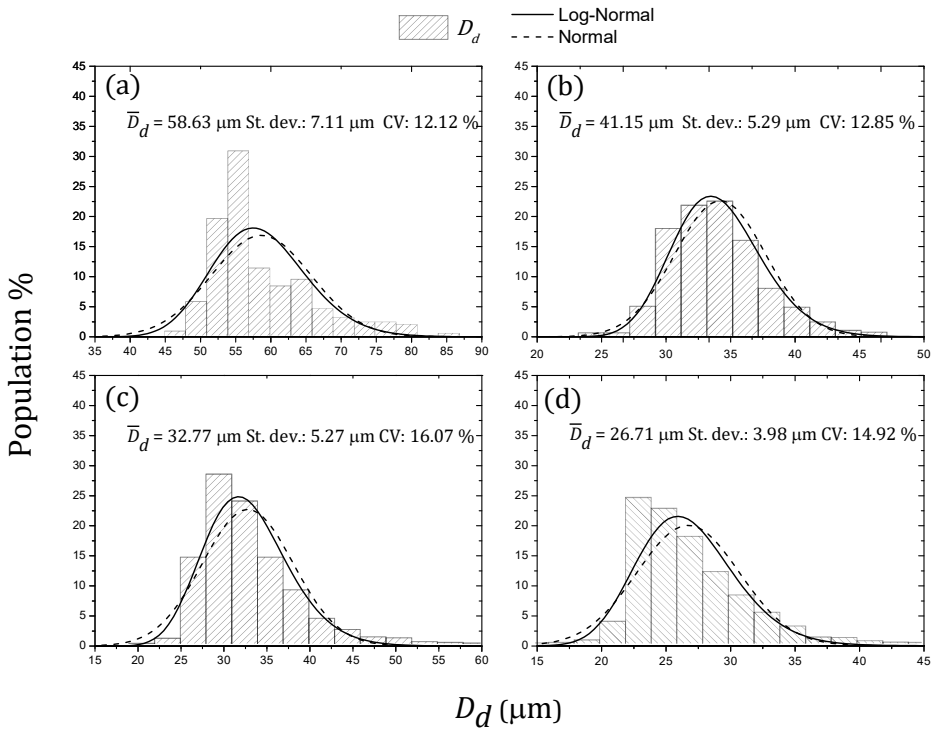

Figure 4.6. Probability distribution for the droplet diameter (dashed bars), D_d, produced for the different flow conditions: (a) $Q_d = 1$ and $Q_c = 10$; (b) $Q_d = 1$ and $Q_c = 200$; (c) $Q_d = 1$ and $Q_c = 40$; (c) $Q_d = 1$ and $Q_c = 70$ (both in µL min-1). Log-Normal (line) and Normal curves (dash line) curves for all flow conditions.

4.3.2 Microparticle characterization

The size distributions of the droplets and of the, subsequent, cured microparticles were compared in order to study any change in size during the curing process, Figure 4.7. The sizes of at least 200 droplets and 200 microparticles, were measured for each flow condition. The average diameters, over multiple experiments, of droplets and microparticles, $\overline{D}_d$ and $\overline{D}_p$ respectively, as well as the respective coefficients of variance (CV), were calculated.

The distributions are plotted in Figure 4.7 and, for all flow conditions, they are very similar. Also, the average diameters and the coefficients of variance are almost the same. The variations are within the error of the measurement procedure.

Although other works, [21, 26], report a pronounced shrinkage of particles during the PDMS curing, in the present work no significant change of size was observed. The use of Brij® L4 as surfactant may explain the significant shrinkage observed in previous works. Further investigation is necessary to clarify this issue.

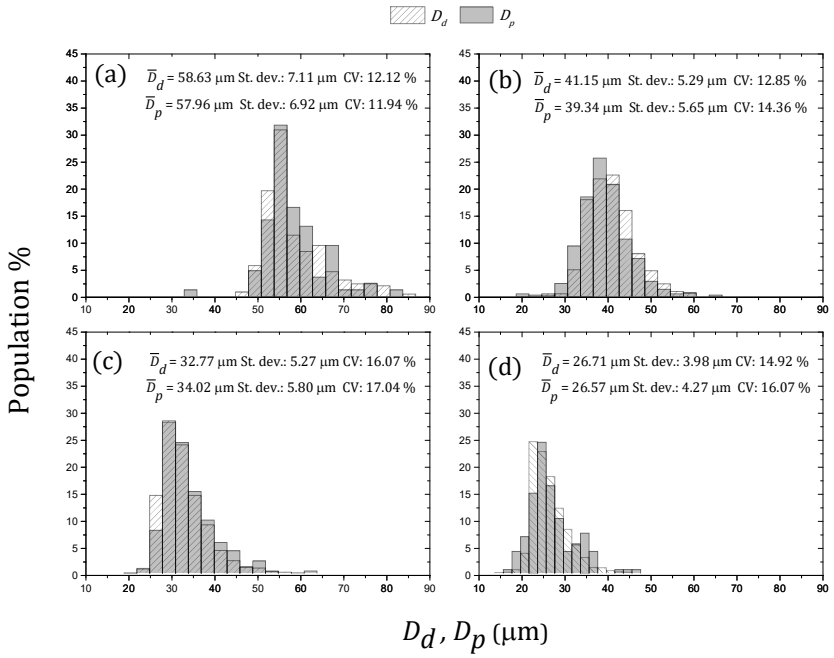

Figure 4.7. Probability distribution for the droplet (dashed bars), D_d , and microparticles (grey bars), D_p, diameters produced for the different flow conditions: (a) Q_{d}= 1 and Q_{c} = 10; (b) Q_{d}= 1 and Q_{c} = 20; (c) Q_{d}= 1 and Q_{c} = 40(c) Q_{d}= 1 and Q_{c} = 70 (both µL min^{-1}).

4.3.3 Chemical characterization of the particles

In order to verify the purity of the PDMS microparticles, a qualitative composition analysis by SEM - Energy Dispersive X-ray spectroscopy (EDS) was performed. The composition of the wall (PDMS) of the channels where microdoplets were formed was also analysed, Figure 4.8. As stated in the Methods section the microparticles and the microchannels had different base to curing agent ratios: 5:1 for the microchannel and 6:4 for the microparticles.

Besides gold (Au), the conductive element used in SEM, only carbon (C), oxygen (O) and silicon (Si) elements are present in both cases, Figure 4.9. Carbon and oxygen are in lower percentages in the PDMS of the wall.

The EDS results are in agreement with the composition of cured PDMS referred in the literature and no contaminants were found [30]. Contaminated samples (not subjected to the washing step) were also analysed and higher peaks of sodium (Na) and sulfur (S) were present in the samples suggesting SDS contamination.

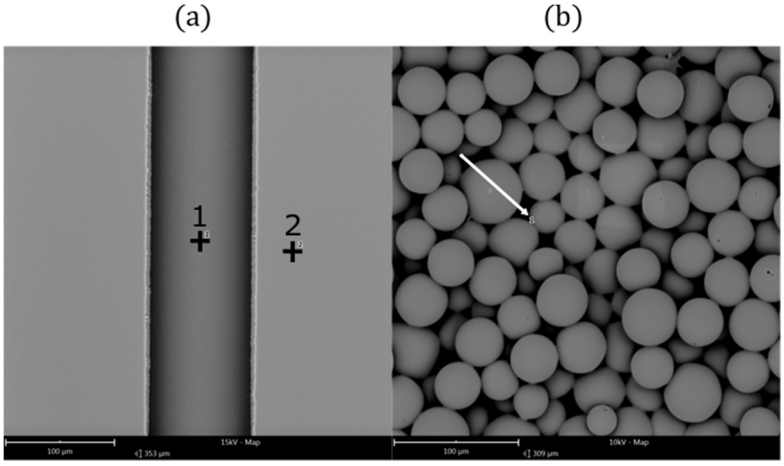

Figure 4.8. SEM images: (a) outlet of the microchannel used to generate the droplets with a EDS spot pointing for the channel top wall and for a region outside the channel, Spot 1 and 2 respectively; (b) linescan of a microparticle (flow condition: Q_d = 1 and Q_c = 20 µL min^{-1})

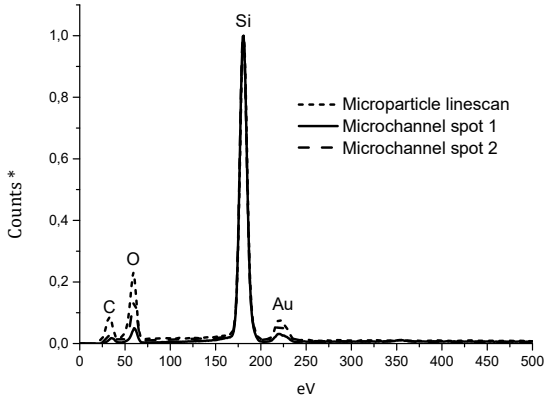

Figure 4.9. EDS profile for the microparticle linescan and microchannel spot 1 and 2. The counts are normalized by the highest peak.

4.3.4 Optical characterization

When the refractive index of the microparticles matches PDMS refractive index, the particles are optically compliant with PDMS and can be used in visualization or velocimetry experiments.

In order to verify if the refractive of the microparticles matches that of the PDMS, two different fluids were added to dried microparticle samples: one with the expected refractive index of the PDMS (52 % Dimethyl sulfoxide (DMSO) aqueous solution (w/w), Figure 4.10.1, and another with a different refractive index, distilled water, Figure 4.10.2 [30].

When DMSO solution is added, the microparticles start to become invisible, as expected, Figure 4.10b1. When they are completely submerged all of them become invisible and only some contaminants from storage can be seen, Figure 4.10c1. When distilled water is added, Figure 4.10b2, the microparticles are always visible, as was predictable since the refractive index of the water (1.3325) is different from that of the PDMS. The results confirm the reliability of the method of producing clean PDMS microparticles and the potential of the PMDS microparticles to produce transparent particulate fluids.

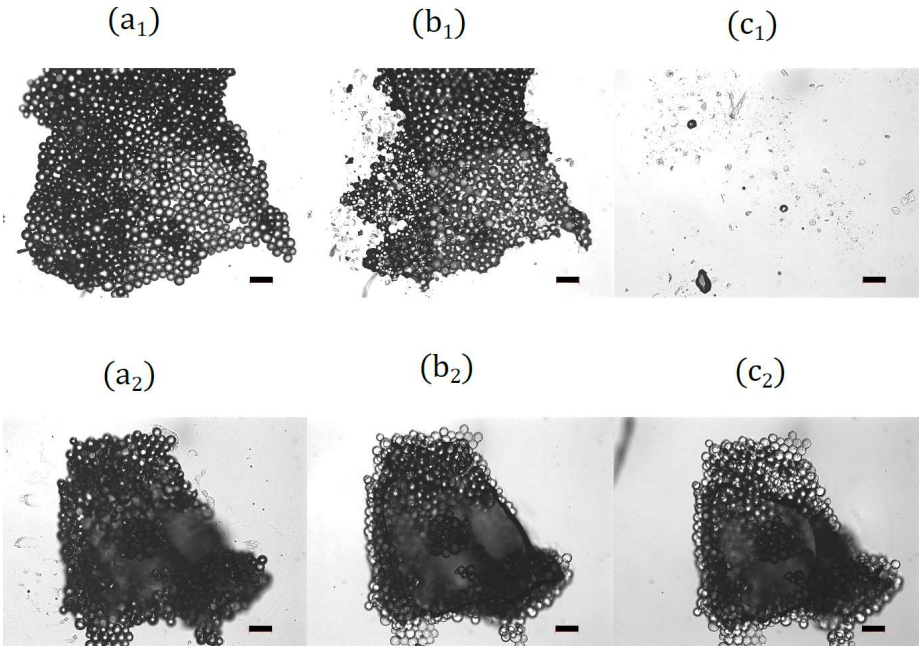

Figure 4.10. Refractive index test: (a) 52 % DMSO and water (w/w) and (b) distilled water. Microparticles generated with the flow condition $Q_d = 1$ and $Q_c = 20$ µL min^{-1}. Scale bar: 100µm.

4.4 Conclusion

In this work, PDMS microparticles were successfully produced in PDMS microchannels with a simple square-section. They are generated in the jetting regime with a diameter ranging from ~ 27 to 59 µm. Droplets size can be easily controlled by tuning the flow rate ratio. For each flow rate ratio, the size dispersion of the droplets is relatively low with a maximum CV of ~ 17 %. During the cure, it was not observed any shrinkage of the microparticles.

SEM analysis and optical refraction index tests showed that the PDMS microparticles produced with the proposed method are contaminant free and optically compliant with the PDMS of the microchannels and so they can be used in visualization and velocimetry techniques.

By operating in the jetting regime, it is possible to produce thousands of particles per second in a single channel, which is a significant improvement by comparison to

the dripping regime. The amount is still insufficient for practical applications, but that can be mitigated with the parallelization of the droplet generation.

Acknowledgements

This work was funded by FEDER funds through COMPETE2020—Operational Programme for Competitiveness Factors (POCI) and National Funds (PIDDAC) through FCT (Fundação para a Ciência e a Tecnologia) under projects PEst-OE/EME/UI0532, POCI-01-0145-FEDER-016861-PTDC/QEQ-FTT/4287/2014 and PD/BD/114313/2016. J.Carneiro wants to thank Ali Emami for the SEM analysis.

Notation

Latin	Definition	Units
CV	Coefficient of variance	(%)
D_d	Droplet diameter	(µm)
$\overline{D}_d$	Average droplet diameter	(m)
$\overline{D}_{ds}$	Average satellite droplet diameter	(µm)
D_p	Microparticle diameter	(µm)
$\overline{D}_p$	Average microparticle diameter	(µm)
f_{exp}	Experimental droplet generation frequency	(Hz)
h	Channel characteristic dimension	(m)
Q_{c}	Volumetric flow rate of the continuous phase	(m^3 s^{-1})
Q_{d}	Volumetric flow rate of the dispersed phase	(m^3 s^{-1})
v	Velocity	(m s^{-1})

Greek	Definition	Units
Δt	Time interval	(s)
ε	Thread diameter	(m)
μ_{c}	Dynamic viscosity of the continuous phase	(Pa s)
μ_{d}	Dynamic viscosity of the dispersed phase	(Pa s)
ρ_{c}	Density of continuous phase	(kg m^{-3})
ρ_{d}	Density of dispersed phase	(kg m^{-3})
σ	Interfacial tension	(N m^{-1})

φ^*	Inversed of the ratio of the volumetric flow rates	---
χ	Viscosity ratio	---

Dimensionless numbers	**Definition**
Ca	Capillary number
Ca_c	Capillary number of the continuous phase
Ca_d	Capillary number of the dispersed phase

Acronyms	**Definition**
DMSO	Dimethyl sulfoxide
EDS	Energy dispersive X-ray spectroscopy
MFFD	Microfluidic Flow Focusing Device
PDMS	Polydimethylsiloxane
SEM	Scanning slectron microscope
SDS	Sodium dodecyl sulfate

References

1. Lagus, T.P. and J.F. Edd, *A review of the theory, methods and recent applications of high-throughput single-cell droplet microfluidics.* Journal of Physics D: Applied Physics, 2013. **46**(11): p. 114005-114005.
2. Teh, S.-Y., et al., *Droplet microfluidics.* Lab on a Chip, 2008. **8**(2): p. 198-198.
3. Champion, J.A., Y.K. Katare, and S. Mitragotri, *Particle shape: A new design parameter for micro- and nanoscale drug delivery carriers.* Journal of Controlled Release, 2007. **121**(1-2): p. 3-9.
4. Xu, Q., et al., *Preparation of Monodisperse Biodegradable Polymer Microparticles Using a Microfluidic Flow-Focusing Device for Controlled Drug Delivery.* Small, 2009. **5**(13): p. 1575-1581.
5. Day, P., A. Manz, and Y. Zhang, *Microdroplet Technology*. 2012. 249-249.
6. Nunes, J.K., et al., *Dripping and jetting in microfluidic multiphase flows applied to particle and fibre synthesis.* Journal of Physics D: Applied Physics, 2013. **46**(11): p. 114002-114002.
7. Wan, J., *Microfluidic-based synthesis of hydrogel particles for cell microencapsulation and cell-based drug delivery.* Polymers, 2012. **4**(2): p. 1084-1108.
8. Oh, J.K., et al., *The development of microgels/nanogels for drug delivery applications.* Progress in Polymer Science, 2008. **33**(4): p. 448-477.
9. Oliveira, M.B. and J.F. Mano, *Polymer-based microparticles in tissue engineering and regenerative medicine.* Biotechnology Progress, 2011. **27**(4): p. 897-912.
10. Anna, S.L., *Droplets and Bubbles in Microfluidic Devices.* Annual Review of Fluid Mechanics, 2016. **48**(1): p. 285-309.
11. Anna, S.L. and H.C. Mayer, *Microscale tipstreaming in a microfluidic flow focusing device.* Physics of Fluids, 2006. **18**(12).
12. Zhu, P. and L. Wang, *Passive and active droplet generation with microfluidics: a review.* Lab Chip, 2017. **17**(1): p. 34-75.
13. Utada, A.S., et al., *Dripping to Jetting Transitions in Coflowing Liquid Streams.* Physical Review Letters, 2007. **99**(9): p. 094502-094502.
14. Yang, L., et al., *Visualization and characterization of gas-liquid mass transfer around a Taylor bubble right after the formation stage in microreactors.* Chemical Engineering Science, 2016. **143**: p. 364-368.
15. Garstecki, P., et al., *Formation of droplets and bubbles in a microfluidic T-junction—scaling and mechanism of break-up.* Lab on a Chip, 2006. **6**(3): p. 437-437.

16. Anna, S.L., N. Bontoux, and H.A. Stone, *Formation of dispersions using "flow focusing" in microchannels.* Applied Physics Letters, 2003. **82**(3): p. 364-366.

17. Baroud, C.N., et al., *Dynamics of microfluidic droplets.* Lab on a Chip, 2010. **10**(16): p. 2032-2032.

18. Seemann, R., et al., *Droplet based microfluidics.* Reports on Progress in Physics, 2012. **75**(1): p. 016601-016601.

19. Carneiro, J., J.B.L.M. Campos, and J.M. Miranda, *High viscosity polymeric fluid droplet formation in a flow focusing microfluidic device – Experimental and numerical study.* Chemical Engineering Science, 2019. **195**: p. 442-454.

20. Cubaud, T. and T.G. Mason, *Capillary threads and viscous droplets in square microchannels.* Physics of Fluids, 2008. **20**(5): p. 1-11.

21. Muñoz-Sánchez, B.N., et al., *Generation of micro-sized PDMS particles by a flow focusing technique for biomicrofluidics applications.* Biomicrofluidics, 2016. **10**(1): p. 1-11.

22. Di Benedetto, F., et al., *Rolling particle lithography by soft polymer microparticles.* Soft Matter, 2013. **9**(7): p. 2206-2206.

23. Jiang, K., et al., *Microfluidic synthesis of monodisperse PDMS microbeads as discrete oxygen sensors.* Soft Matter, 2012. **8**(4): p. 923-926.

24. Zhao, L.-B., et al., *A novel method for generation of amphiphilic PDMS particles by selective modification.* Microfluidics and Nanofluidics, 2011. **10**(2): p. 453-458.

25. Carneiro, J., et al., *PDMS droplet formation and characterization by hydrodynamic flow focusing technique in a PDMS square microchannel.* Journal of Micromechanics and Microengineering, 2016. **26**(10): p. 105013.

26. Anes, C.F., et al., *Shrinkage and colour in the production of micro-sized PDMS particles for microfluidic applications.* Journal of Micromechanics and Microengineering, 2018. **28**(7): p. 075002.

27. Basu, A.S., *Droplet morphometry and velocimetry (DMV): a video processing software for time-resolved, label-free tracking of droplet parameters.* Lab on a Chip, 2013. **13**(10): p. 1892-1901.

28. Fu, T., et al., *Droplet formation and breakup dynamics in microfluidic flow-focusing devices: From dripping to jetting.* Chemical Engineering Science, 2012. **84**: p. 207-217.

29. Tomotika, S., *On the instability of a cylindrical thread of a viscous liquid surrounded by another viscous fluid.* Proceedings of the Royal Society of London. Series A - Mathematical and Physical Sciences, 1935. **150**(870): p. 322-337.

30. Doutel, E., et al., *Experimental and numerical methodology to analyze flows in a coronary bifurcation.* European Journal of Mechanics - B/Fluids, 2018. **67**: p. 341-356.

5

Chapter

Microparticle blood analogue suspensions covering a wide hematocrit range*

* J. Carneiro, J.B.L.M. Campos, J. M. Miranda
Microparticle blood analogue suspensions covering a wide hematocrit range, **Soft Matter**, October 2019, under review.

5

Microparticle blood analogue suspensions covering a wide hematocrit range

Abstract

The handling of blood *in vitro* is demanding because of ethical, economical and safety issues. Although several Newtonian and non-Newtonian blood analogues are found in the literature, few studies use particles to mimic red blood cells (RBCs) and built an analogue with similar rheological properties of blood. This work reports the development of a blood analogue suspension composed of polydimethylsiloxane (PDMS) microparticles with an average diameter of ~ 7 μm. A high throughput production of PDMS particles is possible using a multi-stage membrane emulsification process; up to ~ 6 mL of microparticles are manufactured in 3 hours. A concentration of PDMS particles around 21 % (w/w), presents a steady-state and extensional rheology very similar to blood, making it a good candidate for a whole blood analogue. Using the procedure developed it is possible to obtain blood analogue fluids that mimic a wide haematocrit range, up to 45 %, the typical physiological condition. Also, flow studies were performed in microchannels with a contraction to study the cell-free layer (CFL) formation and good qualitative results were achieved.

5.1 Introduction

Blood is a complex physiological fluid which, in a simplistic way, consists of blood cells suspended in liquid plasma. Red blood cells (RBCs) are the most abundant type of cells in whole blood with an average concentration of 45 % [1, 2]. Since RBCs are the most abundant particulate matter, the rheological behaviour of whole blood is generally determined by their presence. Blood exhibits a non–Newtonian shear–thinning behavior, which is the result of aggregation/disaggregation and deformation of RBCs [2-7]. At low shear rates, RBCs form agglomerates known as *rouleaux* which are reversely teared at high shear rates [8].

When whole blood flows in microvessels with diameters less than about 300 μm [9-13] another important phenomenon is the cell-free layer (CFL) formation. Interactions between RBCs and vessel walls usually induce the formation of a plasma layer with reduced hematocrit alongside the vessel walls, and increased concentration of RBCs near the center of the vessel [9-13]. The decrease of the intravascular hematocrit, 50 – 80 %, (Fahraeus effect [11, 14, 15]) has significant consequences on the blood flow behavior in narrow vessels, namely a lower resistance of the vessels to blood flow (Fahraeus-Lindqvist effect [11]).

Although several studies were made concerning the rheological behavior of whole blood [4, 16-21], the use of *in vivo* blood samples to study its flow dynamics is frequently unsuitable due to the cost, safety and ethical issues involved. Therefore, *in vitro* studies with blood analogue fluids are the most adequate alternative [1, 22]. The blood analogues referred in the literature are either Newtonian, water/glycerol and water/DMSO mixtures, or non-Newtonian polymeric aqueous solutions based on Xantham gum, polyacrylamide and hyaluronic acid [5, 23]. However, these solutions don't have the microstructure of blood and cannot be used to mimic blood flow at the microscale. Recent experimental works indicate particulate blood analogue fluids to mimic the flow characteristics of healthy and pathological RBCs [24-26]. Two of the main drawbacks of these analogues are the use of a more viscous and elastic base fluid compared to plasma, Dextran 40 (Dx40), and the low throughput of particle production by current methods. The low amount of particles produced usually hinder the production of blood analogue fluids that mimic blood with hematocrit typical of physiological conditions (45 %).

The main objective of this work is to develop an analogue fluid able to mimic, in all its extension, the blood rheological properties. The proposed analogue is composed of polydimethylsiloxane (PDMS) microparticles, produced through membrane emulsification, suspended in an aqueous solution of 4 % SDS (w/w). PDMS, when cured, is an elastic material with good optical access. A membrane with a pore of 10 μm was used to produce PDMS particles with an average diameter of ~ 7 μm, close to the size of human RBCs, 6-8 μm [4]. The suspension concentration was adjusted to have steady-shear and elastic rheological proprieties similar to whole blood. The advantage of membrane emulsification over conventional microfluidic droplet production is a high throughput production of small droplet sizes [27], enabling the production of fluids with a wide range of PDMS concentrations able to cover a wide hematocrit range. The PDMS analogue suspension proposed in this work was characterized with steady-state and extensional rheology tests and the results compare well with whole blood properties. Also CFL thickness measurements were performed in a microchannel with a contraction.

5.2 Material and Methods

5.2.1 Suspension preparation

Fluids

The suspension was prepared with two immiscible fluids: the continuous phase ($\mu_c = 0.0014$ Pa s and $\rho_c = 1010$ kg m^{-3}) was water with a surfactant, Sodium Dodecyl Sulfate (SDS) 4 % w/w, while PDMS pre-polymer with a ratio of 6:4, base and curing agent respectively, ($\mu_d = 0.0640$ Pa s and $\rho_d = 1030$ kg m^{-3} Corning Sylgard® 184 kit) was the dispersed phase. The viscosity of each fluid was determined using a rotational rheometer (Physica MCR301, Anton Paar) with a Peltier temperature control system set to 20 ºC. The measurements were carried out using a 75 mm

diameter cone–plate geometry, CP75-1, with a gap of 0.041 mm. The interfacial tension, 12 $mN \cdot m^{-1}$, was measured at ~ 20 ºC in a DuNuoy ring tensiometer.

Vortex pre-emulsification

Suspensions of 20 mL with different concentrations of PDMS 6:4 pre-polymer and 4 % SDS aqueous solution were prepared in a 50 mL sterile cup (Deltalab). The mixture was promoted by a vortex mixer (VV3, VWR®) at its maximum output, ≈ 2500 rpm, for 10 min at room temperature, 22 ± 2 ºC, Figure 5.1a.

Membrane emulsification by syringe filters

The membrane emulsification was performed immediately after the vortex pre-emulsification, see Figure 5.1a. The mixture was poured into a 20 mL Luer lock plastic syringe (BD Plastipak ™) set out with an hydrophilic membrane, 10 µm pore size (Versapor® Acrodisc® Syringe Filter, PALL), see Figure 5.1b. A syringe pump (neMESYS CETONI GmbH), mounted vertically to minimize sedimentation effects of the PDMS droplets during the injection, was set at a constant filtration flow rate of ≈ 1800 $\mu L\ s^{-1}$. The filtration was repeated, successively, 3 times using new filters and syringes to avoid clogging.

After the membrane emulsification, the emulsion was poured into a glass container and cured in an oven at 80 °C for 2 hours. Even using new filters for each membrane emulsification, small amounts of PDMS are lost in the filters. To assess the final PDMS concentration, three samples from each concentration were dried at 80 ºC for 24 h and weighted. The results are presented in Table 5.1. On average, the final cured suspensions have ~ 25 % less PDMS than the initial solution. This process is capable of producing ~up to ~ 6 mL, of microparticles in 3 hours.

Droplet and microparticle sizes were measured by placing suspended droplets/particles samples in glass slides and images were captured with a 40x objective (0.25 µm/pixel) using the software of the high-speed camera, Photron FASTCAM Viewer. Diameters bellow 2 µm were not taken into account owing the high measurement error, ≥ 13 %.

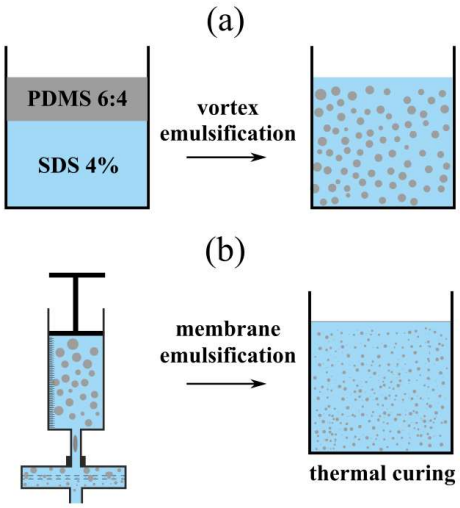

Figure 5.1. Suspension preparation procedure: vortex and membrane emulsification, (a) and (b) respectively. Final suspension was cured in an oven at 80 °C for 2 hours.

Table 5.1. Pre-emulsion concentrations of PDMS pre-polymer and dried concentrations of PDMS after the suspension preparation process.

Pre-emulsion PDMS concentration (%, w/w)	**Dried PDMS concentration** (%, w/w)
10	8 ± 1 %
20	17 ± 1 %
25	21 ± 1 %
30	24 ± 1 %
40	32 ± 2 %

5.2.2 Suspension rheology

Steady-state Shear rheology

To measure the steady-state shear rheology, the protocol implemented in Sousa *et al*. 2013 for whole blood samples was followed [28]. The measurements were carried out in a rotational rheometer (Physica MCR301, Anton Paar) with a Peltier temperature control system. A 50 mm diameter serrated plate–plate geometry, PP50/P2, with a 1 mm gap was used. The temperature was set to 20 °C.

Extensional rheology

Measurements of the suspension filament thinning dynamics were carried out using the plate separation drive unit of a Haake CaBER-1 extensional rheometer (Thermo Haake GmbH, Karlsruhe, Germany) in order to control the position and separation velocities of the circular parallel plates with selectable diameters. The samples were placed between the plates, 4 mm in diameter, with an initial gap of 2 mm apart. To reduce inertial effects, the slow retraction method (SRM) developed by Campo-Deano and Clasen 2010 [29] was employed. The velocities of the movable plate (65 and 130 µm s^{-1}) were low enough to ensure that the liquid bridge undergoes a sequence of equilibrium states until the elasto-capillary instability occurs.

Digital images were acquired using a high speed camera (Photron, FASTCAM Mini UX100) coupled with a high-resolution lens system (Optem Zoom 70 XL). The images were recorded with a 1280 x 312 pixels resolution, at 16000 frames per second (fps) and an exposure time of 1/4000 µs. The resulting image scale factor was 3.57 µm/pixel. The images were digitally processed in Matlab to detect the filament interface [30]. The time evolution of the filament diameter was fitted by an exponential function [31]:

$$\frac{D(t)}{D_0} = \mathrm{C}\, e^{\left(\frac{-t}{3\lambda}\right)} \tag{5.1}$$

where D_0 is the diameter of the filament at $t = 0$, λ the relaxation time and C is a constant, $C = [GD_0/(4\sigma)]^{1/3}$, where G is the fluid elastic modulus.

The relaxation time was calculated from the slope of the linear fit of the data of $\log[D(t)/D_0]$ versus time, t [2, 29, 30]. All measurements were carried out at room temperature, 22 ± 2 ºC.

5.2.3 CFL thickness measurements

The CFL was analysed through the flow of a 21 % (w/w) suspension in a contraction, Figure 5.2. The suspension was placed on a goblet and continuously agitated on a magnetic stirrer to prevent particle sedimentation, Figure 5.2. The suspension was then drawn from the vessel and forced to pass through the microchannel using a dedicated syringe pump, Figure 5.2. The Reynolds numbers, $Re = \rho U W_{in}/\mu$, were in the range 0.08 to 2.13, similar to the range found *in vivo* and *in vitro* studies of blood samples in microvessels [25, 32, 33].

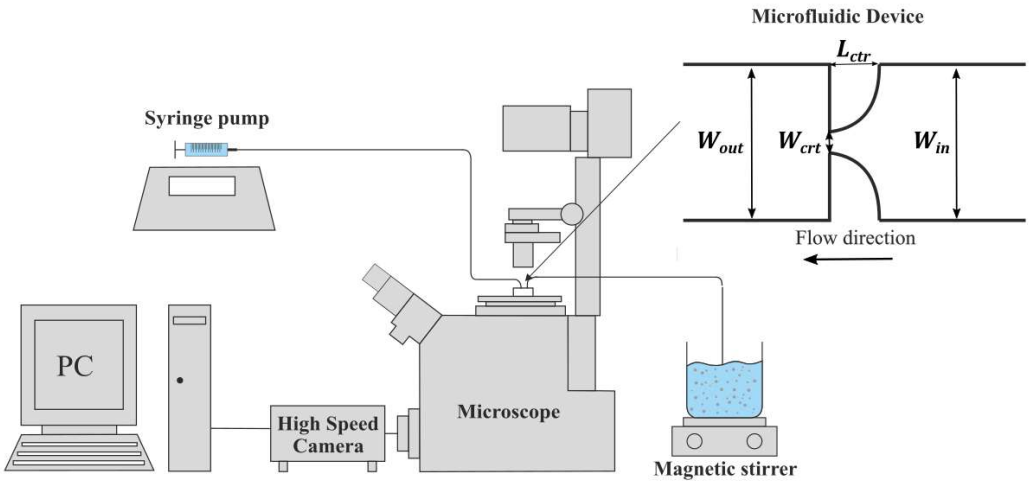

Figure 5.2. CFL analysis experimental setup.

The microchannel was fabricated using a soft-lithography technique [34]. The microchannel has inlet and outlet channels of the same width, 398 µm, and a hyperbolic

contraction with a length of 125 µm (L_{ctr}) and an initial width of 50 µm (W_{ctr}). The hyperbolic contraction corresponds to a Hencky strain of 2 ($\varepsilon_H = \ln(W_{in}/W_{ctr})$), Figure 5.2. The depth is 100 µm. This microchannel geometry was used in previous hemodynamics studies of RBCs suspensions in Dextran 40 (Dx 40) to evaluate the CFL formation [24, 25].

To avoid air bubbles, before each experiment the PDMS surface was modified from hydrophobic to hydrophilic by applying air plasma surface-treatment in a low pressure Plasma Reactor (Diener® electronic GMbH, model ZEPTO). To capture and analyze the flow in the CFL experiments, images were taken, 1280 x 740 pixels resolution, at a frame rate of 4000 frames/s and a shutter speed of 1/10000 s via a high speed camera (Photron, FASTCAM Mini UX100). All the flow experiments were carried out at room temperature, 22 ± 2 ºC.

To measure the CFL thickness, a procedure developed elsewhere was used [32, 35, 36]. Recorded image sequences were analyzed in ImageJ [37, 38] software using a manual tracking plugin, "MTrackJ" plugin. The CFL thickness was obtained by tracking and measuring the distance of the nearest particles to the wall. Also, similarly to previous works, the observed CFL was residual upstream the contraction and consequently the CFL thickness analyses was only performed downstream to the contraction [25, 32].

5.3 Results and Discussion

In order to study the outcome of the emulsification procedure, the particles obtained from the emulsification process of a 21 % (w/w) PDMS suspension were characterized.

The diameter of at least 200 droplets and 200 microparticles, were measured for each emulsification and for the final cured sample. The average diameters, over multiple experiments, of droplets and microparticles, $\overline{D}_d$ and $\overline{D}_p$ respectively, as well as the respective coefficients of variance (CV), were calculated and the size distribution is represented in Figure 5.3.

Observing the size distributions, particles with ~ 40-50 µm are present after the 1st membrane emulsification, Figure 5.3a. These larger particles, even in small number,

are undesirable since they can clog the flow in a microchannel. After the 2nd and 3rd membrane emulsifications only sub 20 µm particles are found, Figure 5.3b and c. Moreover $\overline{D}_d$ decreases after each membrane emulsification and the decrease is higher from the 1st to 2nd compared to the 2nd to 3rd membrane emulsification. The standard deviation follows the same trend achieving a minimum CV of~ 25 % in the 3rd filtration, Figure 5.3c. Comparing the distribution of the 3rd filtration with the distribution of the cured suspension, Figure 5.3c, size distribution, $\overline{D}_p$, and standard deviation are in very good agreement and so it can be concluded that there is no shrinkage during curing process as observed in a previous study [39]. Furthermore, $\overline{D}_p$ is within the size interval of RBCs [4],~7 µm.

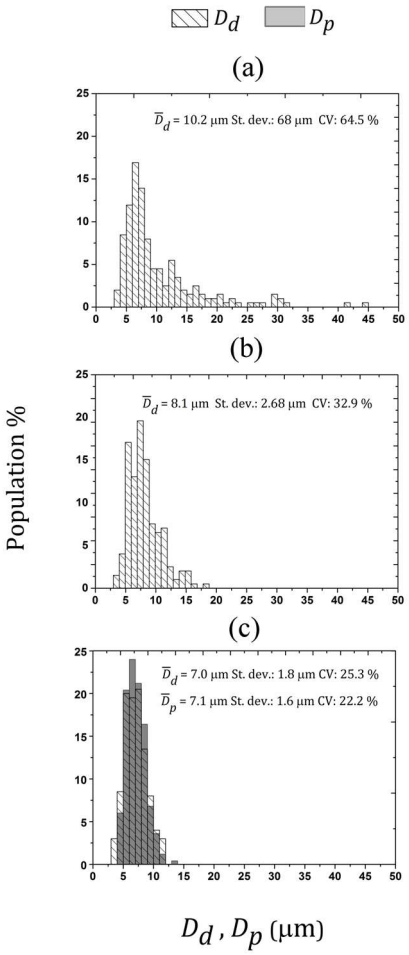

Figure 5.3. 21 % (w/w) PDMS suspension particles size distributions for a) first membrane emulsification; b) second membrane emulsification and c) third membrane emulsification and cured microparticles. 21 % (w/w) PDMS suspension.

5.3.1 Rheology of the suspensions

Steady-state shear rheology

The steady-state shear viscosity curves for the different concentrations of PDMS are shown in Figure 5.4. A shear-thinning behaviour is observed for suspensions with concentrations higher than 8 % (w/w).

The 21 % (w/w) PDMS suspension viscosity curve is in very good agreement with the whole blood viscosity curve at 37 ºC reported by Sousa, Carneiro [28], which makes this suspension a good candidate for a blood analogue suspension [28]. Note that this suspension has the advantage, among others, of being handled at a temperature of 20 °C, ideal for *in vitro* studies.

Also in Figure 5.4, the solvent 4 % SDS aqueous solution rheology shows a Newtonian behaviour with a constant viscosity of 1.44 mPa s and it is in good agreement with the viscosity of the plasma referenced in the literature, 1.1-1.35 mPa s [40].

The reproducibility of the suspension formation proceeding was reinforced by the matching of the different viscosity curves for each concentration obtained during the rheological study, exception of small variations at low shear rate (< 2 s^{-1}).

For deformation rates between 5 and 50 s^{-1}, straight lines were fitted according to the power law:

$$\mu = k\dot{\gamma}^{n-1} \tag{5.2}$$

where *k* and *n* are the consistency and power law indices respectively.

The power law indices, while similar, present a small, but constant, decrease with the concentration, Figure 5.5.

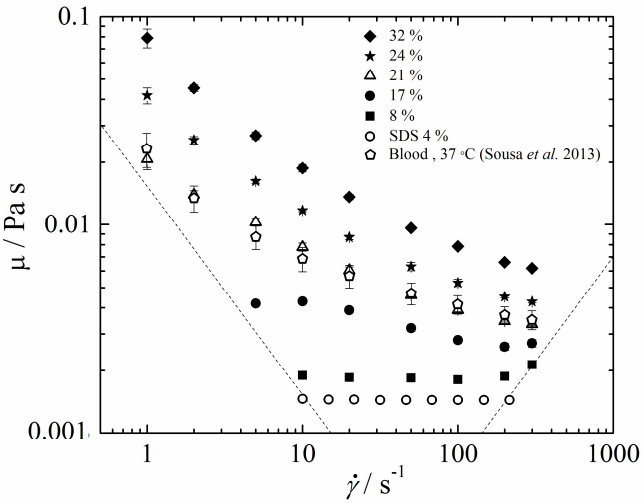

Figure 5.4. Steady-shear viscosity as a function of the shear rate measured at 20 °C, for the 8 %, 17 %, 21 %, 24 % and 32 % suspensions and also for blood (data from Sousa, Carneiro [28]) (2 donors, Htc = 41.6 and 41.3 %), and for a 4 % SDS aqueous solution. The dashed lines represent the minimum measurable shear viscosity based on 5× the minimum resolvable torque (i) and the onset of secondary flow due to Taylor instabilities (ii).

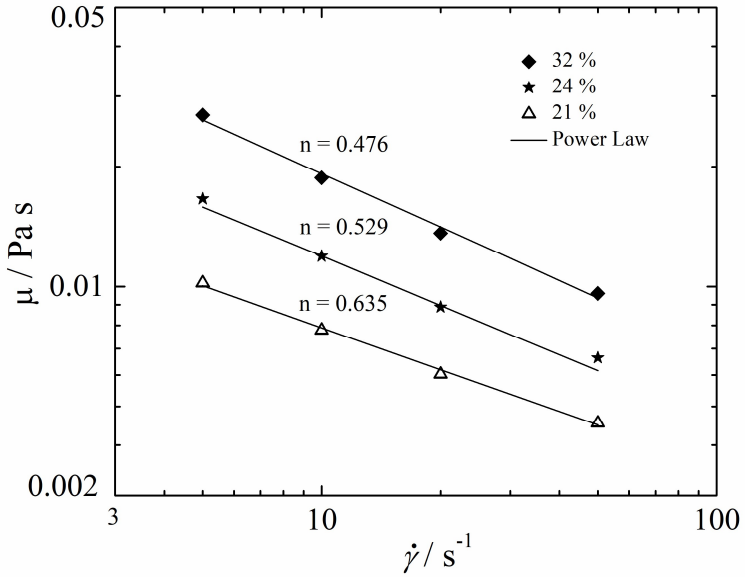

Figure 5.5. Steady-shear viscosity as a function of the shear rate for the interval 5 to 50 s^{-1}, for the 21, 24 and 32 % suspensions. The straight lines represent the power law fittings and *n* the power law index.

5.3.2 Extensional rheology of the blood analogue suspension

The diameter of the filament as a function of time is shown in Figure 5.6 for the 21 % (w/w) PDMS suspension, for the two velocities imposed, and also for the whole blood, data taken from Sousa, Vaz [30]. (Htc = 40.3 %) [30]. To note that the SRM setup used in this work is different from that of Sousa, Vaz [30], which uses custom made smaller plates (2 mm) and a smaller gap of 500 µm. Therefore, to compare the results at similar time ranges, the curves of the 21 % (w/w) PDMS suspension were shifted in time.

The time interval of the elasto-capillary regime, $\Delta t \sim 0.20$ ms, is in good agreement with that found in the literature for blood samples, $\Delta t \sim 0.22$ ms [30]. A quasi-cylindrical filament is observed in the time interval $0.68 \leq t \leq 0.88$ ms, Figure 5.6a-c. During this interval, the balance between viscoelasticity and capillarity forces governs the thinning of the filament.

The relaxation time obtained from the slopes of the red lines in Figure 5.6, 310 ± 15 µs, is also in reasonable agreement, with data from a recent study reporting the whole blood viscoelasticity, 114 ± 30 µs [30].

This relaxation time value is, however, near the ≈ 240 µs reported as the lower limit of the SRM [29] using identical experimental setup. Nonetheless, it gives an idea of the elasticity of the suspension, which is weakly elastic similarly to the blood [28].

The filament before breakup, t= 1 ms, Figure 5.6d, has an irregular shape which may be due to a non-uniform distribution of the PDMS particles along the thin filament. Although this non-uniformity was also present in extensional measurements of whole blood samples [30], the thread breaks at its end instead at the middle, Figure 5.6e. Besides the difference between particles and red blood cells (RBCs) concentrations, one possible explanation is the higher velocities used in this work, 65 µm s^{-1} and 130 µm s^{-1} compared to 10 µm s^{-1} used by Sousa, Vaz [30].

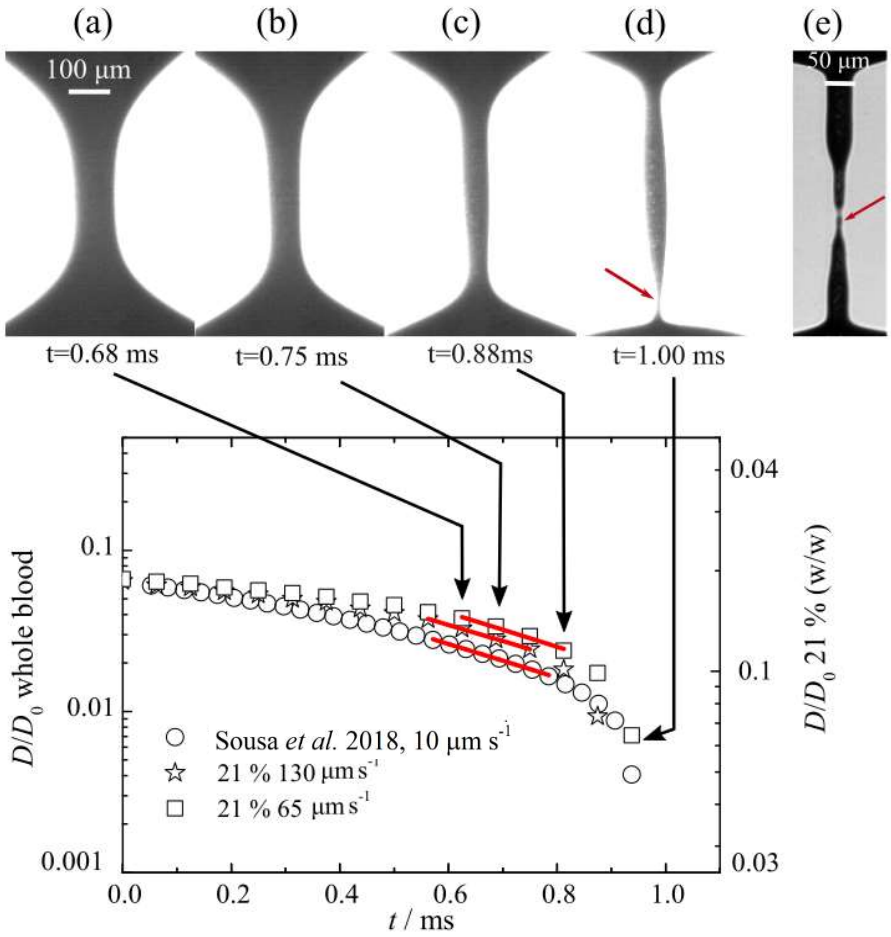

Figure 5.6. Time evolution of the minimum filament diameter for two velocities, 65 and 130 µm/s, for the 21 % (w/w) PDMS suspension and for blood taken from Sousa et al. [30] (Htc = 40.3 %, donor D3). The lines represent the fits to determine the extensional relaxation time. The curves of the 21 % (w/w) PDMS solution were shifted in time. Sequence of images showing the evolution of the filament, 130 µm/s, at the elastic-capillary regime, (a)-(c), filament before breaking (d) and Sousa, Vaz [30] filament before breaking, 10 µm s^{-1}, $\lambda \sim 110$ µs (e) are shown in the upper part of the figure .

5.3.3 CFL thickness

In this study, flow visualizations and measurements of the CFL thickness were carried out for three different suspensions: 21 % (w/w) PDMS suspension and two diluted suspensions 5 % and 10 % (w/w) (prepared from the 21 % (w/w) PDMS suspension). The steady-state rheology of these suspensions is represented in Figure 5.7.

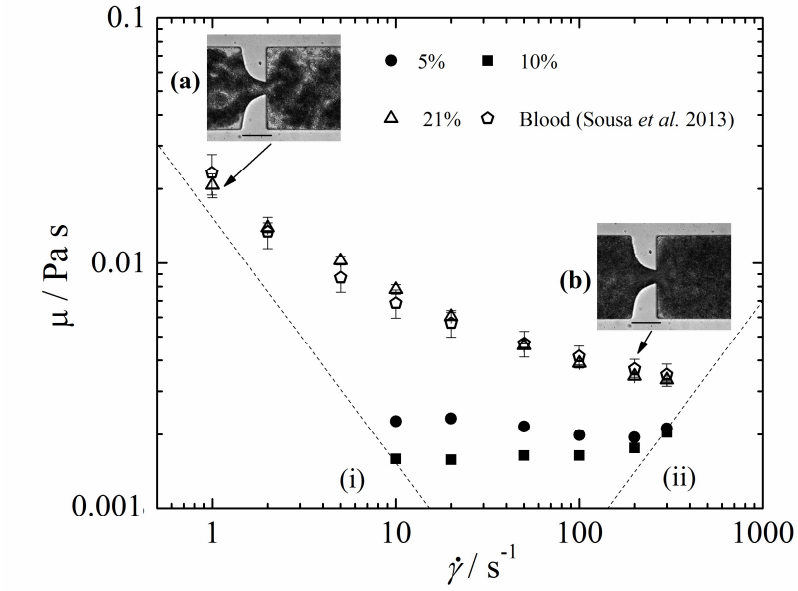

Figure 5.7. Steady-shear viscosity as a function of the shear rate measured at 20 ◦C, for the 21 % (w/w) suspension, whole blood from Sousa, Carneiro [28] (average and standard deviation from 2 donors) and for 5 % and 10 % (w/w) suspensions. The dashed lines represent the minimum measurable shear viscosity based on 5× the minimum resolvable torque (i) and the onset of secondary flow due to Taylor instabilities (ii). (a) and (b): flow images of the 21 % (w/w) suspension at Re ~ 0.03 , ~ 1 s^{-1}, and Re ~ 1.00, ~ 210 s^{-1}, respectively.

In Figure 5.7a, it is evident the aggregation of particles at low shear rates, $\dot{\gamma}$~ 1 s^{-1} while at $\dot{\gamma}$~ 210 s^{-1} the particles aggregation is not detectable, Figure 5.7b. The same phenomenon is also observed in *in vitro* studies with suspended RBCs [41, 42].

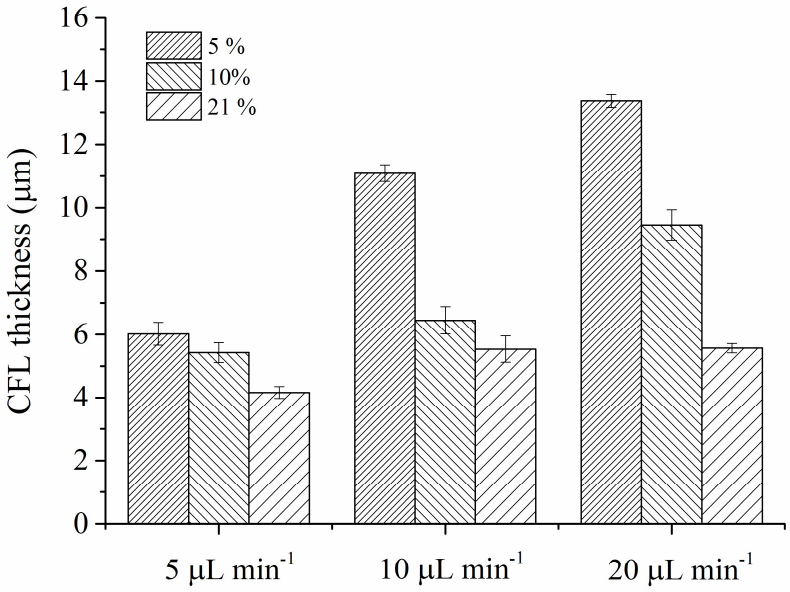

Figure 5.8. CFL thickness for the three suspensions: 5 %, 10 % and for 21 % at three different flow rates, 5, 10 and 20 μL/min. All the measurements were performed at 22 ± 2° C, and. The error bars represent the mean standard deviation.

Figure 5.8 shows the CFL thickness for the three suspensions at three different flow rates, 5, 10 and 20 μL min^{-1}. Except for the 21 % (w/w) PDMS, the CFL thickness increases with the flow rate. By its turn, the CFL thickness decreases with the concentration. The different behavior for the 21 % (w/w) PDMS suspension at higher flow rates is in agreement with those observed in suspensions of healthy RBCs in Dx40 in similar flow conditions [25].

Figure 5.9 shows the flow of 5 % and 21 % (w/w) PDMS suspensions passing through the contraction for two flow rates: 5 and 20 μL min^{-1}. Regarding the CFL thickness, the flow images in Figure 5.9 reinforce the results and conclusions taken from Figure 5.8.

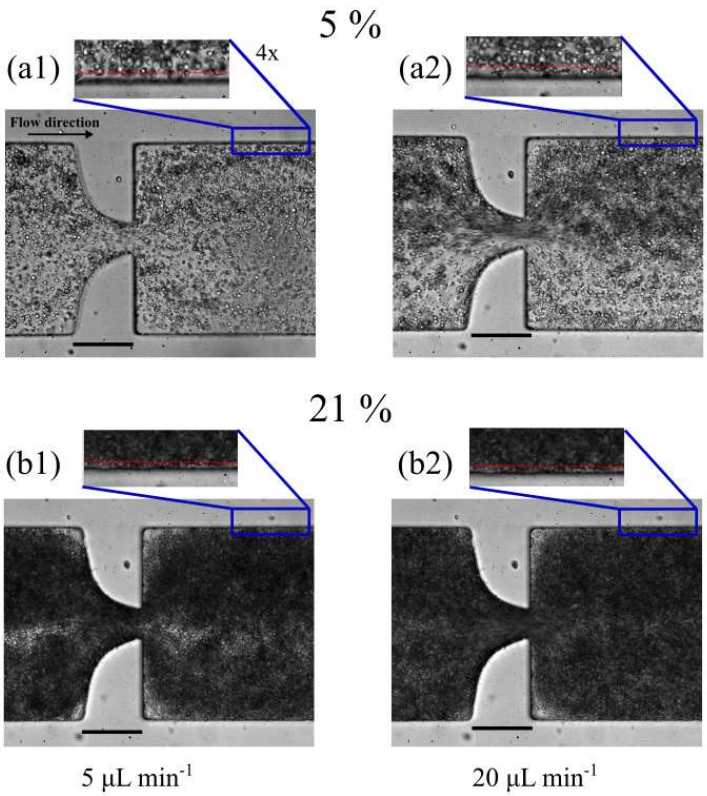

Figure 5.9. Flow visualizations of the suspension for 5 and 21 % and 5 µL/min, and 20 µL/min, objective 20x. Zoomed images, 4x, of the CFL near the channels wall. Scale bar: 100 µm.

5.4 Conclusions

In this work, a blood analogue suspension was successfully produced by generating PDMS microparticles via a high throughput multi-stage membrane emulsification. For that purpose, different concentration of PDMS were tested and a concentration of a 21 % (w/w) PDMS suspension exhibited good results, when compared to human blood, on both steady and extensional experiments. Also the average particle diameter is within the RBCs sizes, 7 µm, with a maximum CV of ~ 25 % which is a reasonable result compared to the CV of PDMS microparticles produced using microfluidic flow focusing techniques in the jetting regime, ~17 % [4, 43]. With the protocol described in this work, a blood analogue can be produced in under 3 hours and the microparticle concentration can be tuned to cover a wide haematocrit range. The CFL thickness

studies show good qualitative results [41, 42]. Also, shear dependent aggregation/disaggregation of microparticles is observed. In future studies, mechanical properties of the individual PDMS particles should be accessed and compared to those of blood cells and also in depth flow studies should be conducted.

Acknowledgements

This work was funded by FEDER funds through COMPETE2020—Operational Programme for Competitiveness Factors (POCI) and National Funds (PIDDAC) through FCT (Fundação para a Ciência e a Tecnologia) under projects UID/EMS/00532/2019, POCI-01-0145-FEDER-016861-PTDC/QEQ-FTT/4287/2014 and grant PD/BD/114313/2016. The authors thank Rui Lima for providing the channel molds for the CFL thickness study.

Notation

Latin	Definition	Units
CV	Coefficient of variance	(%)
$D(t)$	Diameter of the filament of the capillary thinning process at t	(m)
D_0	Diameter of the filament at $t = 0$	(m)
D_d	Droplet diameter	(µm)
$\overline{D}_d$	Average droplet diameter	(m)
D_p	Microparticle diameter	(µm)
$\overline{D}_p$	Average microparticle diameter	(µm)
$D(t)$	Diameter of the filament of the capillary thinning process at t	(m)
D_0	Diameter of the filament at $t = 0$	(m)
G	Elastic modulus	(Pa)
k	Power law consistency index	---
L_{ctr}	Hyperbolic contraction length	(µm)
n	Power law index	---
t	Time	(s)
U	Velocity	(m s^{-1})
W_{ctr}	Initial width of the hyperbolic contraction	(µm)
W_{in}	Inlet channel width	(µm)
W_{out}	Outlet channel width	(µm)

Greek	Definition	Units
Δt	Time interval	(s)
$\dot{\gamma}$	Shear rate	(s^{-1})
ε_H	Hencky strain	---
λ	Relation time	(s)
μ_c	Dynamic viscosity of the continuous phase	(Pa s)
μ_d	Dynamic viscosity of the dispersed phase	(Pa s)
ρ	Fluid density	(kg m^{-3})
ρ_c	Density of continuous phase	(kg m^{-3})
ρ_d	Density of dispersed phase	(kg m^{-3})

Dimensionless numbers	Definition
Re	Reynolds number

Acronyms	Definition
CFL	Cell-free layer
Dx 40	Dextran 40
DMSO	Dimethyl sulfoxide
Htc	Hematocrit
PDMS	Polydimethylsiloxane
RBC	Red blood cell
SDS	Sodium dodecyl sulfate
SRM	Slow retraction method

References

1. Sousa, P.C., et al., *A review of hemorheology: Measuring techniques and recent advances.* Korea-Australia Rheology Journal, 2016. **28**(1): p. 1-22.
2. Brust, M., et al., *Rheology of Human Blood Plasma: Viscoelastic Versus Newtonian Behavior.* Physical Review Letters, 2013. **110**(7): p. 078305.
3. Completo, C., V. Geraldes, and V. Semiao, *Rheological and dynamical characterization of blood analogue flows in a slit.* International Journal of Heat and Fluid Flow, 2014. **46**(0): p. 17-28.
4. Robertson, A., A. Sequeira, and M. Kameneva, *Hemorheology*, in *Hemodynamical Flows*. 2008, Birkhäuser Basel. p. 63-120.
5. Campo-Deaño, L., et al., *Viscoelasticity of blood and viscoelastic blood analogues for use in polydymethylsiloxane in vitro models of the circulatory system.* Biomicrofluidics, 2013. **7**(3): p. -.
6. Brust, M., et al., *The plasma protein fibrinogen stabilizes clusters of red blood cells in microcapillary flows.* Sci. Rep., 2014. **4**.
7. Wagner, C., P. Steffen, and S. Svetina, *Aggregation of red blood cells: From rouleaux to clot formation.* Comptes Rendus Physique, 2013. **14**(6): p. 459-469.
8. Baskurt, O.K. and H.J. Meiselman, *Blood Rheology and Hemodynamics.* Semin Thromb Hemost, 2003. **29**(05): p. 435-450.
9. Fåhraeus, R., *The suspension stability of the blood*. Vol. 9. 1929. 241-274.
10. Sollier, E., et al., *Fast and continuous plasma extraction from whole human blood based on expanding cell-free layer devices.* Biomedical Microdevices, 2010. **12**(3): p. 485-497.
11. Lindqvist, R.F.T., *The viscosity of the blood in narrow capillary tubes.* American Journal of Physiology, 1931. **96**: p. 562-568.
12. Pries, A.R., T.W. Secomb, and P. Gaehtgens, *Biophysical aspects of blood flow in the microvasculature.* Cardiovascular Research, 1996. **32**(4): p. 654-667.
13. Lima, R., et al., *In vitro blood flow in a rectangular PDMS microchannel: experimental observations using a confocal micro-PIV system.* Biomedical Microdevices, 2008. **10**(2): p. 153-167.
14. Boyle, J., *Microcirculatory hematocrit and blood flow.* Journal of Theoretical Biology, 1988. **131**(2): p. 223-229.
15. Goldsmith, H.L., G.R. Cokelet, and P. Gaehtgens, *Robin Fahraeus: evolution of his concepts in cardiovascular physiology.* American Journal of Physiology-Heart and Circulatory Physiology, 1989. **257**(3): p. H1005-H1015.
16. Benis, A.M. and J. Lacoste, *Study of erythrocyte aggregation by blood viscometry at low shear rates using a balance method.* Circulation Research, 1968. **22**(1): p. 29-41.
17. Chien, S., *Shear dependence of effective cell volume as a determinant of blood viscosity.* Science, 1970. **168**(3934): p. 977-979.
18. Thurston, G.B., *Rheological parameters for the viscosity viscoelasticity and thixotropy of blood.* Biorheology, 1979. **16**(3): p. 149-62.
19. Pirofsky, B., *The determination of blood viscosity in man by a method based on Poiseuille's law.* The Journal of clinical investigation, 1953. **32**(4): p. 292-298.

20. Picart, C., et al., *Human blood shear yield stress and its hematocrit dependence.* Journal of Rheology, 1998. **42**(1): p. 1-12.
21. Travagli, V., et al., *Comparison of blood viscosity using a torsional oscillation viscometer and a rheometer.* Clinical Hemorheology and Microcirculation, 2008. **38**(2): p. 65-74.
22. Baskurt, O.K., et al., *New guidelines for hemorheological laboratory techniques.* Clinical Hemorheology And Microcirculation, 2009. **42**(2): p. 75-97.
23. Sousa, P.C., et al., *Flow of a Blood Analogue Solution Through Microfabricated Hyperbolic Contractions*, in *Computational Vision and Medical Image Processing*, J.M.R.S. Tavares and R.M.N. Jorge, Editors. 2011, Springer Netherlands. p. 265-279.
24. Calejo, J., et al., *Particulate Blood Analogues Reproducing the Erythrocytes Cell-Free Layer in a Microfluidic Device Containing a Hyperbolic Contraction.* Micromachines, 2016. **7**(1): p. 4.
25. Pinho, D., et al., *In vitro particulate analogue fluids for experimental studies of rheological and hemorheological behavior of glucose-rich RBC suspensions.* Biomicrofluidics, 2017. **11**(5): p. 054105.
26. Carvalho, D.A.M., et al., *Microfluidic Deformability Study of an Innovative Blood Analogue Fluid Based on Giant Unilamellar Vesicles.* Journal of functional biomaterials, 2018. **9**(4): p. 70.
27. Vladisavljević, G.T., I. Kobayashi, and M. Nakajima, *Production of uniform droplets using membrane, microchannel and microfluidic emulsification devices.* Microfluidics and Nanofluidics, 2012. **13**(1): p. 151-178.
28. Sousa, P.C., et al., *Shear viscosity and nonlinear behavior of whole blood under large amplitude oscillatory shear.* Biorheology, 2013. **50**(5-6): p. 269-282.
29. Campo-Deaño, L. and C. Clasen, *The slow retraction method (SRM) for the determination of ultra-short relaxation times in capillary breakup extensional rheometry experiments.* Journal of Non-Newtonian Fluid Mechanics, 2010. **165**(23): p. 1688-1699.
30. Sousa, P.C., et al., *Rheological behavior of human blood in uniaxial extensional flow.* Journal of Rheology, 2018. **62**(2): p. 447-456.
31. Entov, V.M. and E.J. Hinch, *Effect of a spectrum of relaxation times on the capillary thinning of a filament of elastic liquid.* Journal of Non-Newtonian Fluid Mechanics, 1997. **72**(1): p. 31-53.
32. Rodrigues, R.O., et al., *In vitro blood flow and cell-free layer in hyperbolic microchannels: Visualizations and measurements.* BioChip Journal, 2016. **10**(1): p. 9-15.
33. Waite, L. and J.M. Fine, *Applied biofluid mechanics.* 2007.
34. Carneiro, J., et al., *PDMS droplet formation and characterization by hydrodynamic flow focusing technique in a PDMS square microchannel.* Journal of Micromechanics and Microengineering, 2016. **26**(10): p. 105013-105013.
35. Pinho, D., et al., *Automatic tracking of labeled red blood cells in microchannels.* International Journal for Numerical Methods in Biomedical Engineering, 2013. **29**(9): p. 977-987.
36. Pinho, D., T. Yaginuma, and R. Lima, *A microfluidic device for partial cell separation and deformability assessment.* BioChip Journal, 2013. **7**(4): p. 367-374.

37. Schindelin, J., et al., *Fiji: an open-source platform for biological-image analysis.* Nature methods, 2012. **9**(7): p. 676.
38. Rueden, C.T., et al., *ImageJ2: ImageJ for the next generation of scientific image data.* BMC bioinformatics, 2017. **18**(1): p. 529.
39. Muñoz-Sánchez, B.N., et al., *Generation of micro-sized PDMS particles by a flow focusing technique for biomicrofluidics applications.* Biomicrofluidics, 2016. **10**(1): p. 014122-014122.
40. Robertson, A.M., A. Sequeira, and M.V. Kameneva, *Hemorheology*, in *Hemodynamical Flows: Modeling, Analysis and Simulation*, G.P. Galdi, et al., Editors. 2008, Birkhäuser Basel: Basel. p. 63-120.
41. Mehri, R., C. Mavriplis, and M. Fenech, *Red blood cell aggregates and their effect on non-Newtonian blood viscosity at low hematocrit in a two-fluid low shear rate microfluidic system.* PLOS ONE, 2018. **13**(7): p. e0199911.
42. Reinke, W., P. Gaehtgens, and P.C. Johnson, *Blood viscosity in small tubes: effect of shear rate, aggregation, and sedimentation.* American Journal of Physiology-Heart and Circulatory Physiology, 1987. **253**(3): p. H540-H547.
43. Carneiro, J., J.B.L.M. Campos, and J.M. Miranda, *PDMS microparticles produced in PDMS microchannels under the jetting regime for optimal optical suspensions.* Colloids and Surfaces A: Physicochemical and Engineering Aspects, 2019. **580**: p. 123737.

6

Chapter

Conclusions and Future work

6

Conclusions and Future work

This chapter summarizes the contributions of the present thesis to the field, and discusses possible extensions and future work.

6.1 Thesis conclusions

The main goal of the present thesis is the production of Polydimethylsiloxane PDMS microparticles to further develop a blood analogue suspension. The microparticles were generated via microfluidic devices and membrane emulsification.

The generation of PDMS droplets via a microfluidic device was performed in a square section flow-focusing microfluidic channel also made of PDMS. The generation of PDMS droplets in a channel of the same material imposed several challenges, due to the affinity of the liquid pre-polymer PDMS to the channel walls. Also, the high viscosity of the PDMS liquid pre-polymer, at least 600 times higher than water, was an obstacle as the high pressure needed inside the channel could damage it. A careful study of the best conditions to produce PDMS droplets was performed and a flow map regime, based on the disperse and continuous capillary numbers, was constructed for a system with a viscosity ratio of $\chi \approx 533$. Different regimes were identified: dripping, jetting, threading and viscous displacement regime. The flow regime map gave insights for the best conditions to generate stable and monodisperse droplets, and also for formation frequency and breakup distance. Moreover, the dripping to jetting transition was found to be near a critical disperse phase capillary number, $Ca_{cri} \approx 10^{-1}$, a similar value to that referred in the literature [1]. Jetting and dripping were the regimes capable of producing droplets. In the dripping regime, it is possible to achieve droplets with sizes larger

than the channels characteristic dimension and with low size dispersion (coefficients variance (CV) around 3 %), at a generation frequency up to ≈ 12 Hz. Contrarily, in the e jetting regime, sub-channel droplet sizes were generated, but with high size dispersion, 13 % ≤ CV ≤105 %, at a frequency up to ~ 25 Hz. The experimental study of PDMS droplets formation was complemented with a numerical one for high viscosity ratios, $\chi \geq 24$. The numerical code, Ansys Fluent, based on a coupled level-set method and a volume of fluid method (CLSVOF), successfully predicted droplets size in surfactant free systems and also the transition from dripping to jetting. In the presence of surfactant, under certain flow conditions, the numerical code fails the prediction of the droplets size. Although the numerical study was computationally very demanding, it was possible to analyse a wide range of high viscosity ratios, $24 \leq \chi \leq 1480$.

The next step was an attempt to produce large quantities of PDMS microdroplets in the same microfluidic channel but with a lower viscosity ratio system, $\chi = 6$. This lower viscosity ratio provided more stable droplets, especially in the jetting regime. By controlling the flow rate ratio, droplet sizes ranging from ~ 27 to 59 µm were achieved with a maximum production frequency of ~ 1.3 kHz. The size dispersion of the droplets was relatively low, considering the jetting regime, with a maximum CV of ~ 17 %. The PDMS droplets were cured and no shrinkage was observed. The microparticles composition was also analyzed and presents very similar results to pristine PDMS samples. This observation was further sustained by their optical properties, analyzed by submerging the microparticles in a known PDMS refractive matching fluid. When submerged, microparticles do not refracted light and became invisible because the refractive index of both, fluid and microparticles, match. Owing to their good optical properties, PDMS microparticles produced by the proposed method are adequate to be used in visualization and velocimetry experiments.

The size and production rate of PDMS microparticles achieved by the microfluidic flow focusing channel were still insufficient to produce the volumes of blood analogue suspensions required to conduct a rheological characterization. Therefore, an alternative was pursued and the choice was a membrane emulsification process. A blood analogue suspension was successfully produced by generating PDMS microparticles via a high throughput multi-stage membrane

emulsification. With the protocol implemented, a blood analogue can be produced in under 3 hours and the microparticles concentration can be tuned to cover a wide hematocrit range. Different concentrations of PDMS were tested and a concentration of 21 % (w/w) PDMS microparticles suspension, at ~ 20 °C, presents a steady-state shear and extensional rheology very similar to that of the whole blood, at 37 °C, making it a good candidate for a blood analogue suspension. Also, the average particles diameter is within the red blood cells (RBCs) size range, 7 µm with a maximum CV of ~ 25 %, which is a value worse, but still acceptable, when compared to the CV of PDMS microparticles produced using the microfluidic flow focusing technique in the jetting regime. Preliminary cell-free layer thickness tests were performed and good qualitative results were attained. Also, shear dependent aggregation/disaggregation of microparticles was observed.

As already referred, the ultimate goal of this thesis was the production and characterization of droplets and microparticles of PDMS to be further used in blood analogue suspensions. The objective was successfully accomplished and incremental and a deeper understanding about the production of highly viscous polymeric droplets was also achieved. The PDMS blood analogue suspension developed in the present thesis will be used in future flow studies at both macro and micro scale.

6.2 Future work

The results presented in this thesis provide valuable solutions to produce a novel blood analogue suspension. The production of PDMS microparticles generated via microfluidic devices was well characterized and the process is capable of producing microparticles with controlled size. Despite that, the amount and size of the droplets produced were insufficient to attain a workable blood analogue suspension. A future possible solution is to increase the production rate by parallelization of the droplets generation. An initial attempt to parallelize was made (not reported in this thesis), however the channels deformed due to the high pressures developed inside the PDMS channel, as expected when a viscous fluid flows in a microfluidic channel made of an elastomer. In the future, it would be

interesting to test different channels materials that can withstand higher pressures, such as Polymethylmethacrylate (PMMA) or glass [2]. The use of a stiffer material should allow a more robust microfluidic device with the capacity of handling higher flow rates and, consequently, allowing a higher throughput production of small droplets.

The alternative method to produce PDMS microparticles, membrane emulsification process, allows the production of high quantities of PDMS microparticles with RBCs size, however the size dispersion is high. The CV could be lowered by finding a membrane with more equally spaced pores.

A PDMS blood analogue suspension was successfully produced and rheologically characterized. In the future, it would be interesting to perform a dynamic oscillatory shear characterization to further investigate the viscoelastic behavior of the blood analogue. Also, the blood analogue should be tested in, both, macro and micro-scale hemodynamic studies. Furthermore, deformation tests of the PDMS particles should be made and the results compared to those of RBCs. A very recent study reports a deformability analysis of PDMS microparticles comparing against healthy and pathological RBCs [3]. The authors concluded that the deformation index of PDMS microparticles is in between healthy and pathological RBCs. Also, the optical characteristics of PDMS should be further explored in order to perform Micro Particle Image Velocimetry (μPIV), in high density suspensions flowing in realistic patient specific PDMS vessels [4]. The blood analogue will be also relevant for blood flow studies in others micro conditions, for example, in capillary bifurcations and in two-phase (blood/air) flows (embolism).

As a final remark, the proposed methods to produce PDMS particles is not limited to the production of blood analogues and can be used in a variety of other biomedical applications, i.e. sensors, tracer particles, tissue oxygenation and suspensions of magnetic particles used to control the fluid rheology.

References

1. Cubaud, T. and T.G. Mason, *Capillary threads and viscous droplets in square microchannels.* Physics of Fluids, 2008. **20**(5): p. 053302.
2. Yadavali, S., et al., *Silicon and glass very large scale microfluidic droplet integration for terascale generation of polymer microparticles.* Nature Communications, 2018. **9**(1): p. 1222.
3. Pinho, D., et al., *Flexible PDMS microparticles to mimic RBCs in blood particulate analogue fluids.* Mechanics Research Communications, 2019. **100**: p. 103399.
4. Doutel, E., et al., *Geometrical effects in the hemodynamics of stenotic and non-stenotic left coronary arteries—numerical and in vitro approaches.* International Journal for Numerical Methods in Biomedical Engineering, 2019. **35**(8): p. e3207.

Appendix

Production of PDMS microparticles – a preliminary study

[*]J.Carneiro, E. Doutel, JBLM. Campos, JM. Miranda
Visualization of PDMS microparticles formation for biomimetic fluids, **Micro and Nanosystems**, https://doi.org/10.2174/1876402908666160106000558.

Visualization of PDMS microparticles formation for biomimetic fluids

Abstract

In vitro experiments of blood flow are usually performed with blood analogue fluids due to ethical and practical considerations. The ideal analogue must match the rheology of blood in multiple scales. Ideally, the blood analogue fluid should be a suspension of transparent particles with similar properties to red blood cells. PDMS particles are an interesting candidate because they are transparent, have a low refractive index and can be produced through polymerization by heating. Here we present a study to produce polydimethylsiloxane (PDMS) microparticles, to be used in biomimetic fluids, by droplet microfluidics. A microfluidic flow focusing device was employed to produce the droplets. A polymeric fluid (PDMS) was squeezed by two counter-flowing water streams, with 2 % of sodium dodecyl sulfate (SDS). The flow rate of the disperse phase (Q_d) was 1 µl min^{-1} and that of the continuous phase (Q_c) 5 µl min^{-1}. Both liquids were forced to flow through a narrow slit (25 µm × 100 µm) located downstream the channels where PDMS stream breaks into droplets. In these conditions, the device operated in the jetting regime, forming polydispersed droplets. Monodispersed microparticles were also obtained in the dripping regime. The droplets were then cured thermally to form microparticles. The process of droplet formation was filmed with a high-speed camera and the movies were analysed to relate the flow pattern to particle size distribution.

A.1 Introduction

One interesting aspect of most biofluids is their adaptation to the respective biological function. Blood is one of the best examples. Blood is a complex biofluid composed by plasma, red blood cell (RBC) and other cellular components. The rheological characteristics of blood are, accordingly, equally complex. The ability of blood rheology to change with the scale of the vessel, allowing the flow in large arteries and in narrow capillaries is of particular interest. This adaptability results from the RBCs role in blood rheology. RBCs can adjust their shape and penetrate into narrow capillary vessels. In vessels with a diameter less than 300 μm, the effective viscosity is reduced due to the migration of RBCs from the wall of the vessel, leaving a cell free layer that lubricates the flow. So, blood can be a source of inspiration for the development of particulate fluids with similar properties to be used in similar functions.

One of the main challenges of the development of biomimetic particulate fluids is the production of particles with the desired properties. One approach to this problem is to use microfluidic devices to produce the particles from microdroplets.

Microfluidics is a multidisciplinary technology with two decades of existence and it is a powerful platform for the generation of droplets and microparticles [1-17], with tailored sizes and shapes. The manipulation of small volumes of fluid at low Reynolds numbers and the ability to achieve much faster reaction times, compared to macroscale systems, make microfluidics systems an invaluable tool for a wide range of areas from engineering to biology [1-4]. Lab-on-a-chip systems, to generate microscale droplets of one fluid within a second immiscible carrier fluid, are a subclass of microfluidics [3]. The ability to synthesize monodisperse droplets, of controlled size and shape, has numerous potential applications in areas such as the production of emulsions, drug delivery, catalysis or medical imaging. Microfluidics offers also a promising path to synthetize microparticles, enabling the production of highly uniform particles in the micrometer size range [1-6].

Microfluidic research devices are generally fabricated in polydimethylsiloxane (PDMS) [1, 4, 9, 10, 18]. PDMS is a hydrophobic, transparent inert elastomer [18,

19]. Different configurations of microfluidic devices are used to generate droplets, being T-junction and flow focusing configurations the most popular [1, 4, 9].

PDMS is a promising candidate material to produce microparticles analogue to RBCs. PDMS microparticles would have a relatively small refractive index, which matches the index of a large variety of fluids and also that of channels made in PDMS. With this condition, optical techniques, such as Micro Particle Image Velocimetry (μPIV), can be performed in high density suspensions as well as in irregular circular shaped channels. There are, already, some studies regarding the production of PDMS microparticles by flow focusing techniques [17, 20]. All of them show the potential of this approach. However, more research is necessary to produce particles with a very small size (8 μm diameter).

The goal of the present work is to develop a microfluidic device to produce PDMS microparticles, which will be useful to create different transparent biomimetic fluids (due to the low refractive index of PDMS). Droplet formation in a microfluidic device is a high speed phenomenon. The precise way how the droplets form, determines the particle size distribution produced by this process. A high speed camera was used for visualization of droplet formation.

A.2 Materials and Methods

Figure A.1 shows a flow-focusing device used to produce the particles. In flow focusing devices, a dispersed phase (aqueous phase) is squeezed by two counter-flowing streams of a continuous phase [1, 4, 7, 10]. Both liquid phases, continuous and disperse, are forced to flow through a small orifice (nozzle) that is located downstream the inlet channels, see Figure A.1. The continuous phase forces the dispersed phase to flow into the narrow gap, where the disperse phase breaks into droplets. The droplets are then thermally cured to produce microparticles [17].

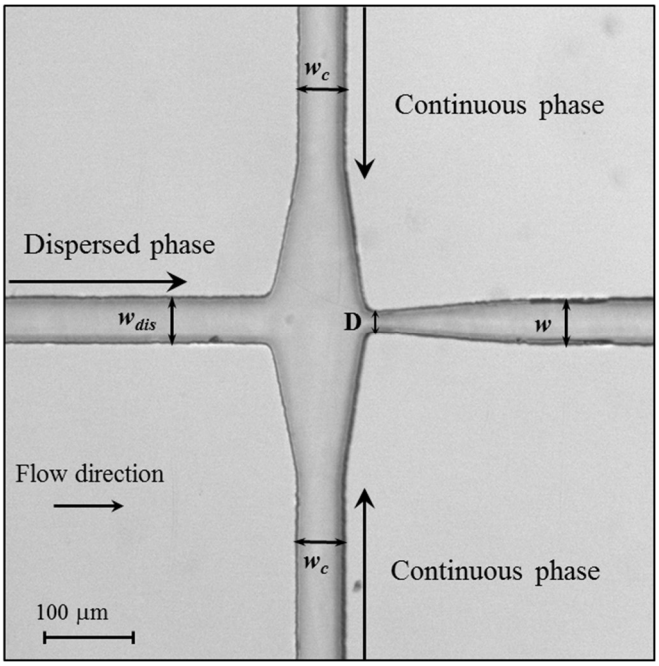

Figure A.1. Flow-focusing geometry implemented in a microfluidic device. The microdevice is composed by two channels for the continuous phase, one channel for the dispersed phase and one downstream channel. The later has an inlet orifice with a width of D = 25 μm. The depth of all the channels is 100μm and the width 50 μm. w_{dis} , w_c and w are the dispersed phase , continuous phase and outlet channels widths, respectively.

A.2.1 Reagents

The PDMS (Sylgard 184, Dow Corning) used to fabricate the micro devices and to produce the microparticles is a two part kit composed by a PDMS pre-polymer and a curing agent. Parts are mixed at different proportions depending on the desirable final mechanical proprieties [21]. The pre-polymer PDMS that comprised the dispersed phase was composed of 60 % PDMS base and 40 % of curing agent (6:4).

In the microdroplet formation experiments, the continuous phase was an aqueous solution of water and a surfactant, Sodium Dodecyl Sulfate (SDS) 2 % w/w, and the dispersed phase was the liquid pre-polymer PDMS containing the curing agent.

A.2.2 Microdevice fabrication

The microchannels fabrication method starts with the design of the geometries by computer-aided design (CAD). The CADs are sent to a specialized laboratory where the geometries are printed onto a chrome mask. The mask is used to produce SU-8 molds by photolithography.

The microchannels are fabricated by soft lithography [22] by pouring a well-mixed solution of PDMS and curing agent (5:1) onto the SU-8 mold. A thin layer of PDMS and curing agent (20:1) is spread, by spin coating, in a glass slide. Both, the mold and the coated glass slide are cured, in an oven, at 80 ºC for 20 minutes. The cured PDMS containing the channels is pealed from the SU-8 and sealed to the glass coated slide. To ensure a good sealing, the sealed channel is left to cure for approximately 12 hours at 80 ºC [22]. An overview of the fabrication method is depicted in Figure A.2.

In the particle formation experiment, the liquid pre-polymer cannot be in direct contact with the PDMS channel walls, since the pre-polymer PDMS has a high affinity with the hydrophobic PDMS of the channel walls, which is undesirable. With an oxygen plasma surface-treatment, the PDMS surface can be modified from hydrophobic to hydrophilic to have more affinity with the aqueous phase. To assure that the PDMS will behave as the dispersed phase, plasma treatment was carried out with air in a low pressure Plasma Reactor (Diener® electronic GMbH, model ZEPTO).

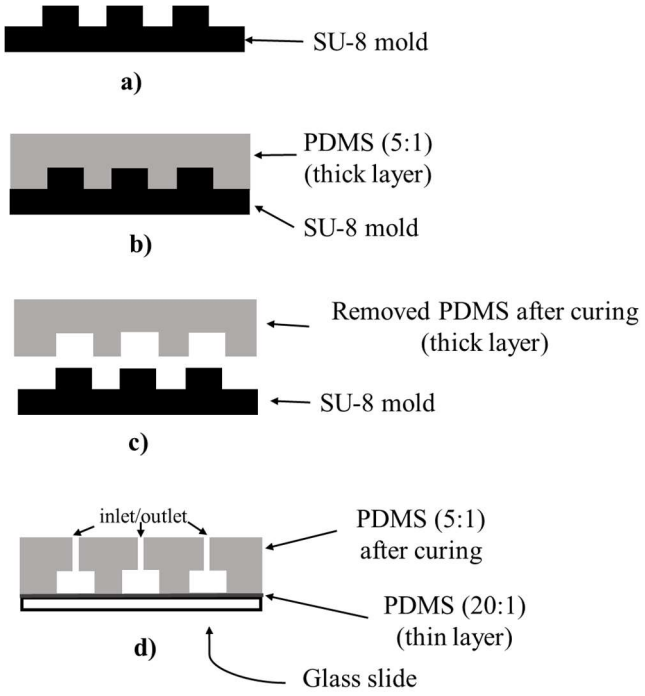

Figure A.2. Overview of the PDMS microchannel fabrication procedure: a) SU-8 mold with a positive relief; b) A mixture of polymer oligomer with curing agent, prepared in a ratio of 5:1, is poured onto the SU-8 mold (thick layer) and placed in the oven to cure during 20 minutes; c) After curing, the PDMS thick layer is removed from the SU-8 mold and access ports are created (inlets/outlets); d) PDMS layer containing the channel structure is bonded to the glass slide covered with a thin layer of PDMS and placed in the oven to further seal the channel.

A.2.3 Fluid characterization

The Sylgard 184 kit is comprised of a base polymer with a viscosity of 5 Pa.s and a curing agent with a viscosity of 0.11 Pa.s. The rheology of the 6:4 mixtures was characterized experimentally. Steady-state shear rheology of both fluids was characterized using a Rotational Rheometer (Physica MCR301, Anton Paar) with a Peltier temperature control system. The measurements were performed at 20 ºC using a 50 mm diameter plate–plate geometry, PP50, with a gap of h = 0.1 mm.

The density of both phases was measured with a 10 mL pycnometer. The interfacial tension between phases was measured at 20 °C in an Attension™ Theta Lite 100 goniometer.

A.2.4 Flow visualization

Images were captured at a rate of 4000 frames per second via a high-speed camera (FASTCAM Mini UX100, Photron) mounted on an inverted epifluorescence microscope (DMI 5000M, Leica Microsystems GmbH). Using a dedicated syringe pump, the dispersed and continuous phases were injected into the microchannel.

A.2.5 Flow characterization

The flow was characterized by the capillary numbers of the phases. The capillary number of phase *i,* Ca_i *,* is defined as:

$$\mathrm{Ca}_i = \frac{V_i \mu_i}{\sigma} \tag{A.1}$$

where V_i and μ_i are the velocity and viscosity of phase i, respectively and σ is the surface tension.

The velocity of phase i was estimated by:

$$V_i = \frac{Q_i}{Hw} \tag{A.2}$$

where Q_i is the flow rate of phase i. H and w are the depth and with of the outlet channel, respectively.

A.3 Results and Discussion

A.3.1 Fluid characterization

The water/SDS fluid had a constant viscosity of 0.00103 Pa s^{-1}. The density of the water/SDS fluid was 1010 kg m^{-3} and the density of the pre-polymer 1000 kg m^{-3}. The viscosity of the pre-polymer was measured for a period of 2 hours, the duration of a typical experiment, to verify if it can be affected by curing. It was found that throughout a 2 hour experiment, the viscosity increases approximately 11 %. The pre-polymer average viscosity was 0.640 Pa s^{-1}. The surface tension determined experimentally at 20 ºC was 0.013 N m^{-1}.

A.3.2 Droplet generation

Figure A.3 shows the typical flow pattern that can be obtained with the experimental setup. The two streams were forced together and droplets were generated through the constriction (nozzle). The flow rate of the disperse phase (Q_d) was 1 µl min^{-1} and the flow rate of the continuous phase (Q_c) was 5 µl min^{-1}. The dispersed phase is squeezed by the continuous phase and enters the nozzle forming a long filament which breaks up into droplets far from the junction. This flow pattern is characteristic of the jetting regime [23]. As can be observed, in the jetting regime droplet formation is unstable and the size of the particles obtained is not uniform.

Preliminary results have shown that the plasma treatment transformed the PDMS surfaces from hydrophobic to hydrophilic. In all experiments the PDMS behaved as the dispersed phase and the aqueous solution as the continuous phase.

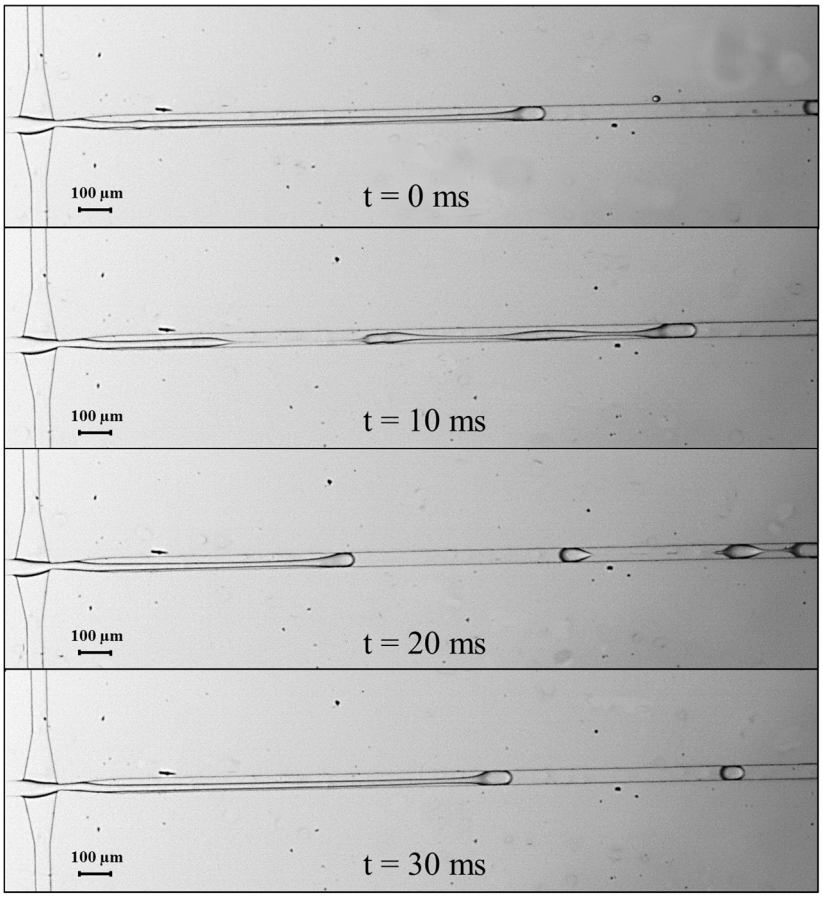

Figure A.3. Overview of a pre-polymer PDMS droplets formation, Q_d = 1 µl min^{-1}and Q_c = 5 µl min^{-1}. The capillary numbers of the dispersed and continuous phases are estimated to be 1.6×10^{-1} and 1.3×10^{-3}, respectively.

According to Cubaud and Mason; [23], the jetting regime is observed for values of the capillary number of the dispersed phase above 0.1. Results of Figure A.3 were obtained for a capillary number of the dispersed phase of 0.16, above the limit. Results of Figure A.4 were obtained for low capillary numbers (capillary number of the dispersed phase is estimated to be 0.03). In this case droplet formation is near the dripping regime. The droplets obtained in this experiment were of uniform size.

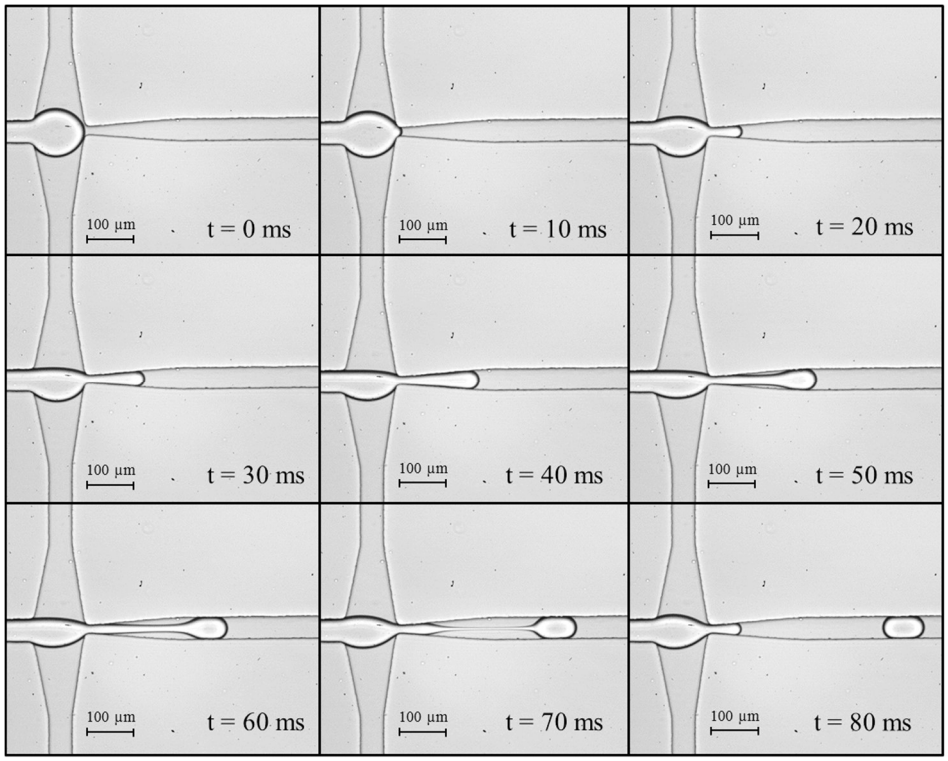

Figure A.4. Pre-polymer PDMS droplets formation in dripping regime (low accuracy of the experimental set-up) The capillary numbers of the dispersed and continuous phases are estimated to be 3.3×10^{-2} and 2.6×10^{-4}, respectively.

To obtain particles with uniform size, the system must operate in the dripping regime, in which the capillary numbers of the phases are small. The microfluidic device used in the experiments has small characteristic dimensions because it was designed to produce very small particles. Small characteristic dimensions combined with high viscosity of PDMS lead to high capillary numbers of the dispersed phase. For this reason, presently, the setup can operate accurately only in the jetting regime. Several options can be taken for the setup to be able to operate accurately in the dripping regime. The capillary numbers could be reduced by increasing the surface tension, but the only realistic possibility is by reducing the amount of surfactant used. However, the surfactant is necessary to avoid coalescence of the droplets. It is also possible to reduce the capillary number of the dispersed phase by reducing its viscosity. Viscosity of the PDMS can be reduced by increasing the ratio of curing agent in the pre-polymer mixture, but this

alternative will also change the mechanical properties of the particles. The lower bound of the viscosity that can be obtained by increasing the curing agent ratio is 0.11 Pa.s, the viscosity of the curing agent. It is also possible to reach the dripping regime by scaling up the microfluidic device, but this option would lead to an increase in the size of the particles. The easiest approach is to reduce the flow rate, by using a pump with higher precision and syringes with a smaller diameter.

A.3.3 Microparticles

At the outlet, the particles are suspended in the continuous phase. They were kept in the continuous phase and taken to the oven. It is advisable to cure the particles at 70º C for 10 minutes [17]. After curing, a suspension of particles in the continuous phase is obtained. The suspension is then washed and resuspended in distilled water and placed in the microscope to observe their morphology and size distribution. As seen in Figure A.5, the spherical particles obtained in the jetting regime are polydispersed in size. The particles obtained had a mean diameter of 56.4 ± 11.2 µm.

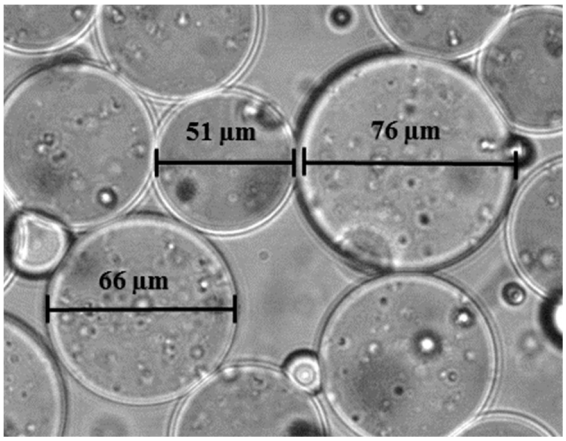

Figure A.5. Sample with particles of different sizes obtained in the jetting regime.

For the dripping regime, before the thermal cure, droplets at the outlet of the channel were measured, Figure A.6. Contrarily to the jetting regime, the dripping regime generates monodisperse droplets with a mean diameter of 84.6 ± 1.1 µm.

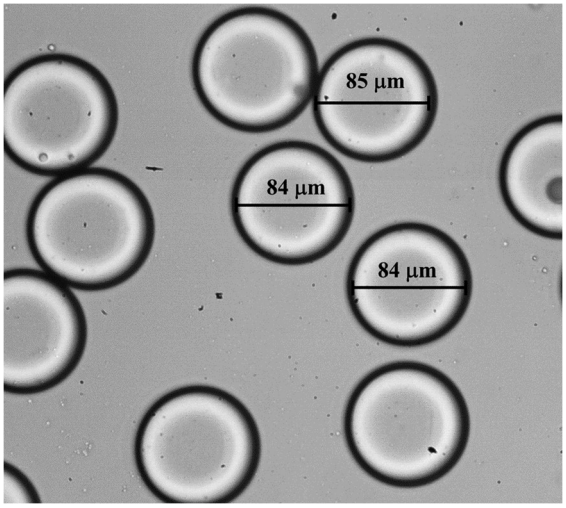

Figure A.6. Sample with droplets of similar sizes obtained in the dripping regime.

A.4 Conclusion

The study focuses on the visualization of PDMS microdroplets formation in a microfluidic device. The aim is to optimize the synthesis of PDMS microparticles. PDMS is a cheap, ubiquitous and well-studied material in the microfluidic field. Microparticles will be used to create biomimetic fluid suspensions suitable for optical measurement techniques, such as μPIV.

PDMS microdroplets formed in the jetting regime lead to polydispersed particles. Visualization by a high speed camera shows an unstable jet that breaks irregularly, forming microdroplets of different sizes. Adjustment on the experimental setup is required to work at smaller flow rates, to reach the dripping regime, in which droplet formation is more regular.

This work is a first step on the manufacture of PDMS microparticles capable of yield the desired rheological proprieties of fluid suspensions and of attain optimal optical access. Further work is necessary to develop a high throughput device that produces monodispersed particles.

Acknowledgements

Work funded by FEDER funds through the Operational Programme for Competitiveness Factors – COMPETE, ON.2 - O Novo Norte - North Portugal Regional Operational Programme and National Funds through FCT - Foundation for Science and Technology under the projects: PEst-OE/EME/UI0532 and NORTE-07-0124-FEDER-000025-RL2_Environment & Health, by the Eixo I do Programa Operacional Fatores de Competitividade (POFC) QREN, project reference COMPETE: FCOMP-01-0124-FEDER-020241.

Notation

Latin	Definition	Units
D	Orifice of the outlet channel	(µm)
H	Channel depth	(µm)
Q	Volumetric flow rate	(µL min^{-1})
Q_c	Volumetric flow rate of the dispersed phase	(µL min^{-1})
Q_d	Volumetric flow rate dispersed of the continuous phase	(µL min^{-1})
V	Velocity	(m s^{-1})
w	Outlet channel width	(m)
w_c	Continuous phase channel width	(m)
w_{dis}	Dispersed phase channel width	(m)

Greek	Definition	Units
μ	Dynamic viscosity	(Pa s)
σ	Interfacial tension	(N m^{-1})

Dimensionless numbers	Definition
Ca	Capillary number

Acronyms	Definition
CAD	Computer-aided design

PDMS	Polydimethylsiloxane
RBC	Red blood cell
SDS	Sodium dodecyl sulphate
SU-8	Designation of epoxi-bored photoresist
μPIV	Micro particle image velocimetry

References

1. Teh, S.-Y., et al., *Droplet microfluidics.* Lab on a Chip, 2008. **8**(2): p. 198-198.
2. Dendukuri, D., et al., *Continuous-flow lithography for high-throughput microparticle synthesis.* Nat Mater, 2006. **5**(5): p. 365-369.
3. Xu, S., et al., *Generation of monodisperse particles by using microfluidics: control over size, shape, and composition.* Angew Chem Int Ed Engl, 2005. **44**(5): p. 724-8.
4. Baroud, C.N., et al., *Dynamics of microfluidic droplets.* Lab on a Chip, 2010. **10**(16): p. 2032-2032.
5. Peng Lee, C., Y. Hsin Chen, and Z. Hang Wei, *Fabrication of hexagonally packed cell culture substrates using droplet formation in a T-shaped microfluidic junction.* Biomicrofluidics, 2013. **7**(1): p. 14101.
6. Utada, A.S., et al., *Dripping to Jetting Transitions in Coflowing Liquid Streams.* Physical Review Letters, 2007. **99**(9): p. 094502-094502.
7. Anna, S.L., N. Bontoux, and H.A. Stone, *Formation of dispersions using "flow focusing" in microchannels.* Applied Physics Letters, 2003. **82**(3): p. 364-366.
8. Dufaud, O., E. Favre, and V. Sadtler, *Porous elastomeric beads from crosslinked emulsions.* Journal of Applied Polymer Science, 2002. **83**(5): p. 967-971.
9. Dendukuri, D. and P.S. Doyle, *The synthesis and assembly of polymeric microparticles using microfluidics.* Advanced Materials, 2009. **21**(41): p. 4071-4086.
10. Todd, P.L. and F.E. Jon, *A review of the theory, methods and recent applications of high-throughput single-cell droplet microfluidics.* Journal of Physics D: Applied Physics, 2013. **46**(11): p. 114005.
11. Garstecki, P., H.A. Stone, and G.M. Whitesides, *Mechanism for Flow-Rate Controlled Breakup in Confined Geometries: A Route to Monodisperse Emulsions.* Physical Review Letters, 2005. **94**(16): p. 164501.
12. Christian, H., *Large-scale droplet production in microfluidic devices—an industrial perspective.* Journal of Physics D: Applied Physics, 2013. **46**(11): p. 114008.
13. Garstecki, P., et al., *Formation of droplets and bubbles in a microfluidic T-junction-scaling and mechanism of break-up.* Lab on a Chip, 2006. **6**(3): p. 437-446.

14. Nie, Z., et al., *Emulsification in a microfluidic flow-focusing device: effect of the viscosities of the liquids.* Microfluidics and Nanofluidics, 2008. **5**(5): p. 585-594.

15. Tran, T.M., S. Cater, and A.R. Abate, *Coaxial flow focusing in poly(dimethylsiloxane) microfluidic devices.* Biomicrofluidics, 2014. **8**(1): p. 016502.

16. Takeuchi, S., et al., *An Axisymmetric Flow-Focusing Microfluidic Device.* Advanced Materials, 2005. **17**(8): p. 1067-1072.

17. Jiang, K., et al., *Microfluidic synthesis of monodisperse PDMS microbeads as discrete oxygen sensors.* Soft Matter, 2012. **8**(4): p. 923-926.

18. Mata, A., A. Fleischman, and S. Roy, *Characterization of Polydimethylsiloxane (PDMS) Properties for Biomedical Micro/Nanosystems.* Biomedical Microdevices, 2005. **7**(4): p. 281-293.

19. Friend, J. and L. Yeo, *Fabrication of microfluidic devices using polydimethylsiloxane.* Biomicrofluidics, 2010. **4**(2): p. 026502.

20. Di Benedetto, F., et al., *Rolling particle lithography by soft polymer microparticles.* Soft Matter, 2013. **9**(7): p. 2206-2206.

21. Sousa, P.C., et al., *Efficient microfluidic rectifiers for viscoelastic fluid flow.* Journal of Non-Newtonian Fluid Mechanics, 2010. **165**(11–12): p. 652-671.

22. Sousa, P.C.S.d., *Entry flow of viscoelastic fluids at macro- and micro-scale*. 2010, Faculdade de Engenharia.

23. Cubaud, T. and T.G. Mason, *Capillary threads and viscous droplets in square microchannels.* Physics of Fluids (1994-present), 2008. **20**(5): p. 053302.